

Probing Active Nanophotonic Materials Phenomena under Electrostatic Modulation

Thesis by
Areum Kim

In Partial Fulfillment of the Requirements for
the degree of
Doctor of Philosophy

The Caltech logo, featuring the word "Caltech" in a bold, orange, sans-serif font.

CALIFORNIA INSTITUTE OF TECHNOLOGY
Pasadena, California

2024
Defended May 24th 2024

© 2024

Areum Kim

ORCID: 0000-0001-9259-0906

ABSTRACT

Nanophotonic metastructured devices have gained significant attention due to their ability to manipulate properties of light such as the wavelength, amplitude, and phase. For photonic metastructures, these properties are typically fixed at the time of fabrication, as they depend on the geometrical parameters of resonant structures. Therefore, there is a growing interest in active nanophotonic devices, which can dynamically control the properties of light by incorporating active materials and applying external stimuli, in operation after fabrication.

This thesis investigates the dynamic control of light through electrostatic modulation of metastructures containing indium tin oxide (ITO) and monolayer transition metal dichalcogenides (1L-TMDs) materials. Specifically, we analyze the dynamic behavior of these materials, characterizing their morphological, electrical, and optical properties within devices.

In the first two chapters, we discuss the effects of ion migration on the electro-optic response of ITO-based active nanophotonic devices. Initially, we investigated uniformly deposited silver/dielectric/ITO heterostructures. Under electrical bias, silver ions and oxygen vacancies in the ITO actively migrate changing the device operating characteristics, resulting in hysteretic current-voltage curve behavior. Although optical modulation was barely observed, we explored the thermodynamic instability giving rise to electrical hysteresis in this volatile device. Furthermore, we investigated the impact of oxygen vacancy ion migration on the frequency response and phase modulation of ITO-based active metasurfaces. By annealing the devices, we were able to reduce the oxygen vacancy concentration, thereby improving the device high frequency performance.

In the latter two chapters, we explore the electro-optic response of field effect heterostructures comprised of 1L-TMDs in high-Q resonators. We designed and simulated two distinct types of high-Q resonators: Fabry-Perot resonators and silicon pillar resonators. We optimized the geometrical parameters of these resonant

structures embedded with 1L-TMDs to enhance device amplitude and phase modulation. Subsequently, we examined the potential for electro-optic modulation of TMDs in the telecommunication band, beyond their excitonic resonance wavelengths, by integrating them with Fabry-Perot resonators. We also discussed the compatibility of 1L-TMDs with gated heterostructure fabrication methods.

Overall, this thesis presents the application of electrical bias as a tool for the dynamic control of light in ITO and 1L-TMDs-based nanophotonic devices, with potential future applications in adaptive and reconfigurable photonic technologies.

PUBLISHED CONTENT AND CONTRIBUTIONS

1. Areum Kim, Souvik Biswas, Ruzan Sokhoyan, and Harry Atwater. “Van der Waals materials for dynamically tunable high-Q dielectric metasurfaces” In preparation
Contribution: conception of the project, transfer matrix calculation, Lumerical FDTD calculation, data analysis, writing of the manuscript
2. Areum Kim, Claudio Hail, Souvik Biswas, and Harry Atwater. “Effects of atomic layer deposition on the optical and topographical properties of monolayer transition metal dichalcogenides” In preparation
Contribution: conception of the project, sample preparation and characterization, data collection, data analysis, writing of the manuscript
3. Areum Kim, Jared Sisler, and Harry Atwater. “Ion migration effects on frequency response and phase modulation in oxide-based active metasurfaces” In preparation
Contribution: conception of the project, quasi-static data collection and analysis, writing of the manuscript
4. Areum Kim, Souvik Biswas, Claudio Hail, and Harry Atwater. “Gate tunability of refractive index in various monolayer transition metal dichalcogenides” In preparation
Contribution: conception of the project, sample preparation and characterization, data collection, data analysis, writing of the manuscript

TABLE OF CONTENT

| | |
|---|-----------|
| Abstract..... | iii |
| Published content and contributions | v |
| Table of Content..... | vi |
| List of Illustrations | viii |
| List of Tables..... | xx |
| | |
| Chapter I: Introduction..... | 1 |
| 1.1 Active nanophotonics | 1 |
| 1.2 Scope of the thesis | 3 |
| | |
| Chapter II: Towards dynamically tunable metasurfaces: Understanding ion migration effects in silver/dielectric/indium tin oxide (ITO) heterostructures | 5 |
| 2.1 Introduction..... | 5 |
| 2.2 Simulations..... | 10 |
| 2.3 Device fabrication..... | 17 |
| 2.3.1 Ultrasmooth silver and alumina deposition..... | 17 |
| 2.3.2 Electrical and optical properties of sputtered ITO | 27 |
| 2.3.3 Whole device stack | 30 |
| 2.4 Electrical response | 34 |
| 2.5 Optical response | 47 |
| 2.6 Conclusion and future work..... | 50 |
| | |
| Chapter III: Probing ion migration impacts on the optical response in oxide-based active metasurfaces | 52 |
| 3.1 Introduction..... | 52 |
| 3.2 Electro-optic response..... | 55 |
| 3.3 Conclusion and future work..... | 64 |

| | |
|--|-----------|
| Chapter IV: Monolayer transition metal dichalcogenides (1L-TMDs) for dynamically tunable metasurfaces | 65 |
| 4.1 Introduction | 65 |
| 4.2 Fabry-Perot resonators embedded with 1L-TMDs | 68 |
| 4.3 Si-pillar resonators embedded with 1L-TMDs..... | 72 |
| 4.4 Conclusion and future work..... | 82 |
| | |
| Chapter V: High-Q Fabry-Perot resonators embedded with 1L-TMDs.. | 84 |
| 5.1 Introduction | 84 |
| 5.2 Gate tunability of refractive index in various 1L-TMDs | 86 |
| 5.3 Distributed Bragg reflector (DBR) | 98 |
| 5.4 1L-TMDs compatibility with deposition techniques | 103 |
| 5.5 Optical response | 116 |
| 5.6 Conclusion and future work..... | 129 |
| | |
| Bibliography | 131 |

LIST OF ILLUSTRATIONS

| <i>Number</i> | <i>Page</i> |
|--|-------------|
| Figure 1.1 Various mechanisms to achieve dynamic control of light post-fabrication under external stimuli..... | 1 |
| Figure 2.1 Schematic diagram of electrochemical reactions in a memristor when applying an electrical bias..... | 6 |
| Figure 2.2 General ionic transport mechanisms: (a) Drift (b) Electromigration (c) Fick's diffusion (d) Thermophoresis..... | 7 |
| Figure 2.3 (a) Real part and (b) Imaginary part of the dielectric function of ITO and Ag as a function of wavelength. (c) Real part and (d) Imaginary part of the dielectric function of Ag-embedded ITO at different fill fractions of Ag as a function of wavelength..... | 10 |
| Figure 2.4 (a) Schematic diagram of three different stacks with different fill fractions of Ag. (b) Calculated refractive index of ITO with 11% Ag embedded. (c) Calculated refractive index of ITO with 20% Ag embedded. (d) Reflectance spectrum calculated by transfer matrix calculation. Each color in the graph corresponds to the schematics in (a)..... | 12 |
| Figure 2.5 (a) Schematic diagram of a unit cell of Au stripe metasurfaces with three different stacks with varying fill fractions of Ag: 1) No effective medium when no applied bias, 2) 11% Ag embedded effective medium implying a low bias, 3) 20% Ag embedded effective medium implying a high bias. (b) Spatial distribution of the electric field amplitude in the metasurface unit cell in the x-z direction at a wavelength of 1480 nm when there is no applied bias. (c) Spatial distribution of the electric field amplitude in the metasurface unit cell in the x-z direction at a wavelength of 1667 nm when a low voltage is applied. (d) Reflectance spectrum in the near-infrared (NIR) region around the resonance wavelengths. (e) Corresponding phase profile..... | 13 |

Figure 2.6 Simulation results of Ag stripe metasurfaces for amplifying the effect of Ag filament growth and rupture: (a) No filament. (b) 80% growth of the Ag filament within the dielectric. (c) 90% growth of the Ag filament within the dielectric. (d) 100% growth of the Ag filament within the dielectric. (e)-(h) Corresponding absolute electric field distribution of the unit cell of the metasurface. (i)-(l) Corresponding reflectance spectrum in the near-infrared (NIR) region

Figure 2.7 (a) General Ag deposition recipe. (b) SEM image of the surface after 80 nm Ag deposition. (c) SEM image of a 5 nm-thick alumina surface on Ag.

Figure 2.8 (a) Thin film growth mechanisms. (b) Surface energy at the interface and the wetting angle.

Figure 2.9 Surface topological image of (a) Ag, (b) Al₂O₃, (c) Depth profiles at three different points indicated in (b), all analyzed by AFM

Figure 2.10 Effect of oxygen plasma treatment on roughness of Ag and Al₂O₃ measured by AFM (a) Ag without plasma treatment, (b) Ag with plasma treatment, (c) Al₂O₃ on Ag without plasma treatment, (d) Al₂O₃ on Ag with plasma treatment

Figure 2.11 Effect of seed layers on the roughness of Ag analyzed by SEM: (a) Ag only without any seed layer, (b) 1 nm Ti/80 nm Ag, (c) 1 nm Cr/80 nm Ag, (d) 1 nm Ge/80 nm Ag

Figure 2.12 Effect of seed layers on the roughness of Al₂O₃ analyzed by SEM: (a) Ag/5 nm Al₂O₃ without any seed layer, (b) 1 nm Ti/80 nm Ag/5 nm Al₂O₃, (c) 1 nm Cr/80 nm Ag/5 nm Al₂O₃, (d) 1 nm Ge/80 nm Ag/5 nm Al₂O₃

Figure 2.13 Effect of oxygen flow rate during Ag deposition on the roughness of Ag and Al₂O₃ measured by AFM: (a) Ag with 0.5 sccm oxygen flow rate, (b) Ag with 5 sccm oxygen flow rate, (c) Al₂O₃ on Ag with 0.5 sccm oxygen flow rate, (d) Al₂O₃ on Ag with 5 sccm oxygen flow rate

Figure 2.14 Effect of Ag deposition rate on the roughness of Ag and Al₂O₃ measured by Atomic Force Microscopy (AFM): (a) Ag deposited at 1 Å/s, (b) Ag deposited at 0.5 Å/s, (c) Ag deposited at 0.5 Å/s including 1 nm AgO, (d) Al₂O₃ on Ag deposited at 1 Å/s, (e) Al₂O₃ on Ag deposited at 0.5 Å/s, (f) Al₂O₃ on Ag

- deposited at 1 Å/s including 1 nm AgO, (g) Line profile represented by the linecut in (c), (h) Line profile represented by the linecut in (f)..... 24
- Figure 2.15 Effect of Ag crucible on the roughness of Ag measured by AFM: (a) 2 nm Ge/80 nm Ag with a graphite crucible, (b) 2 nm Ge/80 nm Ag with a molybdenum crucible, (c) 2 nm Ge/80 nm Ag with a molybdenum crucible, cooling down twice to lower the chamber temperature during deposition 26
- Figure 2.16 Carrier concentration in the ITO as a function of oxygen flow rate during the sputtering deposition process. 28
- Figure 2.17 Band diagram when the ITO has (a) a high work function (WF) and (b) a low WF. Refractive index of (c) high WF ITO with a low carrier concentration of $4 \times 10^{19} \text{ cm}^{-3}$ and high mobility of $50 \text{ cm}^2/\text{Vs}$, and (d) low WF ITO with a high carrier concentration of $4.5 \times 10^{20} \text{ cm}^{-3}$ and low mobility of $13 \text{ cm}^2/\text{Vs}$ 29
- Figure 2.18 (a) Cross-sectional view measured by SEM. The device stack consists of an 80 nm-thick Ag layer, a 5 nm-thick Al_2O_3 layer, and a 118 nm-thick ITO layer on a 1 μm -thick SiO_2 -on-Si substrate. (b) Energy distribution of EDS at 6 keV calculated by Casino simulation. (c) EDS analysis results before and after applying a voltage 31
- Figure 2.19 (a) Macroscopic image of a 2-inch wafer patterned using shadow masks. (b) Microscopic image of the active area, the Ag-ITO crossover region. (c)-(f) show AFM images of different regions: (c) Ag surface, (d) Al_2O_3 on Si surface, (e) ITO on Al_2O_3 on Ag surface, and (f) ITO on Al_2O_3 surface..... 32
- Figure 2.20 (a) Macroscopic image of a 2-inch wafer patterned using EBPG. (b) Microscopic image of the active area, the Ag-ITO crossover region. (c) Macroscopic image of a device connected to a printed circuit board (PCB) 32
- Figure 2.21 Schematic diagram of (a) when a single-layer resist or a shadow mask is used for patterning, and (b) when a bilayer resist is used for patterning. (c) Height profile and (e) topological image at the edge of the patterned Ag using a single-layer resist or a shadow mask. (d) Height profile and (f) topological image at the edge of the patterned Ag using a bilayer resist. (c)-(f) are measured by AFM33

| | |
|---|----|
| Figure 2.22 Four types of ion migration mechanisms, corresponding filament shapes, and IV curves..... | 34 |
| Figure 2.23 Schematic of the I-V characteristics for volatile and nonvolatile switching devices – A) volatile threshold switching, B) write-once-read-many (WORM) switching, C) unipolar switching, and D) bipolar switching behavior | 35 |
| Figure 2.24 Device-to-device variation in I-V curve. (a) Schematic diagram of the device with an ITO having a high carrier concentration. (b)-(f) Five I-V curves of each device from (a). The devices were fabricated under the same deposition conditions on the same 2-inch SiO ₂ on Si wafer. (g) Schematic diagram of the device with an ITO having a low carrier concentration. (h)-(l) Five I-V curves of each device from (g). The devices were fabricated under the same deposition conditions on the same 2-inch SiO ₂ on Si wafer..... | 36 |
| Figure 2.25 (a) Top view of the device, specifically representing the active area. (b) Ag/5nm Al ₂ O ₃ /ITO, (c) Ag/5nm HfO ₂ /ITO, (d) Ag/6nm HAOL/ITO..... | 37 |
| Figure 2.26 Cyclic measurements for 100 cycles to analyze the electrical endurance of the Ag/Al ₂ O ₃ /ITO device..... | 38 |
| Figure 2.27 I-V curves of the Al ₂ O ₃ device taken every 10 cycles out of 100 cycles. (a) 10 th , (b) 20 th , (c) 30 th , (d) 40 th , (e) 50 th , (f) 60 th , (g) 70 th , (h) 80 th , (i) 90 th , (j) 100 th | 38 |
| Figure 2.28 I-V curves of the HAOL device taken every cycle out of 10 cycles. (a) 1 st , (b) 2 nd , (c) 3 rd , (d) 4 th , (e) 5 th , (f) 6 th , (g) 7 th , (h) 8 th , (i) 9 th , (j) 10 th | 39 |
| Figure 2.29 I-V curves of the 20nm HfO ₂ device taken over 5 cycles, respectively. (a)-(e) Cycles 1-5 under positive bias. (f) Proposed growth-connection-disconnection-retraction mechanism when under positive bias. (g)-(k) Cycles 1-5 under negative bias application. The compliance current was set at 10 μA. (l) Proposed growth-connection-disconnection-retraction mechanism when under negative bias. In (f) and (l), gray dots represent reduced Ag ions, and white dots represent oxygen-deficient regions..... | 40 |
| Figure 2.30 Current over time when holding at -1V in the 20nm HfO ₂ device at a compliance current of 1 μA..... | 41 |

- Figure 2.31 (a) Schematic diagram of a device with a thicker ITO layer and Al_2O_3 gate dielectric. (b) Current over time when holding at 1 mV bias. (c) Current over time when holding at -1 mV bias..... 42
- Figure 2.32 I-V curves of a device with a thin ITO layer and Al_2O_3 dielectric, depending on the size of the active area. (a) 100 μm by 100 μm , (b) 50 μm by 50 μm , (c) 20 μm by 20 μm , (d) 10 μm by 10 μm , (e) 5 μm by 5 μm . The compliance current for (b)-(e) is 100 μA 43
- Figure 2.33 Maximum current density as a function of the active area..... 43
- Figure 2.34 I-V curves of a device with a thin ITO layer and Al_2O_3 dielectric with an active area of 5 μm by 5 μm , taken every cycle out of 4 cycles. (a) 1st, (b) 2nd, (c) 3rd, (d) 4th cycle. (compliance current density of 100A/cm²) 44
- Figure 2.35 (a) Relationship between Gibbs free energy and the filament size based on the classical nucleation theory. Depending on the filament size, the device can behave both volatile switching or, nonvolatile switching. (b) proposed growth-connection-disconnection-retraction mechanism. Gray dots represent reduced Ag ions and white dots are oxygen deficient regions 46
- Figure 2.36 (a) Measured and calculated reflectance spectrum of the Ag/ Al_2O_3 /thin ITO device in the visible wavelength range. (b) Measured and calculated reflectance spectrum of the Ag/ Al_2O_3 /thin ITO device in the near-infrared (NIR) region..... 47
- Figure 2.37 Reflectance spectrum in the visible wavelength (a) when applying an electrical bias of -10 mV to 10 mV. (b) when holding at 700 mV, where the current abruptly increased. The corresponding electrical response is represented in Figure 2.24 (c) 48
- Figure 2.38 (a) Schematic diagram of Au stripe metasurfaces with Ag/ Al_2O_3 /ITO. Reflectance spectrum around the resonance (b) measured after 2 days (c) measured after 8 days to investigate Ag ion diffusion over time. Expected reflectance modulation was represented in Figure 2.5 calculated by Lumerical FDTD.. 49
- Figure 2.39 Schematic diagram illustrating ways to improve optical modulation in the Ag/dielectric/ITO device: (a) Few filament formations due to a non-uniform Ag

layer. (b) Increase the diffusion of Ag into the ITO. (c) Increase the number of oxygen vacancies in the ITO. (d) Increase the density of Ag filaments. (e) Thicken the Ag filaments..... 51

Figure 3.1 An indication of ion migration in the gate dielectric under electrical bias

(a) Schematic diagram of a metal-insulator-metal (MIM) capacitor with inert gold electrodes. (b) Current-voltage curve with a compliance current (C.C.) of 100nA

Figure 3.2 Relative carrier concentration and relative mobility of the ITO under different annealing conditions. (a)-(c) The absolute carrier concentration of ITO(L)

is 0.12 cm^{-3} , $\text{Al}_2\text{O}_3/\text{ITO}(\text{L})$ is 0.21 cm^{-3} , and $\text{Al}_2\text{O}_3/\text{ITO}(\text{H})$ 1.76 cm^{-3} . Relative carrier concentration as a function of annealing temperature (a) in air for 1-2 hours (b) in vacuum for 14-16 hours. (c) Relative carrier concentration as a function of annealing

time when annealed in vacuum at $150 \text{ }^\circ\text{C}$. (d)-(f) The absolute mobility of ITO(L) is $32.6 \text{ cm}^2/\text{Vs}$, $\text{Al}_2\text{O}_3/\text{ITO}(\text{L})$ is $48.7 \text{ cm}^2/\text{Vs}$, and $\text{Al}_2\text{O}_3/\text{ITO}(\text{H})$ $38.9 \text{ cm}^2/\text{Vs}$. Relative mobility as a function of annealing temperature (d) in air for 1-2 hours (e) in vacuum for 14-16 hours. (f) Relative mobility as a function of annealing time when annealed

in vacuum at $150 \text{ }^\circ\text{C}$ 58

Figure 3.3 Mechanism showing the removal of oxygen vacancies in the gate dielectric during the annealing process..... 58

Figure 3.4 (a) Schematic diagram of ITO-based active metasurface unit cell. The structure is periodic ($p=400\text{nm}$), and the top gold stripe antenna is lengthy in the y-direction. $t_{\text{Au}}=100\text{nm}$, $t_{\text{ITO}}=17\text{nm}$, $t_{\text{HAOL}}=8\text{nm}$ (two pairs of alternating layers of 1nm alumina and 3nm hafnia), $t_{\text{Si}}=40\text{nm}$, $w_{\text{Si}}=220\text{nm}$. (b) Measured reflectance spectra of the metasurface by applying voltage from 3V to -3V. (c) Comparison of current-voltage (I-V) curves between the metasurface without and with post-annealing process in vacuum, with a compliance current of 100nA 60

Figure 3.5 Comparison of phase profiles between the metasurface (a) without post-annealing process, or a thinner gate dielectric and (b) with post-annealing process, or a thicker gate dielectric as a function of the applied voltage..... 60

Figure 3.6 Quasi-static amplitude response at different applied voltages. Each graph shows the resonance wavelength of a metasurface while slowly sweeping the applied

voltage. (a) The metasurface response without any annealing process. (b) The metasurface response with annealing at 150°C in a vacuum chamber for 24 hours. (c) The metasurface response with annealing at 150°C in ambient air for 24 hours

Figure 3.7. Measured reflectance modulation with modulation frequencies ranging from 0.1 Hz to 1 MHz for devices with and without a 150°C anneal in a vacuum chamber 63

Figure 4.1 High-Q Fabry-Perot resonators embedded with van der Waals materials for amplitude modulation. (a) Schematic of dual distributed Bragg reflectors (DBRs) with an equal number of pairs. (b) Maximum achievable amplitude modulation depth in both transmission and reflection modes as a function of the number of DBR pairs in the dual DBRs. (c) Transmittance spectra and (d) reflectance spectra around the resonance, illustrating the spectral variation with increasing number of DBR pairs 70

Figure 4.2 High-Q Fabry-Perot resonators for a phase modulator, comprised of a 7-pair top DBR and an 8-pair bottom DBR. (a) and (b) depict transmittance and reflectance, alongside the corresponding phase, as a function of wavelength when 1L-TMD is undoped. (c) and (d) illustrate transmittance and reflectance modulation, along with the corresponding phase shift, as a function of the index change in 1L-TMD at a wavelength of $\lambda = 1555.14$ nm 71

Figure 4.3 High-Q transmissive metasurfaces with van der Waals materials for a phase modulator, comprising an array of amorphous a-Si rectangular pillars on a SiO₂ substrate. (a) Schematic of a unit cell of the metasurfaces. (b) Spatial distribution of the electric field amplitude in the metasurface unit cell in x-y and y-z planes, respectively 72

Figure 4.4 Optical response change when varying the Si pillar height (a) Transmission spectrum, and (b) corresponding phase profile when varying height from 850nm to 860nm. (c) Transmission spectrum, and (d) corresponding phase profile when varying height from 858nm to 860nm. (e) Resonance wavelength and linewidth change as a function of pillar height. (f) Q-factor as a function of Si pillar

| | |
|---|----|
| height. Red region indicates the low phase shift even though Q-factor is still high | 74 |
| Figure 4.5 (a) Transmittance and phase as a function of wavelength when 1L-TMD is undoped. (b) Transmittance modulation, along with the corresponding phase shift, as a function of the refractive index change in 1L-TMD at a wavelength of λ = 1551.42 nm | 75 |
| Figure 4.6 (a) Transmittance spectrum when changing the gate dielectric materials. (b) Corresponding phase profile. | 76 |
| Figure 4.7 (a) Transmittance spectrum when changing the imaginary part k of the refractive index of the 1L-TMD from 0 to 0.0001. (b) Q-factor and damping rate, or the linewidth, as a function of k in 1L-TMD..... | 77 |
| Figure 4.8. Schematic of a two-level phase grating system in High-Q transmissive metasurfaces with 1L-TMDs having two distinct refractive indices, n_1 and n_2 . | 78 |
| Figure 4.9 (a) 3D image of far-field intensity of the electric field for a two-level phase grating when the refractive index change between neighboring 1L-TMD is $\Delta n = 0.2$ to 0.7 in the steering angle range of -40° to 40° . (b) Far-field intensity at the wavelength of 1550.1 nm, (c) Far-field intensity at the steering angle of 33° , (d) Magnified view of (b) to closely analyze the intensity change as a function of Δn | 79 |
| Figure 4.10 3D image of far-field intensity of the electric field for a three-level phase grating when the refractive index change between neighboring 1L-TMD is 3.795, 3.367, and 3.050, respectively, in the steering angle range of -40° to 40° | 80 |
| Figure 4.11 The transmittance spectrum mismatch between FDTD simulation and RCWA simulations trying different propagation vector k values in RCWA | 81 |
| Figure 5.1 (a) Schematic diagram depicting the side view of the capacitor geometry with four 1L-TMDs. (b)-(e) Optical microscopic images of exfoliated monolayers: (b) WS_2 , (c) WSe_2 , (d) MoS_2 , and (e) MoSe_2 . The scale bar represents $10 \mu\text{m}$, and the dotted area indicates the presence of the monolayer for each case..... | 87 |
| Figure 5.2 Optical response of monolayers of WS_2 , WSe_2 , MoS_2 , and MoSe_2 exfoliated on 20 nm alumina and 100 nm gold on a silicon substrate. (a), (d), (g), (j) | |

| | |
|--|-----|
| Measured reflectance spectra. (b), (e), (h), (k) Real part of the refractive index (n). | |
| (c), (f), (i), (l) Imaginary part of the refractive index (k). The red curve represents the optical response at 0 V, and the blue curve represents the response at 8 V. The black dotted curve represents the fitted curve with three oscillator models obtained by transfer matrix calculations | 90 |
| Figure 5.3 Refractive index change at the wavelength where the largest $\Delta n/k$ between 0V and 8V is observed | 91 |
| Figure 5.4 Exciton parameters of WS ₂ , WSe ₂ , MoS ₂ , and MoSe ₂ extracted through transfer matrix calculations employing three Lorentz oscillator models. (a), (d), (g), (j) Resonant energy in eV. (b), (e), (h), (k) Linewidth in meV. (c), (f), (i), (l) Oscillator strength in meV | 93 |
| Figure 5.5 (a) Effect of the refractive index contrast on the reflectance spectrum. The blue graph assumes 10 pairs of SiOx and SiNx (n=0.55), and the orange graph assumes 10 pairs of SiOx and TiOx (n=1.27). (b) Effect of the number of pairs N on the reflectance spectrum. All cases assume SiOx and TiOx pairs | 99 |
| Figure 5.6 (a) Reflectance spectrum as a function of the number of top DBR pairs obtained by transfer matrix calculations. (b) Measured reflectance spectrum as a function of the number of evaporated top DBR pairs..... | 100 |
| Figure 5.7 Measured reflectance spectrum fitted by a Lorentzian curve (a) 4 pairs, (b) 6 pairs, (c) 8 pairs, (d) 10 pairs, (e) 12 pairs, (f) 14 pairs | 101 |
| Figure 5.8 Comparison of FWHM of the resonance between calculation and experiment as a function of the number of DBR pairs | 102 |
| Figure 5.9 Impact of ALD process temperature during the deposition of 20nm alumina on the surface morphology and photoluminescence of 1L-WS ₂ . Process 1: 10nm alumina deposited at 150°C, followed by 10nm at 200°C. Process 2: 10nm alumina deposited at 150°C, followed by 10nm at 270°C. Process 3: 10nm alumina deposited at 200°C, followed by 10nm at 270°C. Process 4: 7nm alumina deposited at 150°C, followed by 7nm at 200°C, and 6nm at 270°C. (a)-(d) depict the surface morphology of the deposited alumina on a bare silica-on-silicon substrate. (e)-(h) | |

illustrate the surface morphology of the deposited alumina on exfoliated 1L-WS₂. (i)-(l) represent the normalized PL intensity before and after deposition 107

Figure 5.10 Impact of ALD process temperature during the deposition of a 20nm alumina film on the photoluminescence of 1L-WS₂. Process 1: 10nm alumina deposited at 150°C, followed by 10nm at 200°C. Process 2: 10nm alumina deposited at 150°C, followed by 10nm at 270°C. Process 3: 10nm alumina deposited at 200°C, followed by 10nm at 270°C. Process 4: 7nm alumina deposited at 150°C, followed by 7nm at 200°C, and 6nm at 270°C. (a)-(d) represent the PL intensity before and after deposition..... 108

Figure 5.11 Influence of oxygen plasma surface treatment prior to alumina deposition. The first column presents the results from the deposition of a 30nm alumina film without surface treatment. The second column shows the results from the deposition of a 30nm alumina film after UV-ozone treatment. (a) depicts the surface morphology of the deposited alumina on a bare silica-on-silicon substrate. (b) illustrates the surface morphology of the deposited alumina on exfoliated 1L-MoSe₂. (c) represents the PL intensity, and (d) represents the normalized PL intensity before deposition, after treatment, and after deposition, respectively 109

Figure 5.12 Influence of UV-ozone surface treatment prior to alumina deposition. The first column presents the results from the deposition of 30nm alumina without surface treatment. The second column shows the results from the deposition of 30nm alumina after UV-ozone treatment. (a)-(b) depict the surface morphology of the deposited alumina on a bare silica-on-silicon substrate. (c)-(d) illustrate the surface morphology of the deposited alumina on exfoliated 1L-WS₂. (e)-(f) represent the normalized PL intensity before and after deposition..... 111

Figure 5.13 Influence of UV-ozone surface treatment prior to alumina deposition. (a) represents the PL intensity from the deposition of a 30nm alumina film without surface treatment, before and after deposition. (b) represents the PL intensity from the deposition of a 30nm alumina film after UV-ozone treatment 112

Figure 5.14 Variability in surface morphology and optical properties, as probed by PL, among different 1L-TMDs. Each column corresponds to results from 1L-WS₂,

| | |
|--|-----|
| WSe ₂ , MoS ₂ , MoSe ₂ , and a bare SiO ₂ -on-Si substrate, respectively. (a)-(e) depict the surface morphology of the deposited 179nm-thick alumina on the exfoliated monolayers. (f)-(j) represent the normalized PL intensity before and after deposition | 112 |
| Figure 5.15 Normalized PL intensity of various gate dielectric candidates before and after deposition with (a) exfoliated and transferred hexagonal boron nitride (hBN), (b) electron-beam evaporated Al ₂ O ₃ , (c) electron-beam evaporated SiO ₂ , and (d) plasma-enhanced chemical vapor deposited SiO ₂ | 114 |
| Figure 5.16 PL intensity of various gate dielectric candidates before and after deposition with (a) exfoliated and transferred hexagonal boron nitride (hBN), (b) electron-beam evaporated Al ₂ O ₃ , (c) electron-beam evaporated SiO ₂ , and (d) plasma-enhanced chemical vapor deposited SiO ₂ | 115 |
| Figure 5.17 (a) Schematic diagram of a Fabry-Perot resonator consisting of dual metallic mirrors. (b) Schematic diagram of a Fabry-Perot resonator consisting of dual dielectric mirrors. (c) Reflectance spectrum of the structure in (a) depending on the presence or absence of 1L-TMDs. (d) Reflectance spectrum of the structure in (b) depending on the presence or absence of 1L-TMDs | 117 |
| Figure 5.18 Exfoliated and transferred 1L-TMDs onto SiO ₂ /Au on a substrate. (a) WS ₂ , (b) MoS ₂ , (c) WSe ₂ , (d) MoSe ₂ , (e) MoTe ₂ | 118 |
| Figure 5.19 (a) Reflectance spectrum of 5 distinct 1L-TMDs embedded in an Au/Au Fabry-Perot resonator. (b) Resonance wavelength of each material. (c) Full-width at half-maximum (FWHM) of the reflectance response fitted by a Lorentzian curve. (d) Minimum reflectance of the reflectance response | 119 |
| Figure 5.20 Optical setup configuration for NIR reflection response. (a) No beam collimation. (b) Beam collimation achieved by locating a lens at the back focal plane of an objective..... | 120 |
| Figure 5.21 Reflectance spectrum as a function of top Au thickness from 50 nm to 70 nm. (a) Reflectance spectrum measured by the setup without beam collimation. (b) Reflectance spectrum measured by the setup with beam collimation ... | 120 |
| Figure 5.22 Optical setup configuration for NIR transmission response | 121 |

- Figure 5.23 (a) Calculated and (b) Measured transmittance spectrum as a function of the top Au thickness 122
- Figure 5.24 (a) Dielectric constant and dielectric strength of various gate dielectric candidate materials. (b) Gate dielectric evaluation and selection rules 123
- Figure 5.25 Three main criteria to select a gate dielectric. The first row represents an ideal example, and the second row depicts an unfavorable scenario. (a) and (d) Surface smoothness measured by atomic force microscopy (AFM). (b) and (e) Process compatibility evaluated by photoluminescence (PL) measurements. (c) and (f) Dielectric strength assessed by current-voltage (I-V) measurements using a probe station..... 123
- Figure 5.26 Normalized PL intensity before and after spin-coating of (a) PMMA, (b) SU-8, (c) HSQ..... 124
- Figure 5.27 Optical responses of a 1L-WS₂ embedded Fabry-Perot resonator. (a) Microscopic image of the device. (b) IR image measured at the wavelength of 1509 nm. (c) IR image taken at the same position as in (b), but with an iris to limit the measurement area. Transmittance spectrum at (d) the cavity without 1L-WS₂, (e) the cavity with 1L-WS₂, (f) the edge of 1L-WS₂ and the cavity..... 125
- Figure 5.28 Transmittance spectrum of different Fabry-Perot resonators: (a) evaporated SiO₂, (b) exfoliated and transferred hBN, (c) thin ALD-deposited Al₂O₃ and thick PECVD-deposited SiO₂. (d)-(e) are corresponding microscopic images of each device 126
- Figure 5.29 Optical response of a 1L-MoSe₂ embedded Fabry-Perot resonator. (a) Transmittance spectrum at the resonance. (b) Resonance wavelength modulation. (c) Q-factor modulation on the cavity without 1L-MoSe₂ under electrical bias. (d) Resonance wavelength modulation. (e) Q-factor modulation on the 1L-MoSe₂ under electrical bias. The voltage sweep was from 0 to positive 75V, to negative 75V, and back to 0V. The evaporated SiO₂ reached breakdown during the measurement at -50V application. The blue error bars in (b)-(e) represent the error from the fitting 128

LIST OF TABLES

| <i>Number</i> | <i>Page</i> |
|--|-------------|
| Table 2.1 Development and demonstration of optical memristors, and their properties and mechanisms | 8 |
| Table 2.2 Maxwell Garnett model and Bruggeman model for mixtures of materials A and B | 11 |
| Table 2.3 Overall Ag deposition recipes and corresponding roughness values of each layer, Ag, and Al ₂ O ₃ | 25 |
| Table 5.1 Electro-Optic properties of four types of 1L-TMDs around excitonic resonances. FOM: Figure of Merit. Averaged value represents the extracted values as a function of the applied voltage between 0 V and 8 V, averaged over this range | 95 |
| Table 5.2 Electro-Optic properties of four types of 1L-TMDs at the wavelength of 1550 nm. Values are extrapolated based on the reflectance measurements from 550 nm to 850 nm | 97 |
| Table 5.3 Dielectric materials candidate and their real part refractive index at 1550nm..... | 99 |

Chapter 1

INTRODUCTION

1.1 Active nanophotonics

Nanophotonics delves into the intricate interactions between light and nanoscale objects. Each component in this realm operates on a subwavelength level, interacting with light to modulate the optical functionality of the device, such as amplitude, phase, polarization, or wavelength¹⁻¹⁰. However, their functionality remains fixed after fabrication, limiting their broader applications.

Consequently, researchers have explored active nanophotonics, which enables dynamic control of light by applying external stimuli (electrical gating, magnetic fields, chemical doping, mechanical forces, thermal energy, or optical pumping) to active materials¹¹⁻¹⁹. This approach allows for tuning the refractive index even after fabrication, imbuing the devices with versatility (Figure 1.1).

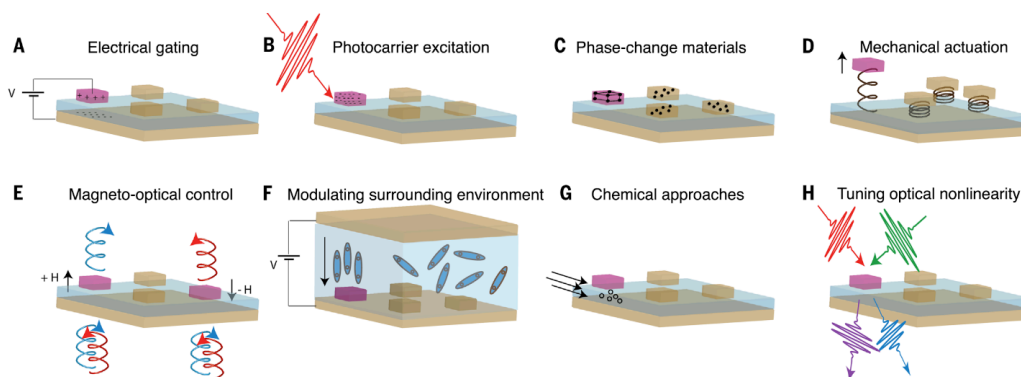


Figure 1.1 Various mechanisms to achieve dynamic control of light post-fabrication under external stimuli adopted from¹⁵.

Depending on the intended application, nanophotonic devices can find utility in diverse fields, including LiDAR (Light Detection and Ranging), LiFi (Light

Fidelity), and holographic imaging, among others. The ability to dynamically manipulate light opens up new avenues for innovation and adaptive functionality in these domains.

1.2 Scope of the thesis

This thesis encompasses the electrical gating effect in transparent oxide-based nanophotonic devices and monolayer transition metal dichalcogenides (1L-TMDs) based nanophotonic devices, with a focus on their electrical and optical responses. Specifically, the dynamic phenomena of these materials were analyzed in terms of their topological, electrical, and optical properties within the devices.

Chapters 2 and 3 concentrate on how the electrochemical reaction in transparent oxide-based nanophotonic devices affects the electrical and optical responses under an applied electrical bias.

In Chapter 2, a stack of silver (Ag), gate dielectric, and indium tin oxide (ITO) was deposited under optimized processes for uniform and ultrasmooth layers. When an electrical bias is applied to the stack, Ag ions and oxygen vacancies in the gate dielectric and ITO migrate within the layers. Alongside these electrochemical reactions, a distinct hysteresis loop was observed in the current-voltage curve. Following this electrical memory effect, the optical memory effect was studied, and strategies to amplify the optical modulation effect by ion migration were further discussed.

In Chapter 3, the impacts of oxygen vacancy ion migration were investigated on the frequency response and phase modulation of ITO-based active metasurfaces. Post-annealing at 150°C in a vacuum effectively reduced defects while preserving the ITO properties, mitigating hysteresis in electrical and optical responses. Time-resolved reflectance measurements revealed improved quasi-static resonance stabilization and enhanced switching speeds in annealed metasurfaces compared to unannealed devices.

Chapters 4 and 5 focus on effectively utilizing the emerging material, 1L-TMDs, by integrating them into active nanophotonic devices for applications ranging from the

visible wavelengths, where excitonic resonances occur, to the near-infrared (NIR) region beyond excitonic resonances. Overall, our findings highlight the promising capabilities of 2D TMD-based nanophotonic devices with low loss for advanced optical modulation and manipulation.

In Chapter 4, the versatility of dual dielectric mirror resonators as amplitude modulators or phase modulators by adjusting the number of dielectric mirror pairs was explored through simulations. The amplitude modulation configuration achieves an 80% transmittance modulation and 97% reflectance modulation. Meanwhile, the phase modulation configuration exhibits nearly a π -phase shift in transmission and a 2π -phase shift in reflection. In addition, a tunable metasurface featuring an array of silicon pillars on a silica substrate, with Q-factors exceeding 12000, was introduced for light manipulation in the NIR with 1L-TMDs. With a transmission phase shift of over π , we propose this metasurface for potential applications in 2D beam steering.

In Chapter 5, the interaction of four types of 1L-TMDs with visible light under electrical bias at room temperature was experimentally demonstrated. By measuring the reflectance response of each material, the refractive index, including the resonance wavelength, oscillator strength, and linewidth, respectively, were extracted as a function of the applied bias. The results can guide the selection of appropriate materials for different electro-optic applications. In addition, the possibility of employing their electro-optic modulation in telecommunication band applications beyond their excitonic resonance wavelength was studied by integrating them with Fabry-Perot resonators. Subsequently, for experimental demonstrations, the compatibility of 1L-TMDs with various deposition techniques was extensively researched. An Au/dielectric mirror Fabry-Perot resonator was fabricated by integrating with 1L-TMDs to analyze their optical functionalities.

TOWARDS DYNAMICALLY TUNABLE METASURFACES:
UNDERSTANDING ION MIGRATION EFFECTS IN
SILVER/DIELECTRIC/INDIUM TIN OXIDE(ITO) HETEROSTRUCTURES

2.1 Introduction

In this chapter, the investigation focuses on how the electrochemical reaction in a stack of silver (Ag), gate dielectric, and indium tin oxide (ITO) affects the electrical and optical response under an applied electrical bias.

A memristor, a portmanteau of "memory" and "resistor," is also known as a resistive switching memory. It is recognized as the fourth fundamental circuit element alongside the resistor, inductor, and capacitor. Typically, a memristor consists of an electrolyte sandwiched between two electrodes. The electrolyte acts as an ionic conductor but an electrical insulator. When an electrical bias is applied to the device, it initiates electrochemical reactions and facilitates ionic transport.

Figure 2.1 illustrates the electrochemical processes with a current-voltage curve. First, mobile ions, in this case Ag, are injected into the dielectric. Second, if the voltage is continually applied, the Ag ions migrate, and a reduction reaction occurs until the copper ions reach the other electrode. Third, the filament growth continues, and the conducting filament eventually shorts, creating a low-resistive state. Lastly, when the bias is reversed, the conducting filaments are disrupted, leading to a high-resistive state. The device can rapidly switch on and off by manipulating just a few atoms within the filaments.

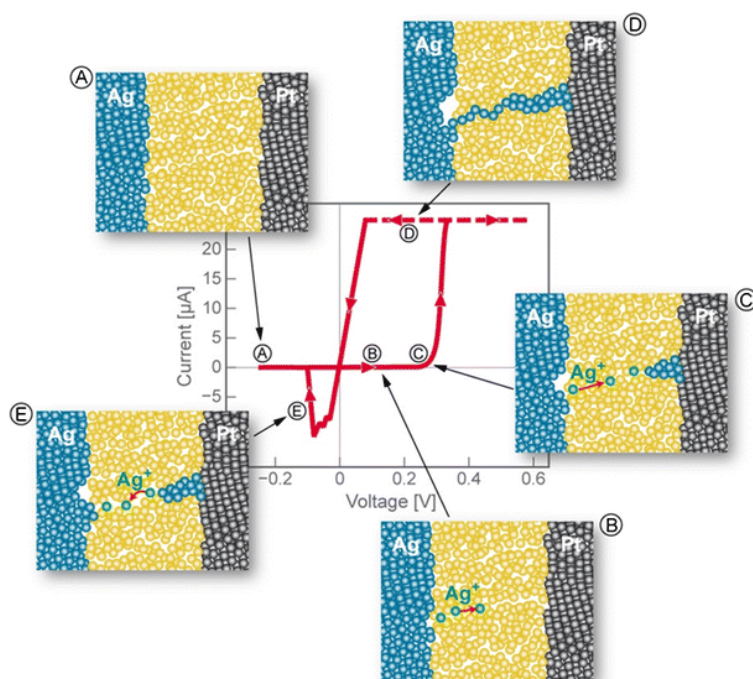


Figure 2.1 Schematic diagram of electrochemical reactions in a memristor when applying an electrical bias adapted from ²⁰.

The electrochemical mechanism of Ag migration in gate dielectric materials under electrical bias has still been actively explored. What the mobile species are, and where (location), why (driving force) and how (microscopic picture) they are moving under electrical excitations need to be addressed. Not only indirect analysis such as IV curves, but direct analysis such as AFM, or in-situ TEM, STEM are required ²¹⁻²³. There are four main ionic transport mechanisms shown in Figure 2.2: drift due to the electric potential gradient, electromigration due to electron kinetic energy, Fick's diffusion due to the concentration gradient, and thermophoresis due to the temperature gradient. The energy gradient from an electrode to the counter electrode during voltage application drives any ion migration. Not only the electric potential but also kinetic, chemical, and thermal energy are altered under bias. Therefore, the system can be very complicated to interpret the ion migration effect.

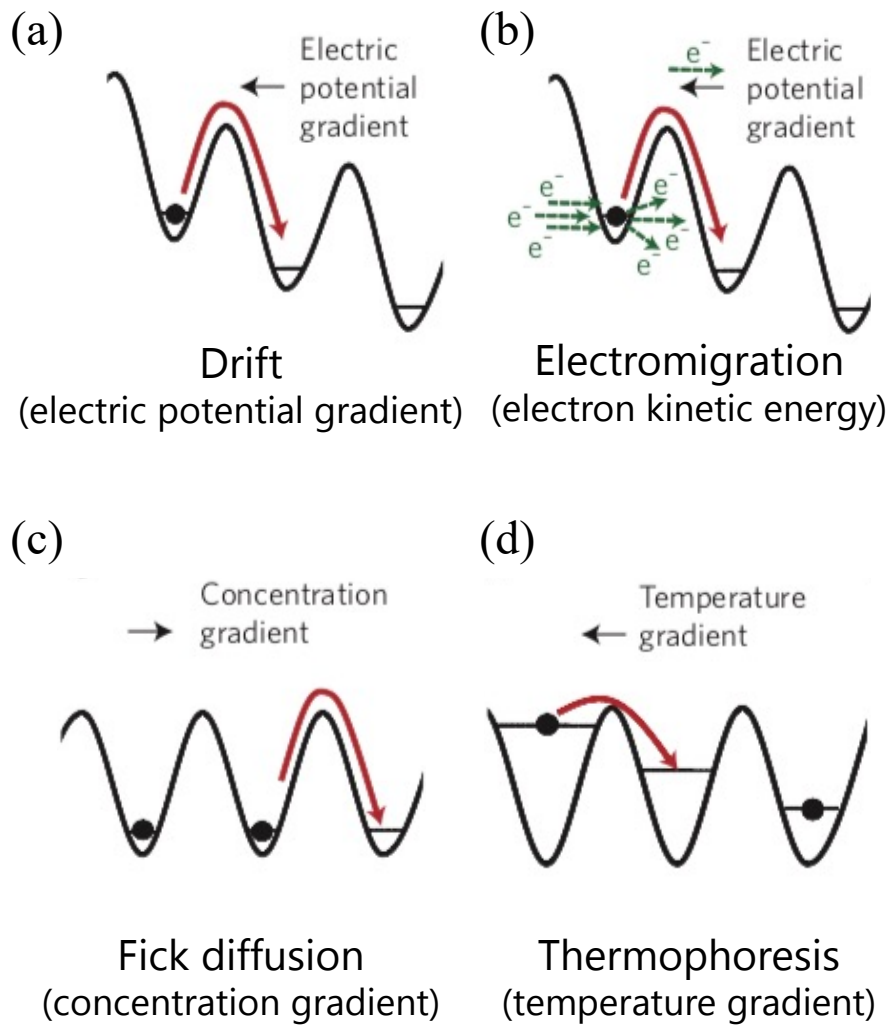


Figure 2.2 General ionic transport mechanisms: (a) Drift (b) Electromigration (c) Fick's diffusion (d) Thermophoresis, adopted from ²⁴.

Table 2.1 Development and demonstration of optical memristors, and their properties and mechanisms. References^{25–32}

| | Active electrode | Electrolyte | Passive electrode | Mobile species | dominant | Wavelength (nm) | Voltage (V) |
|---|------------------|--------------------------------|-------------------|----------------|-------------------|-----------------|-------------|
| 1 | - | SiO ₂ | Au, ITO | anion | E-field | 1550 | -3 – 3 |
| 2 | - | ZnO | Al, Si | anion | E-field + heating | 5000 – 18000 | -6 – 6 |
| 3 | Ag | a-Si | p-Si | cation | E-field | 1500 | -3 – 9 |
| 4 | Ag | a-Si | Pt | cation | E-field | 1549 | -0.25 – 1.5 |
| 5 | Cu | Cu ₂ S | Pt | cation | E-field | 1000 – 5000 | -0.5 – 1 |
| 6 | Ag/ITO | SiO ₂ | Au | cation | E-field | 400 – 800 | -5 – 10 |
| 7 | Ag | Al ₂ O ₃ | Au | cation | E-field | 400 – 2000 | 0 – 3 |
| 8 | Ag | Al ₂ O ₃ | ITO | cation | E-field + heating | 500 – 800 | 0 – 0.005 |

Due to the exceptional properties of memristors and their technological potential^{24,33–45}, the optics and photonics community has been searching for an optical analogue to such a device, known as the optical memristor^{25,27–32,46–55}. Silver or copper typically serve as active electrode materials, with silver ions or copper ions as the mobile cations responsible for forming the conductive filaments^{56–59}. In certain cases, oxygen ions in the dielectric can also function as the mobile species, particularly when both electrodes are inert, as demonstrated in^{27,48}. By forming and dissolving the conductive filaments, a distinctive hysteresis loop can be observed in the current-voltage curve within the voltage range. Due to the tight confinement of the mode within the waveguide, the optical memristor is highly sensitive to filament formation and disruption within the medium. The resonance wavelength or amplitude is modulated in the visible wavelength in response to the electrical bias, as the conductive filament formation strongly perturbs the plasmonic mode.

However, these devices require complex resonance structures, such as waveguides, to tightly confine light and enhance the sensitivity to detect small changes in the

formation and deformation of filaments in the dielectric layer. Here, we suggest a different mechanism for an optical memristor device: a refractive index change in ITO induced by the electrochemical reaction of Ag and Ag ion transport through the gate dielectric and ITO under an applied electrical bias. In this case, the device does not rely solely on the formation of nanometer-sized filaments, but the optical property of the entire ITO layer is modulated, allowing for a simpler device design while still achieving large modulation. Prior research showed that Ag ions are transported through the gate dielectric layer and reduced in the ITO layer^{32,60}.

2.2 Simulations

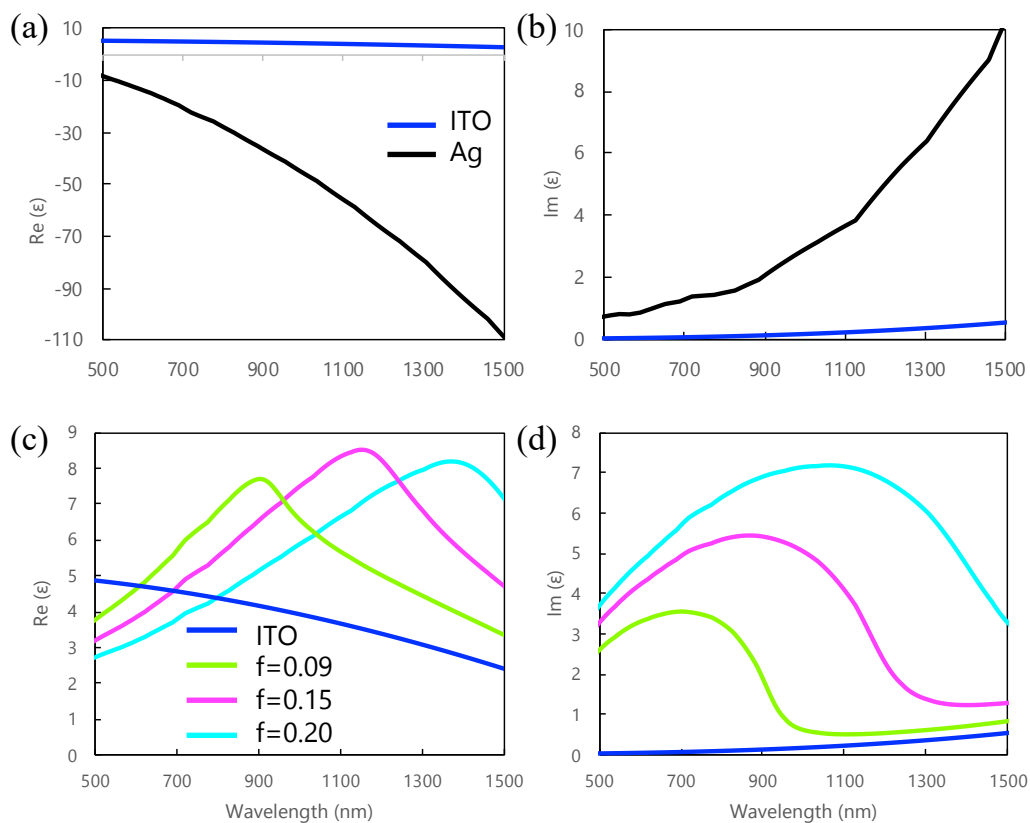


Figure 2.3 (a) Real part and (b) Imaginary part of the dielectric function of ITO and Ag as a function of wavelength. (c) Real part and (d) Imaginary part of the dielectric function of Ag-embedded ITO at different fill fractions of Ag as a function of wavelength.

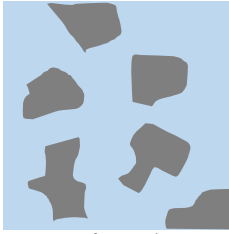
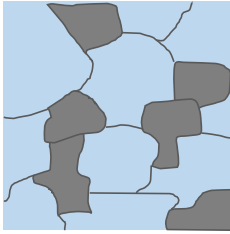
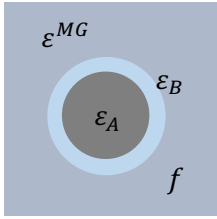
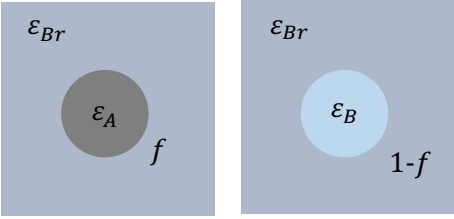
Figure 2.3 (a)-(b) shows the real and imaginary parts of the dielectric function of ITO and Ag as a function of wavelengths in the visible to near-infrared (NIR) range. The dielectric function of Ag was taken from Palik data⁶¹. The dielectric function of ITO was calculated using the Drude model with an assumed carrier concentration of $5 \times 10^{20} \text{ cm}^{-3}$. Ag exhibits optically metallic properties, with a negative real part and a large imaginary part of the dielectric function, while ITO can be either optically metallic or dielectric, depending on the oxygen vacancies and carrier

concentration in the material. The optical properties of Ag embedded in ITO were addressed by modeling the Bruggeman effective medium ⁶² (Table 2.2). In this model, it is assumed that a certain amount of Ag is homogeneously mixed in the ITO, following the equation 2.1:

$$f \frac{\varepsilon_{Ag} - \varepsilon_{Br}}{\varepsilon_{Ag} + 2\varepsilon_{Br}} + (1 - f) \frac{\varepsilon_{ITO} - \varepsilon_{Br}}{\varepsilon_{ITO} + 2\varepsilon_{Br}} = 0 \quad 2.1$$

Here, f is the volume fraction of Ag, ε_{Ag} and ε_{ITO} are the dielectric constants of Ag and ITO, respectively, and ε_{Br} is the dielectric constant of the Ag-embedded ITO mixture. By changing the fill fraction of Ag (f), distinct values of ε_{Br} can be calculated, as seen in Figure 2.2 (c)-(d). As Ag and ITO have distinctive dielectric functions, the dielectric function of the mixture can be largely modulated depending on the fill fraction of Ag.

Table 2.2 Maxwell Garnett model and Bruggeman model for mixtures of materials A and B.

| Maxwell Garnett model | Bruggeman model |
|---|---|
|  Separated-grain structure |  Aggregate structure |
|  $f = \text{Ratio of volumes}$ |  $f = \text{Probability of being A}$ |
| $\frac{\varepsilon^{MG} - \varepsilon_B}{\varepsilon^{MG} + 2\varepsilon_B} = f \frac{\varepsilon_A - \varepsilon_B}{\varepsilon_A + 2\varepsilon_B}$ | $f \frac{\varepsilon_A - \varepsilon_{Br}}{\varepsilon_A + 2\varepsilon_{Br}} + (1 - f) \frac{\varepsilon_B - \varepsilon_{Br}}{\varepsilon_B + 2\varepsilon_{Br}} = 0$ |

Referring to previous research in ³², the reflectance modulation in the NIR wavelengths of the planar structure is calculated by transfer matrix calculation using Lumerical FDTD. By applying an electrical bias, Ag is transported and embedded in the ITO, forming a mixture with a different fill fraction of Ag depending on the applied voltage (Figure 2.4 (a)). Based on this assumption, the reflectance can be largely modulated around 1570 nm, ranging from 7% to 92%.

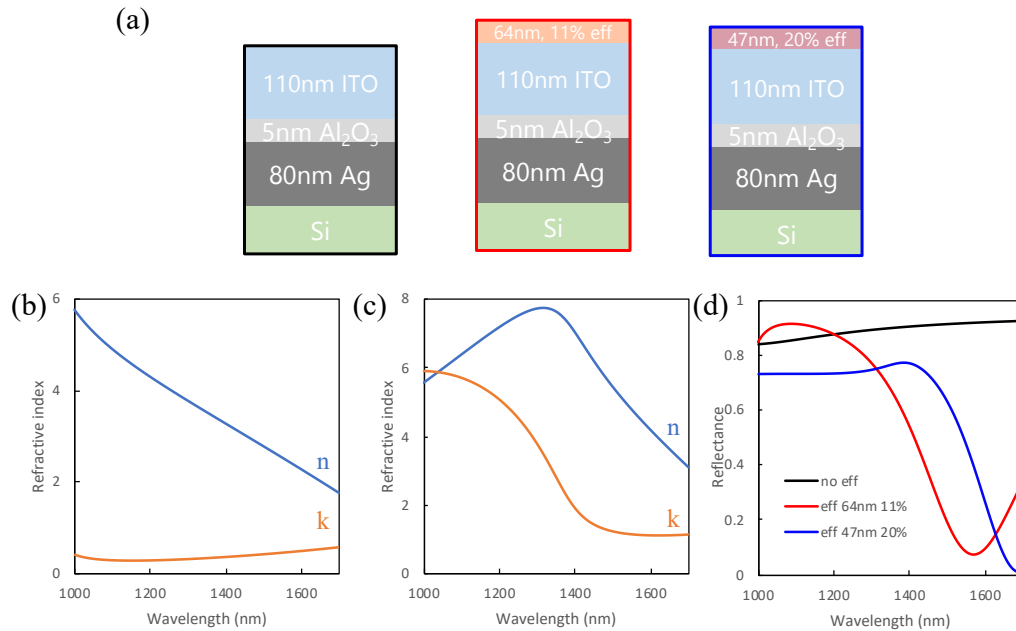


Figure 2.4 (a) Schematic diagram of three different stacks with different fill fractions of Ag. (b) Calculated refractive index of ITO with 11% Ag embedded. (c) Calculated refractive index of ITO with 20% Ag embedded. (d) Reflectance spectrum calculated by transfer matrix calculation. Each color in the graph corresponds to the schematics in (a).

With the assumption of calculated values, the device exhibits large potential as an optical modulator, even with a simple planar structure utilizing electrochemical reactions in the Ag/gate dielectric/ITO stack. The following sections demonstrate

whether this concept is experimentally realized in terms of optical response and electrical response.

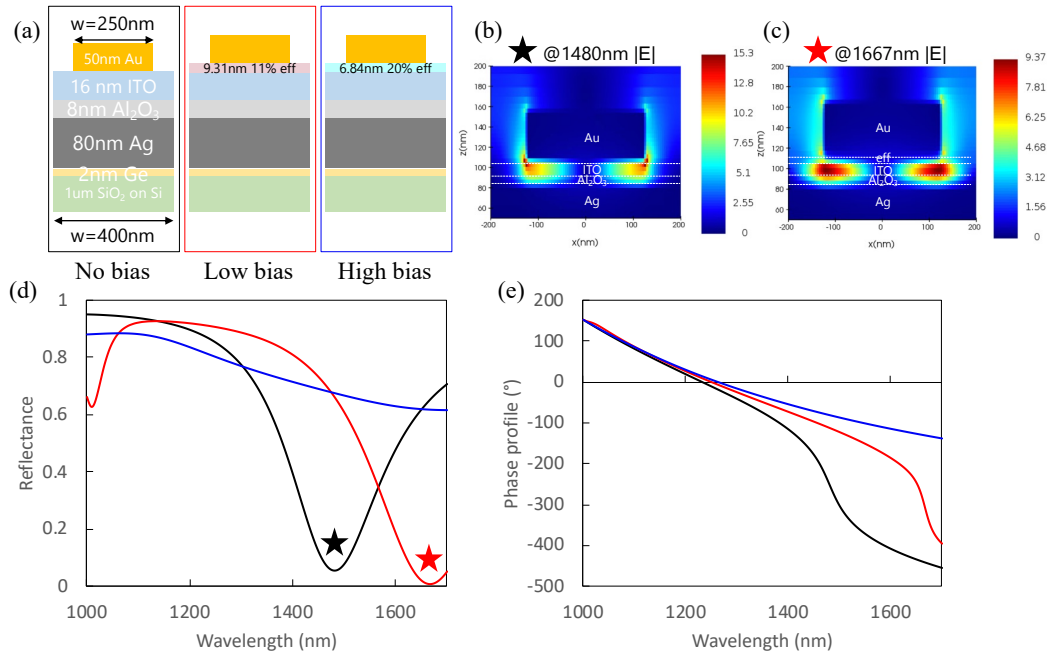


Figure 2.5 (a) Schematic diagram of a unit cell of Au stripe metasurfaces with three different stacks with varying fill fractions of Ag: 1) No effective medium when no applied bias, 2) 11% Ag embedded effective medium implying a low bias, 3) 20% Ag embedded effective medium implying a high bias. (b) Spatial distribution of the electric field amplitude in the metasurface unit cell in the x - z direction at a wavelength of 1480nm when there is no applied bias. (c) Spatial distribution of the electric field amplitude in the metasurface unit cell in the x - z direction at a wavelength of 1667nm when a low voltage is applied. (d) Reflectance spectrum in the near-infrared (NIR) region around the resonance wavelengths. (e) Corresponding phase profile.

In Figure 2.5, simulations were conducted on a resonant structure integrated with the Ag/ Al_2O_3 /ITO planar structure to confine the light at a specific wavelength and

effectively modulate the reflectance and phase. A periodic Au stripe with a width of 250 nm and a height of 50 nm was introduced on a planar structure. Without any bias application, the electric field is tightly confined at the edge of the Au stripe at the interface between Au and ITO, as shown in Figure 2.5(b). When applying a bias, Ag starts to migrate into Al_2O_3 and diffuse into ITO, eventually forming an effective medium. Here, a 9.31 nm-thick layer of ITO embedded with 11% Ag was assumed. The values were adopted from a previous work in reference 63. The resonance was strongly shifted by 187 nm, from 1480 nm to 1667 nm, due to the formation of an effective medium layer, and the corresponding electric field is shown in Figure 2.5(c). Now, the electric field is tightly confined within the ITO layer. When the Ag fill fraction increases to 20%, the effective medium acts more like a metallic layer, and the mode from the Au stripe is no longer confined, resulting in the absence of a resonance peak and maintaining a high reflectance in the NIR. Figure 2.5(e) shows the corresponding phase profile. Approximately a $3/2\pi$ phase shift was achieved. In this simulation study, it was proposed that an Ag-embedded ITO layer, the effective medium layer, can significantly perturb the electric field and drive substantial reflectance and phase modulation in the NIR region.

A different case was studied with Lumerical FDTD simulations. Above, Ag diffusion into ITO was crucial to drive the optical modulation under the electrochemical reaction with electrical bias. On the other hand, Ag filament growths within the Al_2O_3 layer can also drive the optical modulation under Ag filament formation and disruption with electrical bias. In this case, the filaments themselves can act as plasmonic structures. For example, simulation results with an Ag stripe metasurface with induced filament formation having a 100 nm-wide rod in a 25 nm-thick Al_2O_3 layer are shown in Figure 2.6. In the simulations, it was assumed that the Ag filaments are densely packed and uniformly, periodically aligned in the x-direction to simplify the effect of Ag filaments in the structure. While forming or rupturing the filaments when applying the set and reset voltages,

extra gap plasmons can be induced, as shown in Figures 2.6 (b) and (c), in addition to plasmons from the Ag stripe structures. Figures 2.6 (j) and (k) show narrower resonance peaks in the NIR region.

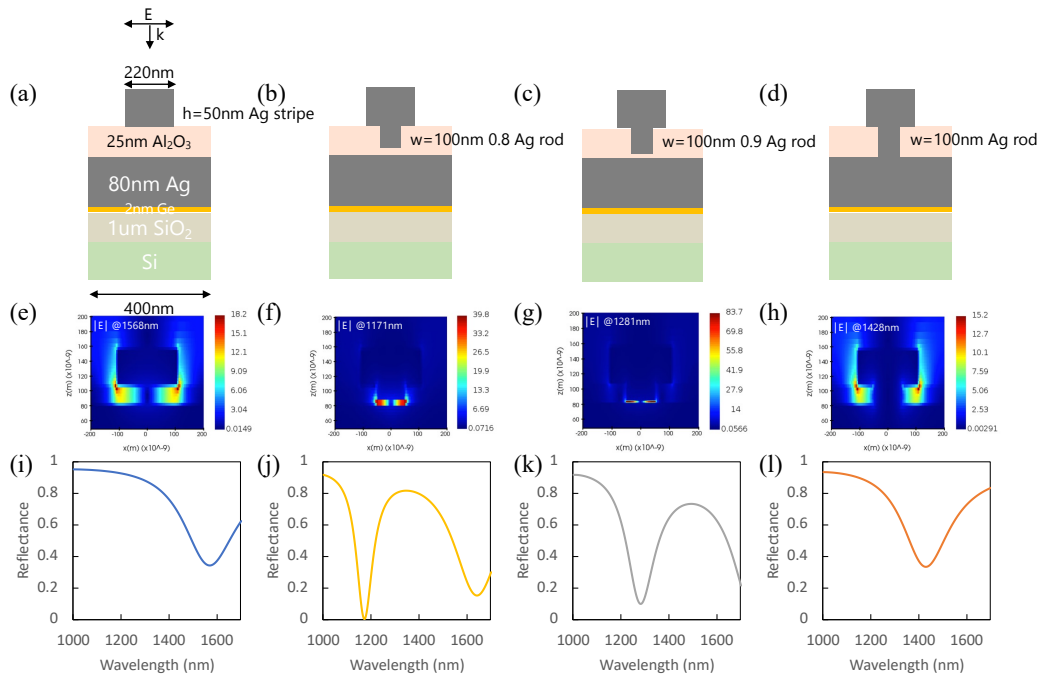


Figure 2.6 Simulation results of Ag stripe metasurfaces for amplifying the effect of Ag filament growth and rupture: (a) No filament. (b) 80% growth of the Ag filament within the dielectric. (c) 90% growth of the Ag filament within the dielectric. (d) 100% growth of the Ag filament within the dielectric. (e)-(h) Corresponding absolute electric field distribution of the unit cell of the metasurface. (i)-(l) Corresponding reflectance spectrum in the near-infrared (NIR) region.

In simulation works, two distinct cases for optical modulation were studied. 1) Ag diffused into the ITO layer, forming a mixture layer that induces a refractive index change in the ITO and perturbs the electric field. 2) Ag filament growths within a dielectric layer due to Ag ion migrations and reduction induce variations in

plasmonic modes. These simulation studies proposed that both mechanisms, the formation of an Ag-embedded effective medium layer and the growth of Ag filaments within a dielectric, can significantly modulate the optical properties, such as reflectance and phase, in the near-infrared region. However, these simulation results need to be experimentally demonstrated to validate the proposed mechanisms and their effectiveness in achieving optical modulation.

2.3 Device fabrication

2.3.1 Ultrasmooth Ag and Al₂O₃ depositions

To apply an electrical bias through the device and initiate ion migration, the gate dielectric should be ultra-smooth without any pinholes within the layer to prevent current leakage. The roughness of the gate dielectric can be significantly influenced by the underlying layer or substrate. In this case, the bottom layer is silver (Ag), and an ultra-smooth Ag layer is crucial for obtaining a pinhole-free, ultra-smooth gate dielectric over the entire active area.

An 80 nm-thick Ag layer is deposited on a 1 μm-thick silica-on-silicon substrate. This thickness of 80 nm ensures optically thick, allowing Ag to serve as both a back reflector in the visible to near-infrared wavelengths and a back electrode. Ag is deposited by electron-beam evaporation. For ultra-smooth Ag deposition, various deposition parameters are considered, including beam shape, deposition rate, and deposition temperature. Furthermore, surface activation prior to the main Ag deposition is considered crucial, including surface cleaning, plasma treatment, deposition of a thin adhesion layer (seed layer), and deposition of a thin layer of Ag oxide.

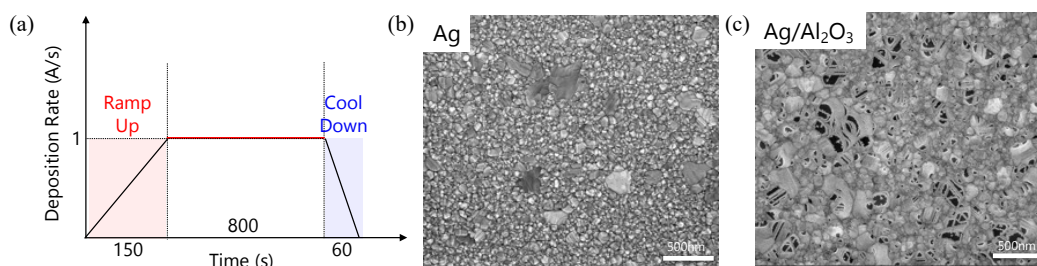


Figure 2.7 (a) General Ag deposition recipe. (b) SEM image of the surface after 80 nm Ag deposition. (c) SEM image of a 5 nm-thick alumina surface on Ag.

The general Ag deposition recipe involves a deposition rate of 1 \AA/s under a vacuum of 1×10^{-7} Torr. The detailed recipe is shown in Figure 2.7(a). During the ramp-up phase, the deposition rate gradually increases through a series of ramp and soak processes. The total deposition duration is approximately 1000 seconds. Figure 2.7(b) shows a scanning electron microscopy (SEM) image of the Ag surface after deposition, revealing the formation of Ag islands on the surface. The growth of metal films initiates with islands following the Volmer-Weber mechanism (Figure 2.8(a)).⁶³ These islands form on the substrate as the interaction between Ag film atoms is stronger than the interaction between adjacent film and substrate atoms (Figure 2.8(b)). When a 5 nm-thick alumina (Al_2O_3) layer is deposited onto this island-growth Ag layer by atomic layer deposition (ALD), a high density of pinholes is observed in the SEM image shown in Figure 2.7(c). To analyze the surface roughness in three dimensions, atomic force microscopy (AFM) is employed. The size of the Ag islands varies from 100 nm to 1000 nm in one direction, and the root mean square (RMS) roughness of the layer exceeds 1.5 nm, indicating a rough surface (Figure 2.9(a)). Figure 2.9(b) shows the surface profile of the Al_2O_3 layer with pinholes, exhibiting a large RMS roughness of over 5 nm. Three different pinholes, each approximately 100 nm wide in one direction, are closely analyzed with depth profiles. The depth of the pinholes exceeds the thickness of the alumina, implying that the gate dielectric is leaky or even shorted, as the pinholes will be filled with the top electrode material, directly forming bridges between the bottom and top electrodes.

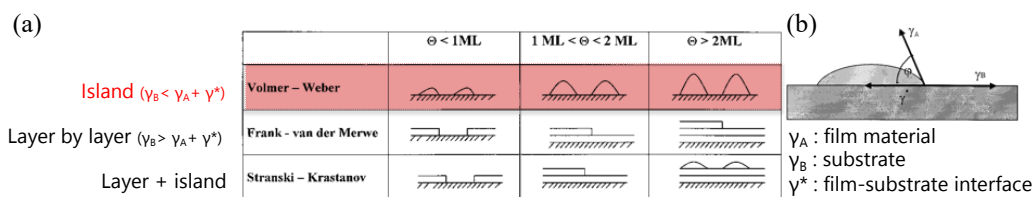


Figure 2.8 (a) Thin film growth mechanisms. (b) Surface energy at the interface and the wetting angle.⁶³

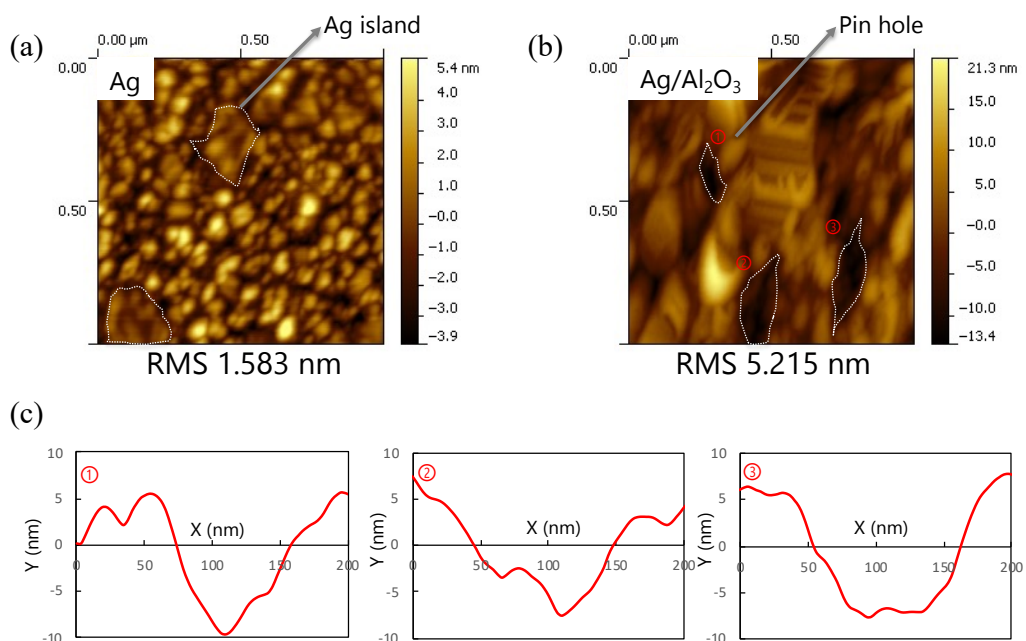


Figure 2.9 Surface topological image of (a) Ag, (b) Al₂O₃, (c) Depth profiles at three different points indicated in (b), all analyzed by AFM.

To further improve surface smoothness, surface cleaning and oxygen plasma treatment are conducted prior to any deposition on the substrate⁶⁴. The substrate is cleaned using the RCA cleaning method, as well as sonication soaking in acetone for 10 minutes and isopropyl alcohol (IPA) for 10 minutes. Oxygen plasma treatment is performed using a plasma asher with an RF power of 400 W at a pressure of 400 mTorr for 1 minute for surface activation. Plasma treatment slightly improves the surface smoothness of Ag, as seen in Figure 2.10.

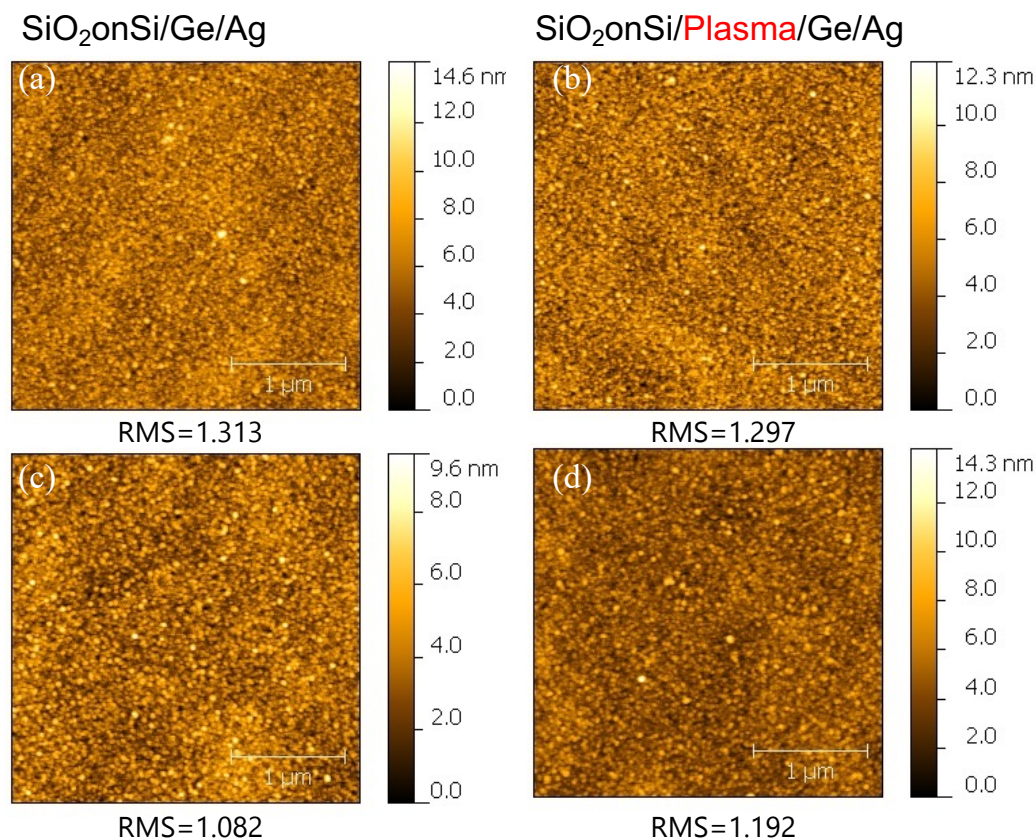


Figure 2.10 Effect of oxygen plasma treatment on roughness of Ag and Al_2O_3 measured by AFM (a) Ag without plasma treatment, (b) Ag with plasma treatment, (c) Al_2O_3 on Ag without plasma treatment, (d) Al_2O_3 on Ag with plasma treatment.

To remove pinholes in the dielectric layer, the islands need to be eliminated from the Ag layer^{63,65–68}. The effect of transition metal seed layers is investigated using various materials, including titanium (Ti), chromium (Cr), and germanium (Ge). A 1 nm-thick seed layer is deposited at a deposition rate of 0.5 Å/s, followed by Ag deposition without a vacuum break in the electron-beam evaporation chamber. When using Ti as a seed layer (Figure 2.11(b)), the size of the islands decreases compared to depositing Ag without any seed layer (Figure 2.11(a)), but islands still exist. When using Cr as a seed layer (Figure 2.11(c)), the density of islands decreases compared to depositing Ag without any seed layer, but the size of the

islands remains as large as in the Ag-only deposition. When using Ge, there are no islands in the Ag layer. SEM images are analyzed again after depositing a 5 nm-thick Al_2O_3 layer on each Ag surface with a seed layer (Figure 2.12).

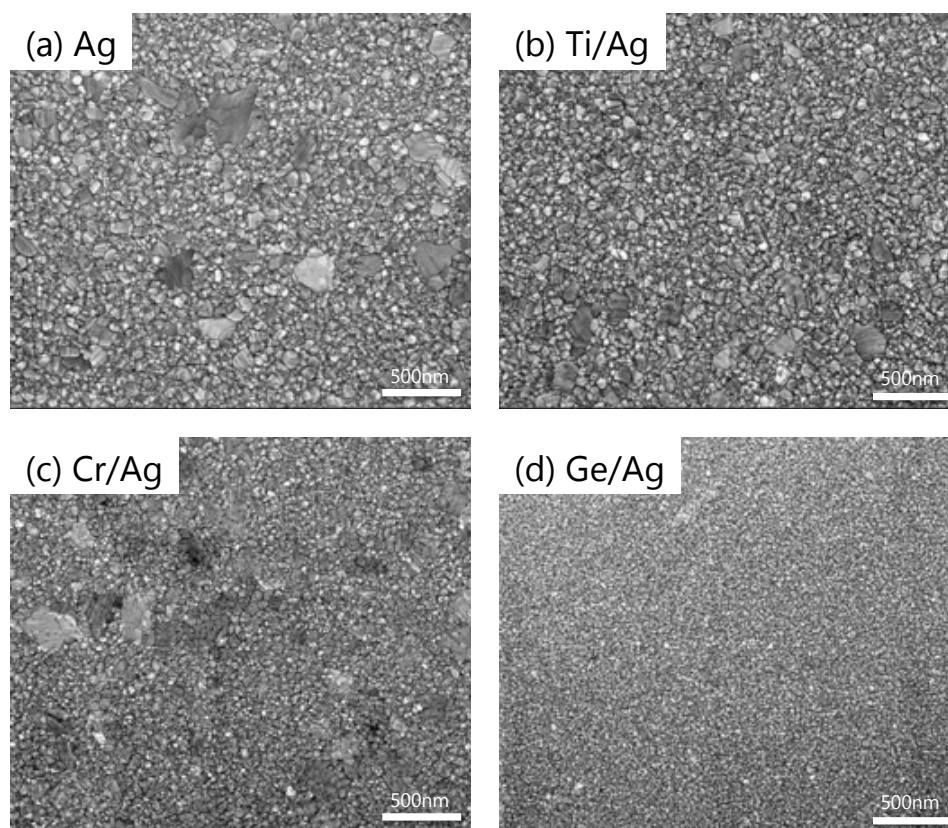


Figure 2.11 Effect of seed layers on the roughness of Ag analyzed by SEM: (a) Ag only without any seed layer, (b) 1 nm Ti/80 nm Ag, (c) 1 nm Cr/80 nm Ag, (d) 1 nm Ge/80 nm Ag.

As expected, when islands are present in the Ag layer, the subsequent Al_2O_3 layer exhibits numerous pinholes, but there are no pinholes on the Ge/Ag surface, as the surface is smooth enough (Figure 2.12(d)). These seed materials deposited on the SiO_2 -on-Si substrate also undergo Volmer-Weber growth mode⁶⁷, but the density of nuclei is much higher, and the islands are significantly smaller than those for Ag

deposited directly on the substrate, leading to an ultra-smooth Ag surface. The decreased sum of surface energy in the seed layer and seed material-substrate interface, compared to the surface of the substrate, contributes to a smoother Ag surface. However, it should be noted that Ge atoms have been reported to segregate through Ag grain boundaries towards the free surface of the metal over time, which needs to be considered⁶⁹⁻⁷¹.

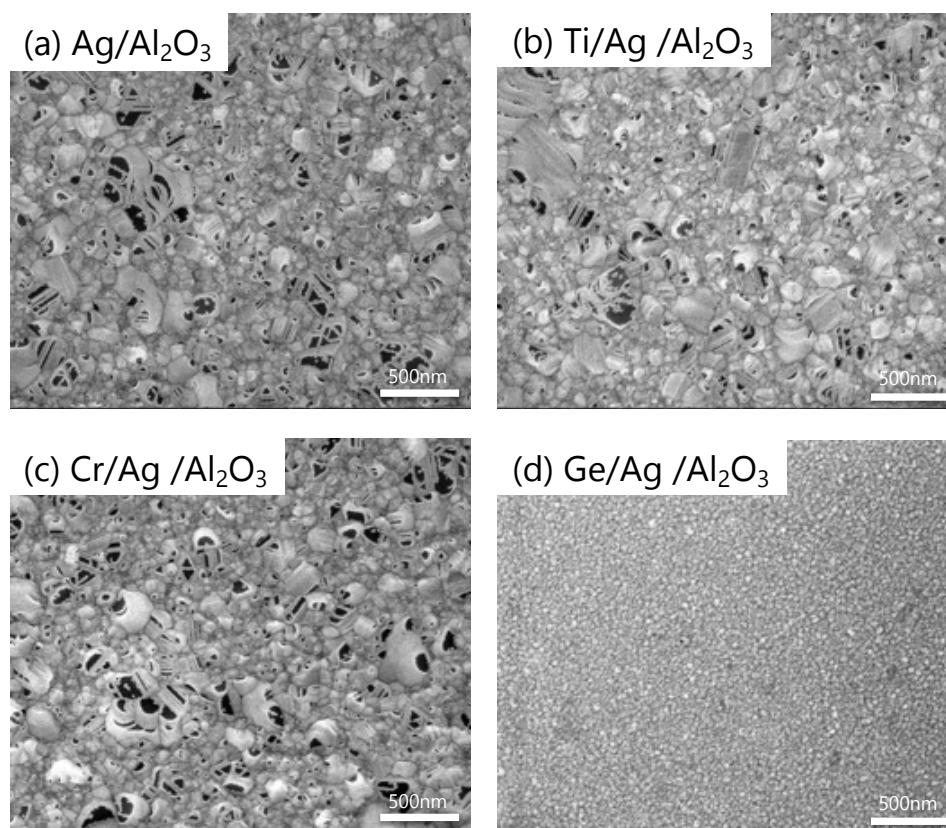


Figure 2.12 Effect of seed layers on the roughness of Al₂O₃ analyzed by SEM: (a) Ag/5 nm Al₂O₃ without any seed layer, (b) 1 nm Ti/80 nm Ag/5 nm Al₂O₃, (c) 1 nm Cr/80 nm Ag/5 nm Al₂O₃, (d) 1 nm Ge/80 nm Ag/5 nm Al₂O₃.

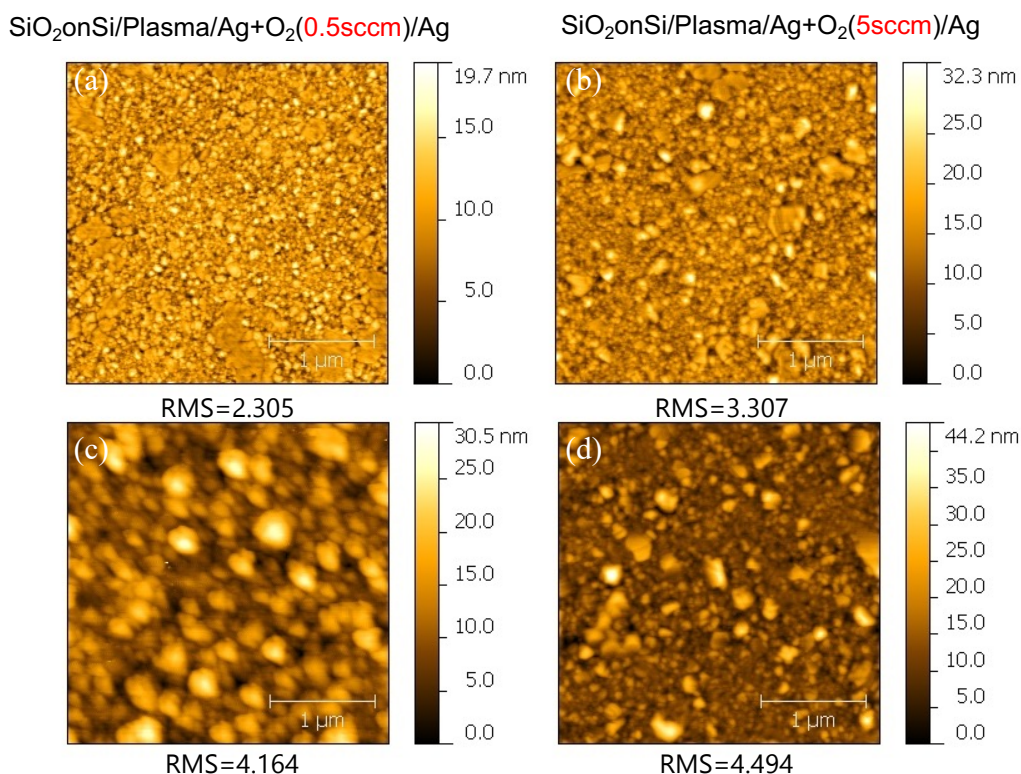


Figure 2.13 Effect of oxygen flow rate during Ag deposition on the roughness of Ag and Al_2O_3 measured by AFM: (a) Ag with 0.5 sccm oxygen flow rate, (b) Ag with 5 sccm oxygen flow rate, (c) Al_2O_3 on Ag with 0.5 sccm oxygen flow rate, (d) Al_2O_3 on Ag with 5 sccm oxygen flow rate.

The effect of the Ag deposition rate on the surface roughness is also investigated. A slower deposition rate enhances the smoothness of the Ag layer, as evidenced by comparing Figures 2.14(a) and (b). When the surface is activated with Ag oxidation, the smoothness of the Ag layer is further improved, with a root-mean-square (RMS) roughness of approximately 0.8 nm. The subsequent Al_2O_3 layer exhibits no pinholes and is ultra-smooth, with an RMS roughness of less than 0.7 nm. The line profiles of the optimized layers in Figures 2.14(c) and (f), depicted in Figures 2.14(g) and (h), respectively, reveal a prominently small grain size of less than 50 nm and an averaged peak-to-valley height of less than 2 nm.

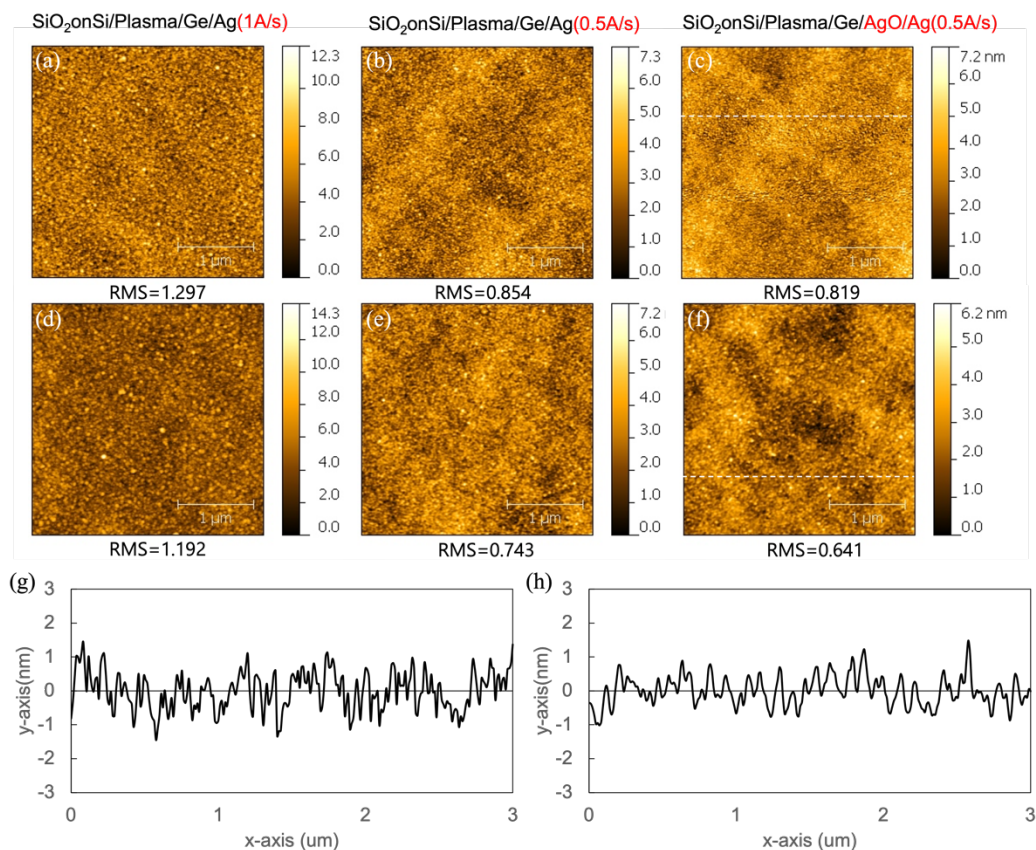


Figure 2.14 Effect of Ag deposition rate on the roughness of Ag and Al₂O₃ measured by Atomic Force Microscopy (AFM): (a) Ag deposited at 1 Å/s, (b) Ag deposited at 0.5 Å/s, (c) Ag deposited at 0.5 Å/s including 1 nm AgO, (d) Al₂O₃ on Ag deposited at 1 Å/s, (e) Al₂O₃ on Ag deposited at 0.5 Å/s, (f) Al₂O₃ on Ag deposited at 1 Å/s including 1 nm AgO, (g) Line profile represented by the linecut in (c), (h) Line profile represented by the linecut in (f).

Table 2.3 shows the overall Ag deposition recipes and the corresponding RMS roughness values of the Ag and Ag/Al₂O₃ surfaces measured by AFM. By activating the surface with oxygen plasma treatment, increasing surface wettability with a Ge seed layer, further activating the surface with the formation of a thin silver oxide layer, and depositing Ag at a slower deposition rate, an ultra-smooth Ag layer without any islands is achieved, leading to a pinhole-free Al₂O₃ layer.

Table 2.3 Overall Ag deposition recipes and corresponding roughness values of each layer, Ag, and Al₂O₃.

| | Ag deposition recipe | Before 5nm Al ₂ O ₃ RMS (nm) | After 5nm Al ₂ O ₃ RMS (nm) |
|----|--|---|--|
| 1 | SiO ₂ onSi/Plasma/Ag+O ₂ (0.5sccm)/Ag(4A/s) | 2.305±0.213 | 4.164±0.795 |
| 2 | SiO ₂ onSi/Cr/Ag(1A/s) | 2.603±0.294 | 5.605±1.801 |
| 3 | Si/Al ₂ O ₃ /Plasma/Ag+O ₂ (5sccm)/Ag(4A/s) | 2.934±0.362 | 3.722±1.348 |
| 4 | SiO ₂ onSi/Plasma/Ag+O ₂ (5sccm)/Ag(4A/s) | 3.420±0.530 | 4.595±1.141 |
| 5 | Si/Plasma/Ag+O ₂ (5sccm)/Ag(4A/s) | 3.307±0.472 | 4.494±1.046 |
| 6 | SiO ₂ onSi/Plasma/Ge/Ag(1A/s) | 1.297±0.116 | 1.192±0.109 |
| 7 | SiO ₂ onSi/Ge/Ag(1A/s) | 1.313±0.118 | 1.082±0.099 |
| 8 | SiO ₂ onSi/Plasma/Ag+O ₂ (5sccm)/Ag(0.5A/s) | 1.593±0.131 | 2.357±0.674 |
| 9 | SiO ₂ onSi/Plasma/Ge/Ag(0.5A/s) | 0.854±0.071 | 0.743±0.080 |
| 10 | SiO ₂ onSi/Plasma/Ge/Ag+O ₂ (0.5sccm)/Ag(0.5A/s) | 0.819±0.085 | 0.641±0.065 |

It is noteworthy that the depositions were processed using a graphite crucible, requiring only 6% of the power to melt Ag with the electron beam. The crucible material is important because the thermal conductivity of the crucible material is distinctive, requiring different power levels to melt the material being deposited, which impacts the chamber temperature during deposition. When using a molybdenum crucible, 19% of the power is required to deposit Ag. The higher the power during deposition, the higher the increase in the chamber temperature. The deposition temperature affects the grain size of the Ag layer. By comparing Figure 2.15(a) and (b), the grain size is larger when using the molybdenum crucible due to the increased deposition temperature compared to when using the graphite crucible. In the evaporation system used, the chamber temperature could not be controlled during deposition. However, better smoothness is expected if the deposition temperature is lower during deposition with a cooling system.

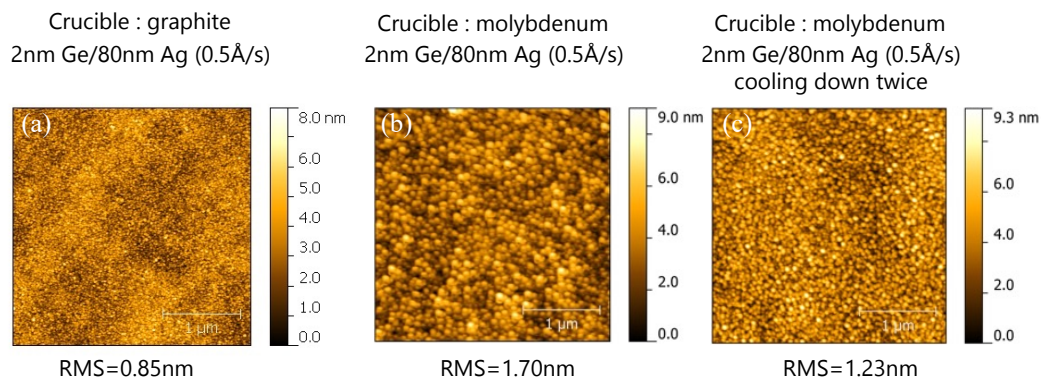


Figure 2.15 Effect of Ag crucible on the roughness of Ag measured by AFM: (a) 2 nm Ge/80 nm Ag with a graphite crucible, (b) 2 nm Ge/80 nm Ag with a molybdenum crucible, (c) 2 nm Ge/80 nm Ag with a molybdenum crucible, cooling down twice to lower the chamber temperature during deposition.

2.3.2 Electrical and optical properties of sputtered ITO

The electrical and optical properties of the sputtered ITO are affected by the deposition conditions, especially the oxygen flow rate during deposition⁷²⁻⁷⁹. The dielectric constant of ITO as a function of wavelength can be expressed as:

$$\varepsilon_{ITO}(\omega) = \varepsilon_{\infty} - \frac{\omega_p^2}{\omega^2 + i\omega\Gamma} \quad 2.2$$

$$\omega_p^2 = \frac{Nq^2}{\varepsilon_0 m^*} \propto N \quad 2.3$$

$$\rho_{ITO} = \frac{1}{q\mu N} = \frac{m^*\Gamma}{Nq^2} \quad 2.4$$

where ε_{∞} is the high frequency permittivity, Γ is the damping rate, ω_p is the plasma frequency, N is the carrier concentration, q is the electron charge, ε_0 is the dielectric permittivity of vacuum, m^* is the effective mass, ρ is the resistivity, and μ is the electron mobility.

Following these equations from 2.2 to 2.4, the electrical (ρ_{ITO}) and optical (ε_{ITO}) properties of the ITO are dependent on the carrier concentration in the ITO layer. The main carriers in ITO are oxygen vacancies. If the oxygen flow rate is increased during sputtering, the oxygen vacancies in the ITO decrease, leading to a lower carrier concentration. The concentration can be controlled by adjusting the oxygen flow rate. The relationship between the oxygen flow rate and carrier concentration was experimentally demonstrated in previous works^{80,81} and it is replotted in the Figure 2.16.

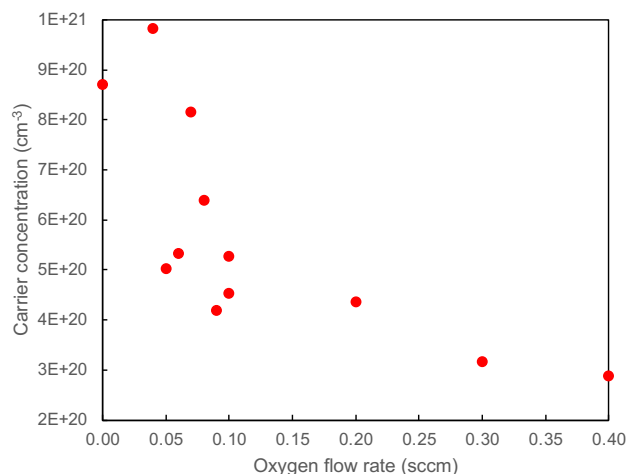


Figure 2.16 Carrier concentration in the ITO as a function of oxygen flow rate during the sputtering deposition process. The graph is replotted from ^{80,81}.

To avoid device shorts due to built-in charges, the work function of the ITO was considered. The work function of ITO is known to be tunable from 4.2 to 5 eV. It is hypothesized that if the work function of the ITO layer is significantly higher than that of silver, it could potentially result in the presence of built-in charges even before applying any bias, thus contributing to high leakage current. To address this concern, the oxygen flow rate during the sputtering process was reduced. This adjustment led to an increase in the carrier concentration, ultimately resulting in the reduction of the ITO's work function. While the work function was not directly measured, the carrier concentration, mobility, and refractive index of our ITO layer were verified. Based on our observations, we can infer that the reduction in the work function was achieved, aiming to minimize the occurrence of built-in charges. Figure 2.17 (a)-(b) shows the difference in band diagrams when the ITO has high and low work functions (WF). The corresponding refractive indices of the ITO as a function of wavelength were measured by ellipsometry and Hall measurements (Figure 2.17 (c)-(d)). The following electrical and optical responses with these devices will be addressed in the next sections.

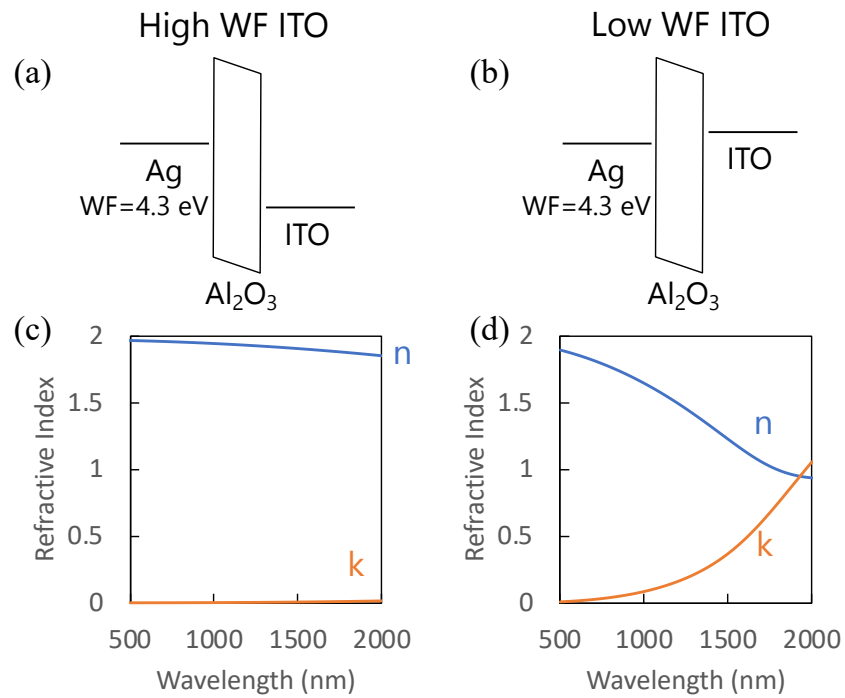


Figure 2.17 Band diagram when the ITO has (a) a high work function (WF) and (b) a low WF. Refractive index of (c) high WF ITO with a low carrier concentration of $4 \times 10^{19} \text{ cm}^{-3}$ and high mobility of $50 \text{ cm}^2/\text{Vs}$, and (d) low WF ITO with a high carrier concentration of $4.5 \times 10^{20} \text{ cm}^{-3}$ and low mobility of $13 \text{ cm}^2/\text{Vs}$.

2.3.3 Whole device stack

After optimizing the deposition parameters of each layer, the whole stack was integrated into a chip. Figure 2.15(a) shows an SEM image of the cross-sectional view of the stack. In addition to Al_2O_3 , ALD-deposited HfO_2 and $\text{Al}_2\text{O}_3/\text{HfO}_2$ laminates were also studied. Before conducting electrical and optical measurements, Ag ion migration under bias was indirectly observed by energy dispersive spectroscopy (EDS) by comparing the relative amount of the Ag peak before and after applying a voltage. As seen in the Casino simulation results (Figure 2.15(b)), at an application energy of 6 keV, the material information gathered included not only ITO and Al_2O_3 but also contributions from the Ag layer. Therefore, while the EDS measurements do not provide quantitative information about Ag migration, they suggest that Ag was migrated inside the device, as most of the information was coming from the ITO.

To pattern bars on the SiO_2 -on-Si substrate, shadow masks were designed and used. Crossbar antenna devices were designed to effectively apply bias to the bottom Ag and top ITO electrodes through the gate dielectric (Figure 2.19(a)). The active area of this type of device is $500\ \mu\text{m}$ by $500\ \mu\text{m}$. As confirmed by AFM topographical images on different regions, the surface was ultra-smooth over the entire region (Figure 2.19(c)-(f)).

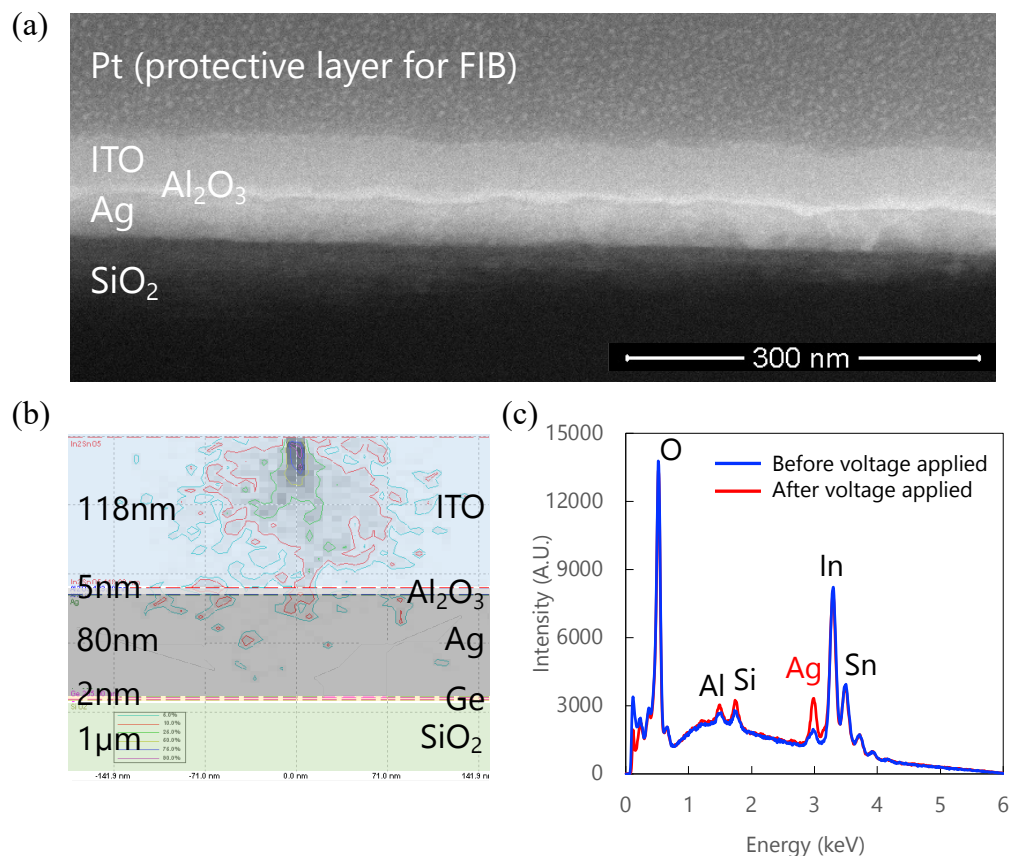


Figure 2.18 (a) Cross-sectional view measured by SEM. The device stack consists of an 80 nm-thick Ag layer, a 5 nm-thick Al₂O₃ layer, and a 118 nm-thick ITO layer on a 1 μm-thick SiO₂-on-Si substrate. (b) Energy distribution of EDS at 6 keV calculated by Casino simulation. (c) EDS analysis results before and after applying a voltage.

However, there were still issues with shorted devices even before applying any bias, despite the ultra-smooth layer depositions. To decrease the chance of having pinholes, the active area was reduced from 500 μm by 500 μm to 100 μm by 100 μm using an electron-beam pattern generator (EBPG) (Figure 2.20(a)-(b)). Alternatively, the area was further decreased to 5 μm by 5 μm.

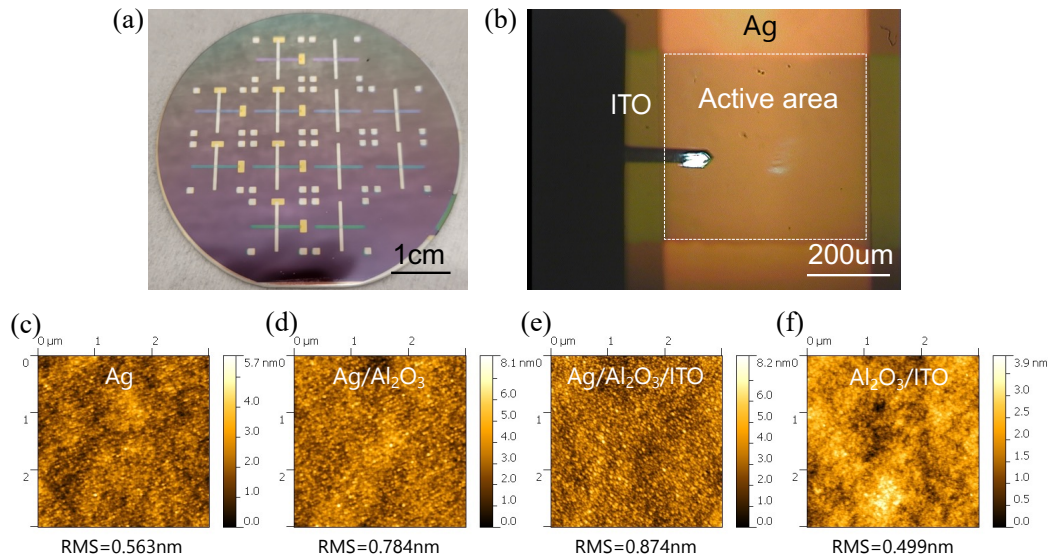


Figure 2.19 (a) Macroscopic image of a 2-inch wafer patterned using shadow masks. (b) Microscopic image of the active area, the Ag-ITO crossover region. (c)-(f) show AFM images of different regions: (c) Ag surface, (d) Al₂O₃ on Si surface, (e) ITO on Al₂O₃ on Ag surface, and (f) ITO on Al₂O₃ surface.

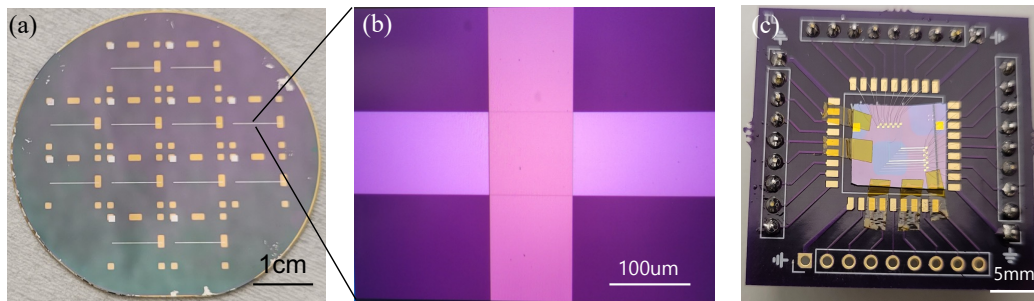


Figure 2.20 (a) Macroscopic image of a 2-inch wafer patterned using EBPG. (b) Microscopic image of the active area, the Ag-ITO crossover region. (c) Macroscopic image of a device connected to a printed circuit board (PCB).

Additionally, while investigating the shorted devices, it was found that excessive Ag was deposited at the edge of the pattern when a shadow mask or a single-layer

resist was used. The height of the Ag tail was over 5 nm, meaning that the Ag bottom electrode could directly contact the top ITO electrode because the gate dielectric was only 5 nm thick. To resolve this issue, a bilayer resist was used to improve the smoothness of the edge profile without having any Ag tails. Figure 2.21(d) and (f) show the proof of smooth deposition at the edge when a bilayer resist was used.

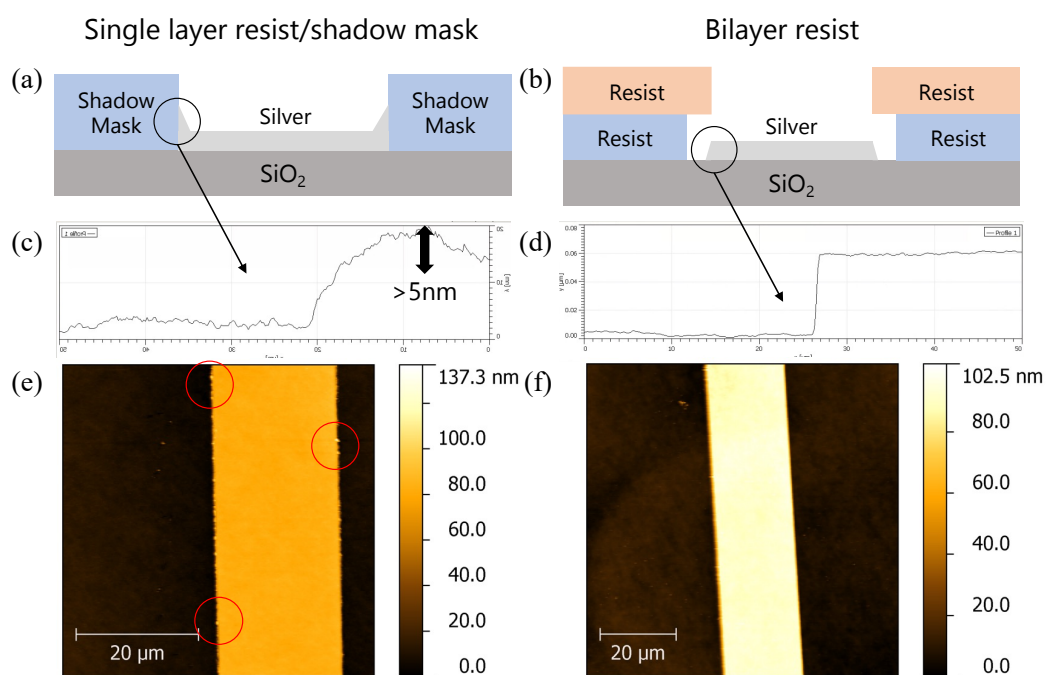


Figure 2.21 Schematic diagram of (a) when a single-layer resist or a shadow mask is used for patterning, and (b) when a bilayer resist is used for patterning. (c) Height profile and (e) topological image at the edge of the patterned Ag using a single-layer resist or a shadow mask. (d) Height profile and (f) topological image at the edge of the patterned Ag using a bilayer resist. (c)-(f) are measured by AFM.

2.4 Electrical response

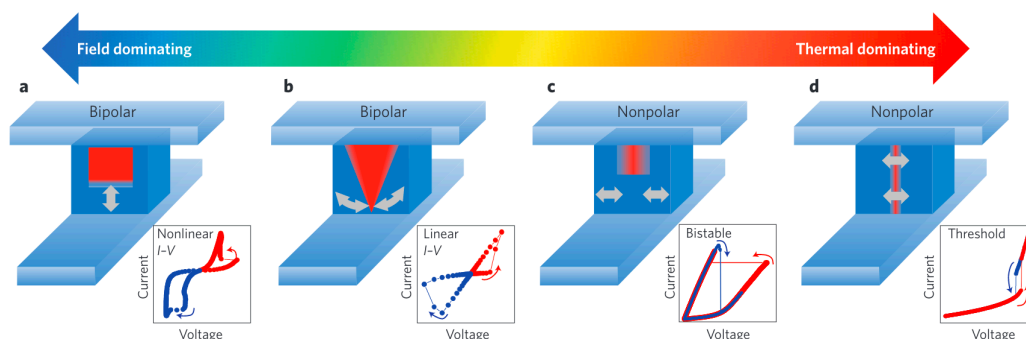


Figure 2.22 Four types of ion migration mechanisms, corresponding filament shapes, and IV curves adopted from ²⁴.

For the analysis of electrical responses in Ag/dielectric/ITO devices, a certain voltage was applied, and the current was measured with a specific compliance current using a probe station. If the current-voltage (I-V) curve exhibits a hysteresis loop, it implies that ions have migrated within the gate dielectric. If the I-V curve does not have a hysteresis loop but maintains a low current level, it implies that there is no ion migration or electrochemical reaction, and only charges are moving at the interface of the electrodes and the dielectric, behaving like a capacitor. Depending on whether the ion migrations are field-dominating or Joule heating-dominating, the IV characteristics are distinct. Figure 2.22 illustrates these ion migration mechanisms, corresponding filament shapes, and IV curves.

Depending on the ability to retain information, memristors can be categorized into two classes: volatile switching and nonvolatile switching (Figure 2.23). Volatile switching devices require periodic refreshing as a result of the loss of stored information. In this case, there is only one stable state without an external bias. On the other hand, nonvolatile switching devices can retain data for long periods, similar to conventional flash memory. By controlling the compliance current (C.C.), volatile and nonvolatile switching can occur in a single memristor ⁸³. Under low

C.C., thin and weak filaments are formed, leading to volatile switching behavior, while thick and strong filaments are formed under high C.C., leading to nonvolatile switching behavior.

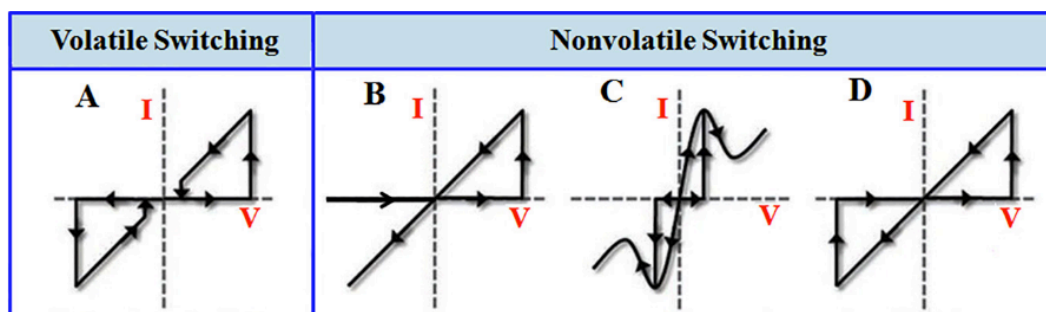


Figure 2.23 Schematic of the I-V characteristics for volatile and nonvolatile switching devices – A) volatile threshold switching, B) write-once-read-many (WORM) switching, C) unipolar switching, and D) bipolar switching behavior. Adopted from ⁸².

The active area of the devices in Figures 2.24 (a) and (g) was 100 μm by 100 μm , and the compliance current was set to 100 nA. To observe whether the carrier concentration in the ITO affects the electrical responses, five devices were analyzed, respectively. The ITO properties were elaborated in Figure 2.17. Although the devices were fabricated under the same conditions on the same 2-inch wafer, the device-to-device variation in I-V curves was substantial. Each device exhibited unique I-V characteristics, potentially due to variations in the surface roughness of the Ag or defects or weak pathways in the alumina layer at different positions. One notable observation is that the possibility of observing a hysteresis loop in the I-V curve is higher with devices having a high carrier concentration in the ITO.

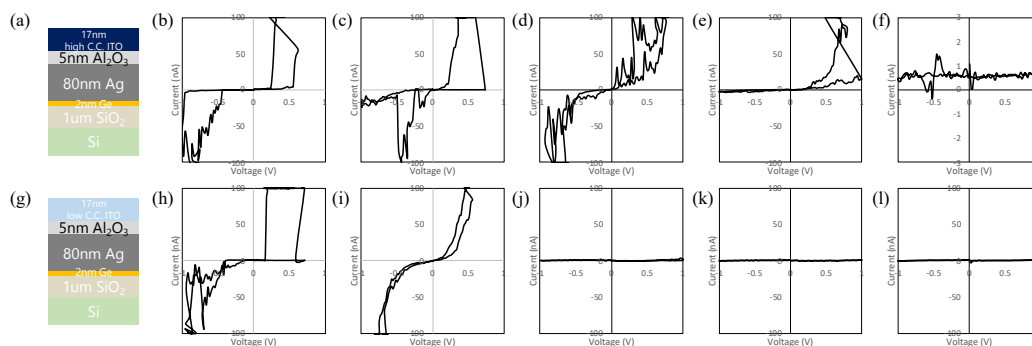


Figure 2.24 Device-to-device variation in I-V curve. (a) Schematic diagram of the device with an ITO having a high carrier concentration. (b)-(f) Five I-V curves of each device from (a). The devices were fabricated under the same deposition conditions on the same 2-inch SiO₂ on Si wafer. (g) Schematic diagram of the device with an ITO having a low carrier concentration. (h)-(l) Five I-V curves of each device from (g). The devices were fabricated under the same deposition conditions on the same 2-inch SiO₂ on Si wafer.

Since Ag is migrated or diffused into the gate dielectric layer under electrical bias, the type of gate dielectric can alter the Ag ion migration properties. Additionally, the concentration of oxygen vacancies in the gate dielectric also varies depending on the process. In the literature, oxygen vacancies in thermal atomic layer deposition (ALD) deposited HfO₂ vary from $8.20 \times 10^{10} \text{ cm}^{-2}$ (or $4.1 \times 10^{16} \text{ cm}^{-3}$) to $1.49 \times 10^{12} \text{ cm}^{-2}$ (or $1 \times 10^{17} \text{ cm}^{-3}$), as demonstrated experimentally by X-ray photoelectron spectroscopy (XPS)^{84,85}. Oxygen vacancies in thermal ALD deposited Al₂O₃ were reported to be $7 \times 10^{20} \text{ cm}^{-3}$ in⁸⁶.

Therefore, Al₂O₃, HfO₂, and an Al₂O₃/HfO₂ laminate (HAOL) were employed as gate dielectrics (Figure 2.25), and the I-V characteristics of each device were analyzed. The gate dielectric layers were deposited by atomic layer deposition (ALD) at a process temperature of 150°C without a vacuum break during the deposition process.

Al_2O_3 exhibits good thermal stability, has a large bandgap, and a high breakdown field of 10 MV/cm, acting as a diffusion barrier for Ag, leading to an increase in the threshold voltage^{80,87} However, it suffers from a relatively low dc permittivity of 9. On the other hand, HfO_2 has a wide bandgap and a relatively high dielectric constant of up to 25. But it exhibits a small breakdown field of 3.1 MV/cm and a high leakage current induced by its low crystallization temperature.

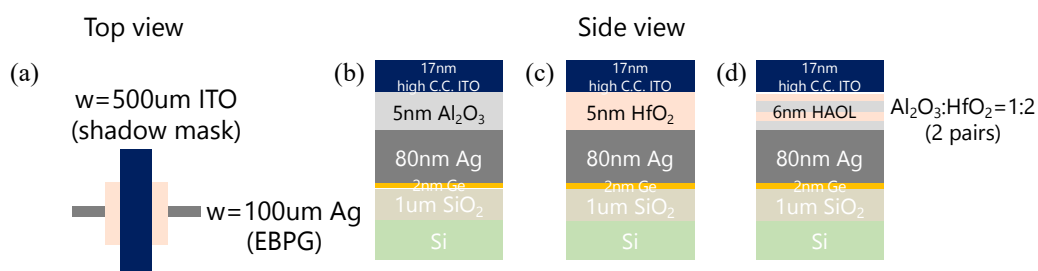


Figure 2.25 (a) Top view of the device, specifically representing the active area. (b) Ag/5nm Al_2O_3 /ITO, (c) Ag/5nm HfO_2 /ITO, (d) Ag/6nm HAOL/ITO.

Figure 2.26 shows the electrical endurance test of the Al_2O_3 device by running over 100 cycles from 0 to 1V with a compliance current of 100 nA. The device did not short over 100 cycles and continued exhibiting a hysteresis I-V loop. Figure 2.27 represents the I-V curves taken every 10 cycles. While the voltage at which an abrupt increase in current occurred remained almost the same over the entire cycles, the shape of the hysteresis loop varied. Specifically, the IV curves in Figures 2.27 (g) and (i) indicate unipolar threshold switching dominated by Joule heating. In addition, the device exhibits volatile switching behavior as the device is still in a high resistance state after the operation, indicating that the filaments are dissolved, and the low resistance state cannot be sustained when the voltage is reduced to 0. The compliance current density of $0.2\text{ mA}/\text{cm}^2$ is not enough to drive the device to behave as a nonvolatile switching device.

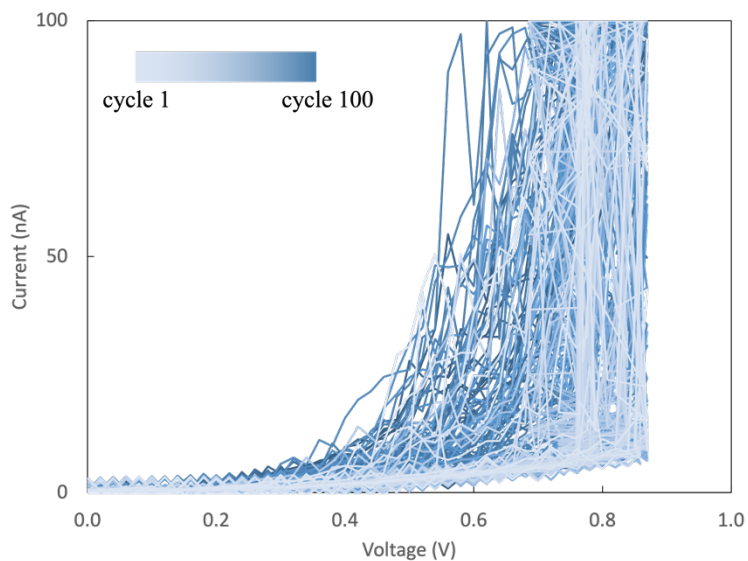


Figure 2.26 Cyclic measurements for 100 cycles to analyze the electrical endurance of the Ag/Al₂O₃/ITO device.

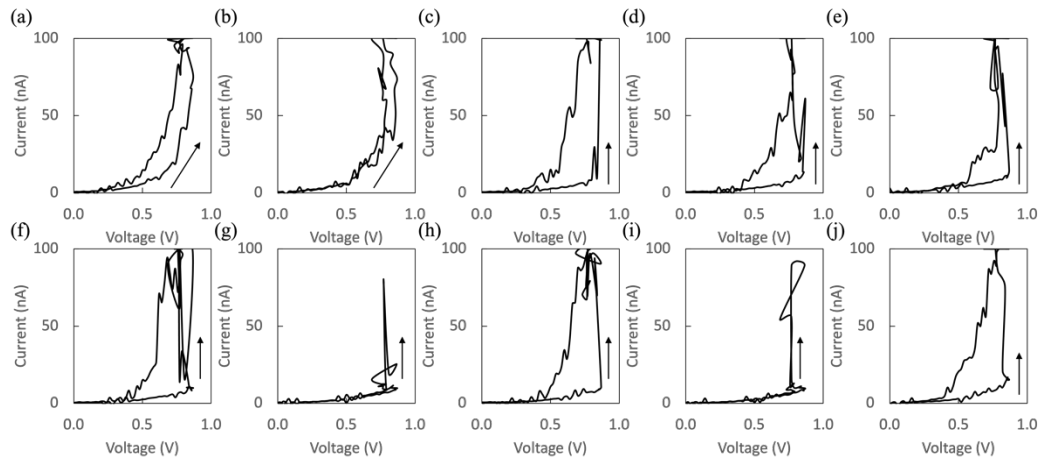


Figure 2.27 I-V curves of the Al₂O₃ device taken every 10 cycles out of 100 cycles. (a) 10th, (b) 20th, (c) 30th, (d) 40th, (e) 50th, (f) 60th, (g) 70th, (h) 80th, (i) 90th, (j) 100th.

A 10-cycle endurance test was also conducted with the HAOL device, as shown in Figure 2.28. For the first 4 cycles, there was no hysteresis loop in the I-V curves, indicating the absence of active ion migration. As the cycle progressed, the hysteresis loop became larger, actively migrating ions in the dielectric layer. The voltage at which the abrupt current jump occurred differed from cycle to cycle. The HAOL device was more unstable than the Al_2O_3 device. The direction of the hysteresis loop was always counter-clockwise, initiating from a high resistance state every time, indicating that the device exhibited volatile switching behavior.

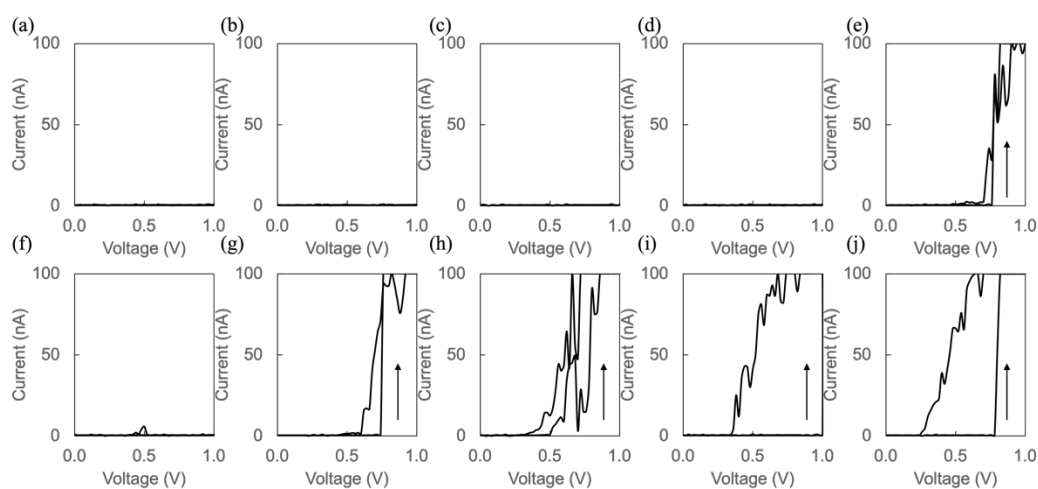


Figure 2.28 I-V curves of the HAOL device taken every cycle out of 10 cycles. (a) 1st, (b) 2nd, (c) 3rd, (d) 4th, (e) 5th, (f) 6th, (g) 7th, (h) 8th, (i) 9th, (j) 10th.

Devices with a 5nm HfO_2 layer were all shorted, possibly due to the small breakdown field. Therefore, a thicker layer of 20nm HfO_2 was deposited, and the I-V characteristics were analyzed with an active area of $5\ \mu\text{m}$ by $5\ \mu\text{m}$. The compliance current density was $40\text{A}/\text{cm}^2$.

Figure 2.29 shows the I-V curves of running 5 cycles when applying positive and negative biases, respectively. The voltage where the current jumps differed from cycle to cycle. After the third cycle, it exhibited nonvolatile unipolar switching characteristics. In Figure 2.28 (d), the loop direction is from low resistance (or high

current) to high resistance, implying that after the set in (c), a reset occurred in (d), followed by a set again in (e). The negative bias IV curve behaved differently. It seemed to set in (g) and reset in (h); however, after the 3rd cycle, the resistance state remained high. This could be because the Ag conductive filaments were completely disrupted, leaving no conductive pathway. Based on the results from Figures 2.27 to 2.29, a filament formation and disruption mechanism was proposed, as illustrated in Figures 2.29(f) and 2.29(l). This mechanism will be discussed in detail in Figure 2.34.

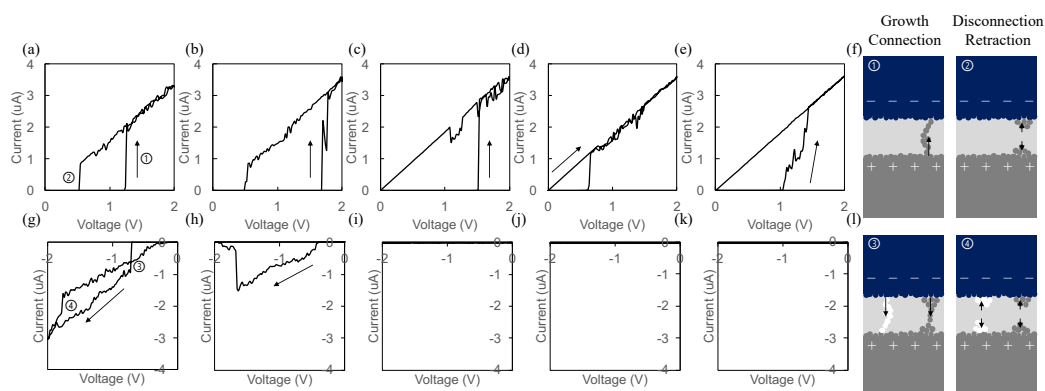


Figure 2.29 I-V curves of the 20nm HfO₂ device taken over 5 cycles, respectively. (a)-(e) Cycles 1-5 under positive bias. (f) Proposed growth-connection-disconnection-retraction mechanism when under positive bias. (g)-(k) Cycles 1-5 under negative bias application. The compliance current was set at 10 μ A. (l) Proposed growth-connection-disconnection-retraction mechanism when under negative bias. In (f) and (l), gray dots represent reduced Ag ions, and white dots represent oxygen-deficient regions.

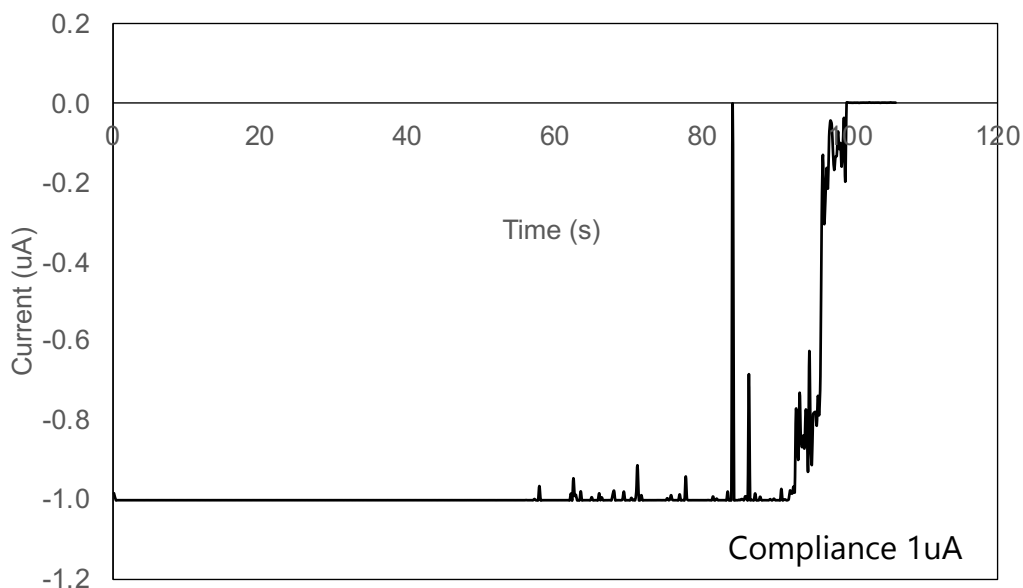


Figure 2.30 Current over time when holding at -1V in the 20nm HfO₂ device at a compliance current of 1 µA.

Figure 2.30 shows the switching kinetics, current-time characteristics under constant voltage stress at -1V for Ag/HfO₂/ITO devices. The current stays at the compliance current, meaning that conductive filaments are formed initially. Over time, while holding under negative bias, the current decreased within 2 minutes. This indicates that the conductive paths composed of Ag are disrupted, leading to a high resistance state. The switching time t_s and the voltage applied have a relationship following equation 2.5⁸⁸ :

$$t_s \propto e^{-\alpha V} \quad 2.5$$

where α is the constant value and V is the voltage applied.

The current instability over time was also observed at a very low voltage application, as shown in Figure 2.31. The electric field is not enough to form filaments, but Joule heating can drive the ion migrations or diffusions within the gate dielectric.

Therefore, a large current jump at a very low voltage implies thermally driven ion migration.

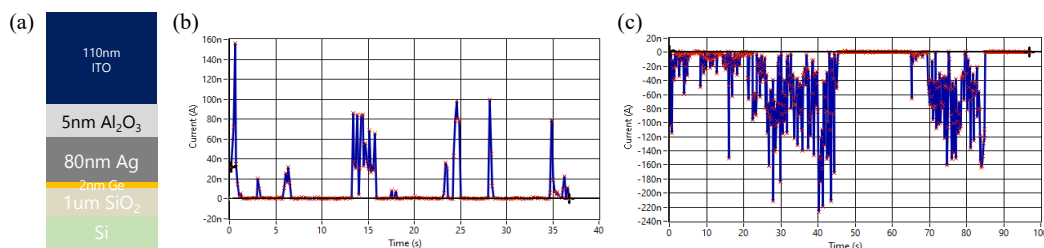


Figure 2.31 (a) Schematic diagram of a device with a thicker ITO layer and Al₂O₃ gate dielectric. (b) Current over time when holding at 1 mV bias. (c) Current over time when holding at -1 mV bias.

To investigate the effect of active area size on I-V characteristics, five devices with varying active areas, ranging from 10000 μm² to 25 μm², were fabricated on a wafer. The devices were patterned with different stripe widths through an electron-beam photolithography (EBPG) process. As the active area decreased, the absolute current flow decreased. However, the current density increased with the reduction in the active area. Additionally, the loop direction in the I-V curves is random, suggesting that both Ag and oxygen vacancies are formed and disrupted in various ways between the two electrodes. For example, Figure 2.32 (a) and (c) has volatile switching behaviors and nonvolatile switching for (b), (d), and (e).

Figure 2.33 shows the maximum current density as a function of the active area. The current density decreases as the active area increases. Notably, the current density in the smaller area (25 μm²) was 10 times higher than in the larger area (10000 μm²). If multiple filaments were uniformly formed over the active area, the maximum current density would likely remain the same regardless of the active area size. However, this observation implies that the filaments are not uniformly distributed but form as a few localized filaments within the active area.

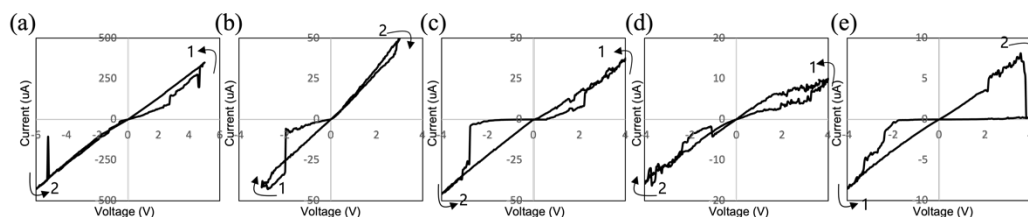


Figure 2.32 I-V curves of a device with a thin ITO layer and Al_2O_3 dielectric, depending on the size of the active area. (a) $100\ \mu\text{m}$ by $100\ \mu\text{m}$, (b) $50\ \mu\text{m}$ by $50\ \mu\text{m}$, (c) $20\ \mu\text{m}$ by $20\ \mu\text{m}$, (d) $10\ \mu\text{m}$ by $10\ \mu\text{m}$, (e) $5\ \mu\text{m}$ by $5\ \mu\text{m}$. The compliance current for (b)-(e) is $100\ \mu\text{A}$.

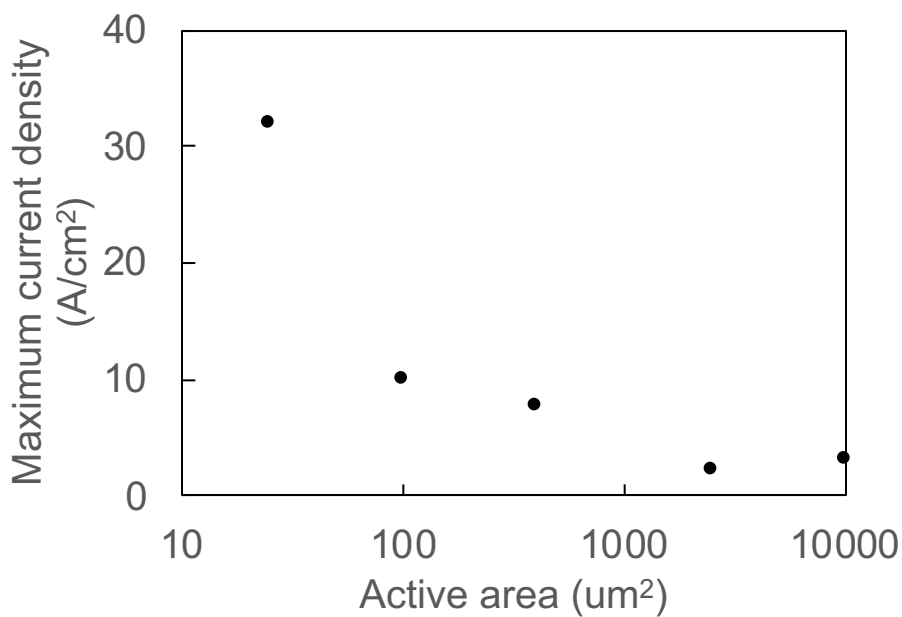


Figure 2.33 Maximum current density as a function of the active area.

In Figure 2.34, the $\text{Ag}/\text{Al}_2\text{O}_3/\text{ITO}$ device was investigated by running 4 cycles from positive bias to negative bias. The loop direction under positive bias is random, sometimes starting from a high resistance state or, in other cases, starting from a low resistance state. However, under negative bias, the loop direction always starts

from a high resistance state, and the abrupt current jump occurs at the same voltage. The device always exhibits volatile behavior under negative bias. Since the resistance state is mixed, the device can be characterized as exhibiting both volatile and nonvolatile switching.

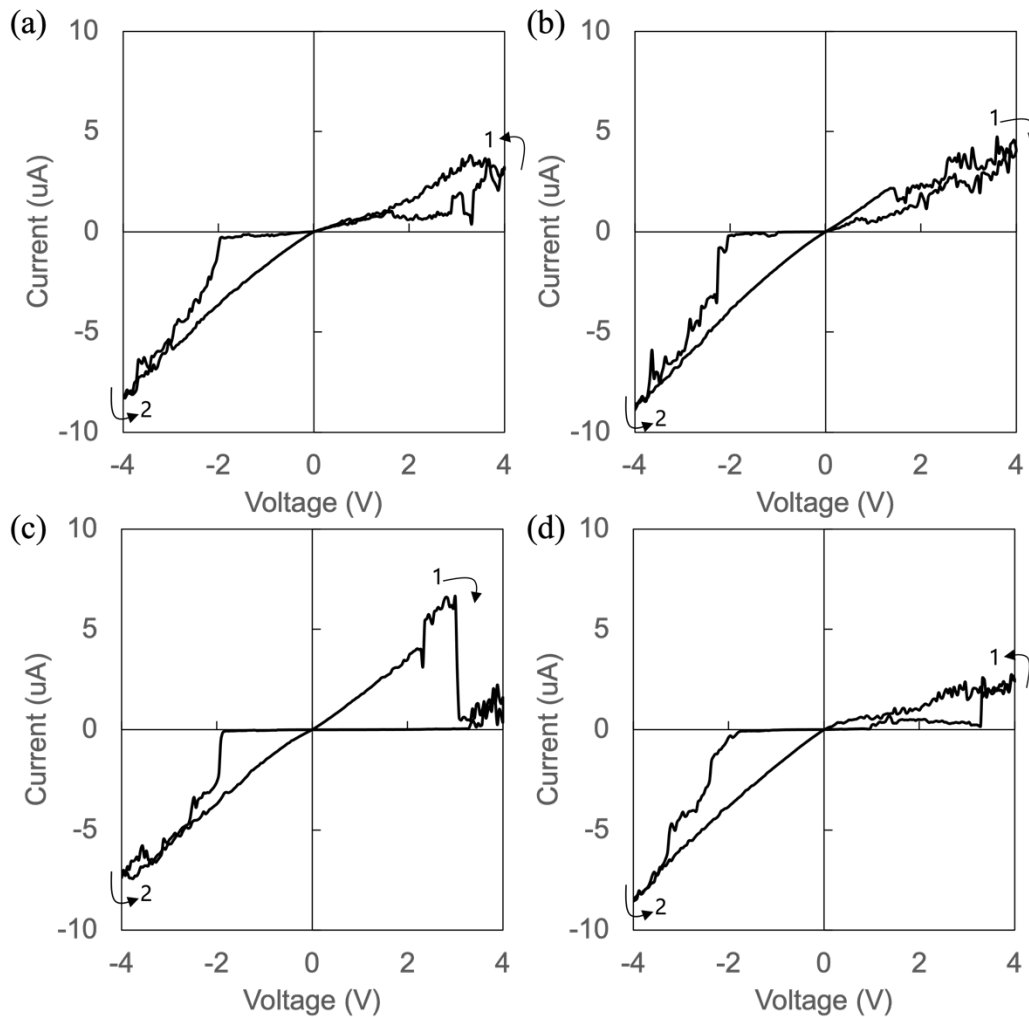


Figure 2.34 I-V curves of a device with a thin ITO layer and Al₂O₃ dielectric with an active area of 5 μm by 5 μm , taken every cycle out of 4 cycles. (a) 1st, (b) 2nd, (c) 3rd, (d) 4th cycle. (compliance current density of 100A/cm²)

Classical nucleation theory could support the unstable volatile and nonvolatile switching behavior^{20,83,89,90}. The Gibbs free energy difference (ΔG) between the state of a continuous conductive filament (CF) and the state of dispersed Ag small clusters is the change in Gibbs free energy, which can be expressed by Equation 2.6:

$$\Delta G = -\pi r^2 L |G_V| + \pi r^2 (\gamma_{ITO} + \gamma_{Ag}) + 2\pi r L \gamma_D \quad 2.6$$

Where r and L are the radius and length of the CF, $|G_V|$ is the difference in Gibbs bulk free energy per unit volume, γ_{ITO} , γ_{Ag} , and γ_D are the surface energy per unit area of the Ag conducting filament contacting with ITO, Ag, and dielectric layer, respectively. The critical size r^* can be determined by equation 2.7:

$$r^* = \frac{L \gamma_D}{L |G_V| - \gamma_{ITO} - \gamma_{Ag}} \quad 2.7$$

As shown in Figure 2.35 (a), when the filament size r is smaller than the critical size r^* , the filament tends to decompose into small Ag clusters. On the other hand, when r is greater than r^* , the filament is thermodynamically stable, and the device exhibits nonvolatile switching behavior. Based on this model, the coexistence of volatile switching and nonvolatile switching indicates that the filament size is slightly below or above the critical size r^* . By inserting literature values, r^* can be estimated to 1~3nm⁹⁰⁻⁹⁵.

Recently, the mechanisms of Ag-based volatile resistive switching memory devices were supported by the Ag ion drift and diffusion model⁹⁵, as well as an analytical model⁹³. Figure 2.35(b) shows a proposed mechanism for the Ag/dielectric/ITO-based volatile memristor. ITO acts as an oxygen vacancy reservoir, having oxygen vacancy concentrations ranging from 1×10^{19} to 1×10^{21} cm⁻³. On the other hand, the dielectric layer has a relatively low concentration of oxygen vacancies compared to the ITO. Therefore, not only Ag but also oxygen vacancies (or oxygen ions) can be mobile species due to the concentration gradient between ITO and the dielectric. As a result, when a positive voltage is applied to Ag, Ag ions start to migrate

through the dielectric and are reduced at the ITO, forming a filament. Simultaneously, due to the concentration gradient and temperature gradient from the Joule heating effect, oxygen vacancies in the ITO also migrate through the dielectric layer, forming an oxygen-deficient region. Since the filaments are thermodynamically unstable, they tend to decompose easily into small Ag clusters. Consequently, the conductive filaments spontaneously migrate from the central region of the filament to the electrodes to minimize the surface energy. By filament thinning and eventual retraction, the device returns to a high-resistant state. As the applied voltage decreases toward zero, the Ag clusters spontaneously retract to the ITO electrode and the Ag electrode to minimize the interfacial energy.

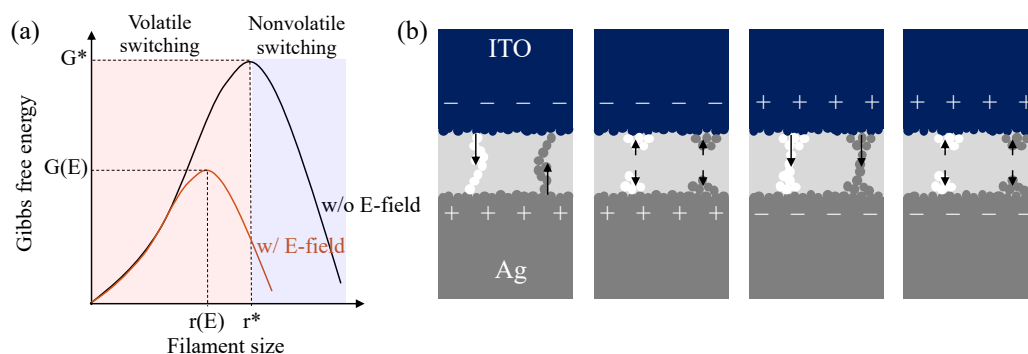


Figure 2.35 (a) Relationship between Gibbs free energy and the filament size based on the classical nucleation theory. Depending on the filament size, the device can behave both volatile switching or, nonvolatile switching. (b) proposed growth-connection-disconnection-retraction mechanism. Gray dots represent reduced Ag ions and white dots are oxygen deficient regions.

2.5 Optical response

In a planar stack of Ag/dielectric/ITO, a high reflectance over 90% is expected due to the reflective Ag layer. Figure 2.36 shows that the measured reflectance spectrum is well-matched with the calculated spectrum obtained from the transfer matrix calculation.

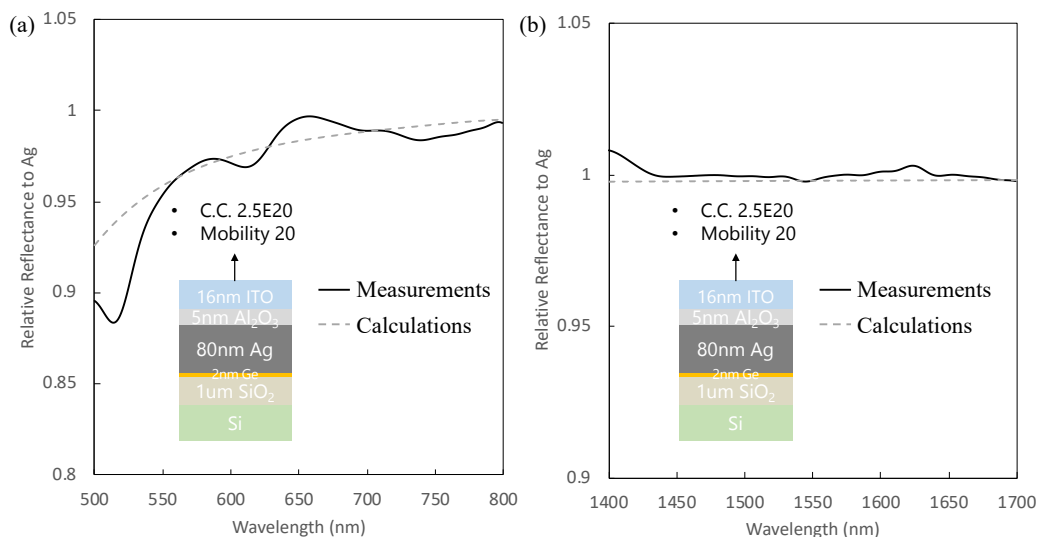


Figure 2.36 (a) Measured and calculated reflectance spectrum of the Ag/Al₂O₃/thin ITO device in the visible wavelength range. (b) Measured and calculated reflectance spectrum of the Ag/Al₂O₃/thin ITO device in the near-infrared (NIR) region.

Unfortunately, no optical modulation under electrical bias was observed in both the visible and NIR wavelength ranges. A voltage ranging from -10 mV to 10 mV was applied to confirm whether there was any dynamic optical change, as shown in Figure 2.37 (a), as well as holding at a voltage where an abrupt current jump occurred, as shown in Figure 2.37 (b). This implies that the Ag ions did not diffuse into the ITO sufficiently to tune the refractive index of the ITO by introducing Ag.

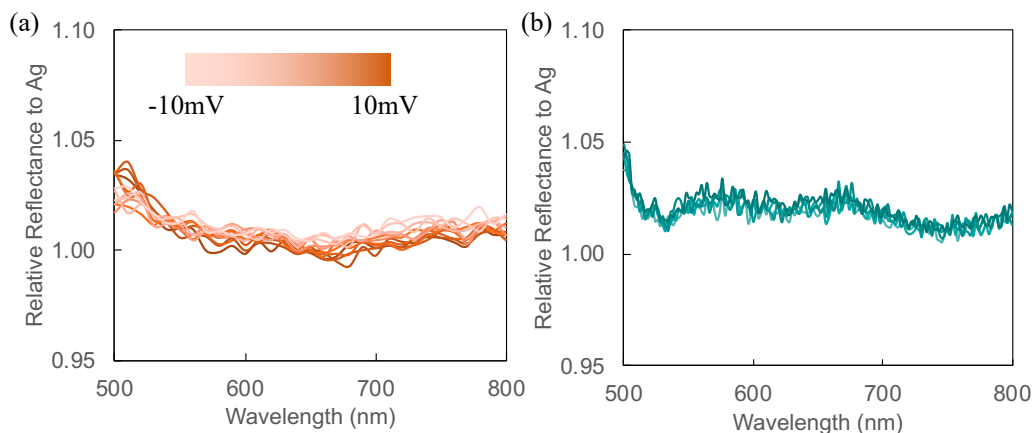


Figure 2.37 Reflectance spectrum in the visible wavelength (a) when applying an electrical bias of -10 mV to 10 mV. (b) when holding at 700 mV, where the current abruptly increased. The corresponding electrical response is represented in Figure 2.24 (c).

Therefore, an Au stripe metasurface was incorporated with the planar stack to tightly confine the light and amplify the optical modulations due to the index change in the Ag-embedded ITO layer resulting from the ion migration effect (Figure 2.38). However, no reflectance modulation occurred around the Au stripe plasmonic resonance wavelength. Ag is known to diffuse well into materials over time, so the aging effect was also studied. Regardless of aging or electrical bias, the optical response did not change. This unmodulated optical response indicates that the amount of Ag diffused into the ITO was not sufficient to form an effective medium layer, which can attribute to large refractive index change and resonance shift. This result is also supported by the classical nucleation model in Figure 2.35 and the unstable electrical responses.

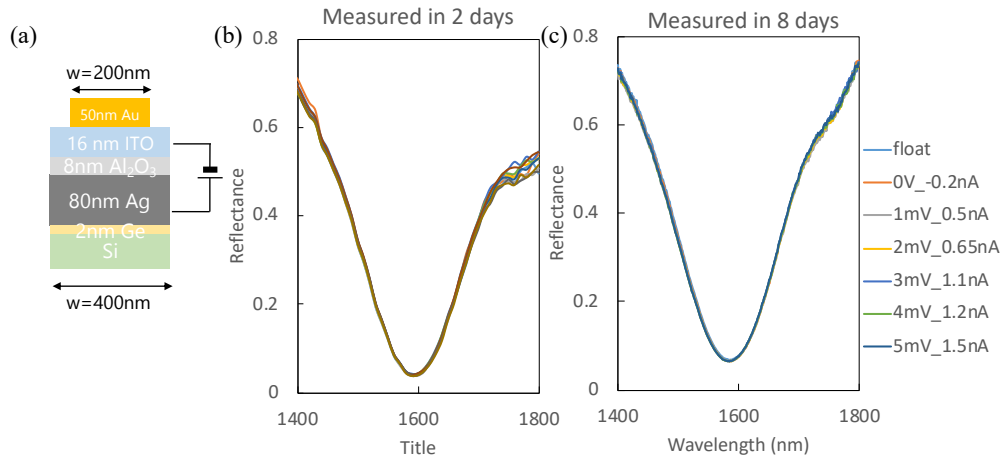


Figure 2.38 (a) Schematic diagram of Au stripe metasurfaces with Ag/Al₂O₃/ITO. Reflectance spectrum around the resonance (b) measured after 2 days (c) measured after 8 days to investigate Ag ion diffusion over time. Expected reflectance modulation was represented in Figure 2.5 calculated by Lumerical FDTD.

2.6 Conclusion and future work

Our device consisting of Ag, Al₂O₃ (or HfO₂, HAOL), and ITO is a complex system as not only Ag but also oxygen vacancies (or oxygen ions) are mobile species⁹⁶⁻¹⁰⁰. As observed in the current-voltage (I-V) curves, cycle-to-cycle and device-to-device variations are extensive. Additionally, the loop direction differs from cycle to cycle, indicating that the resistance due to the formation and disruption of filaments is random and volatile. This random ion migration prevents reliable and reproducible device performance.

Therefore, consistent and conformal formation and disruption of filaments are required to utilize the ion migration effect in optoelectronic devices with reliability and reproducibility¹⁰¹⁻¹¹⁴. In the case of a non-uniform layer, a few filaments will be formed at weak boundaries in the dielectric layer or at regions where the electric field is higher due to smaller electrode distances (Figure 2.39(a)). As shown in Figures 2.39(b) and (c), increasing the diffusion of Ag or oxygen vacancies can help enhance the refractive index change in the effective medium. If the Ag layer is patterned, the density and position of the filaments could be deliberately induced (Figure 2.39(d)). Thickening the filaments can also be another way to improve the plasmonic effect in the device (Figure 2.39(e)). Controlled formation and disruption of filaments are crucial to apply the ion migration effects into active nanophotonic devices, but further research is still required.

By controlling the formation, disruption, and geometry of metallic filaments within dielectric layers, the plasmonic properties can be actively tuned and reconfigured. In addition, the formation of metallic filaments within dielectric layers can result in highly confined plasmonic modes and strong light-matter interactions. This can potentially improve the performance of devices relying on enhanced light-matter coupling. This enables the development of dynamic plasmonic devices with adaptable optical responses. The ion migration-induced plasmonic system can open up new and exciting possibilities in the field of optoelectronic devices. The ability

to dynamically control and manipulate plasmonic structures through controlled ion migration paves the way for novel functionalities and applications.

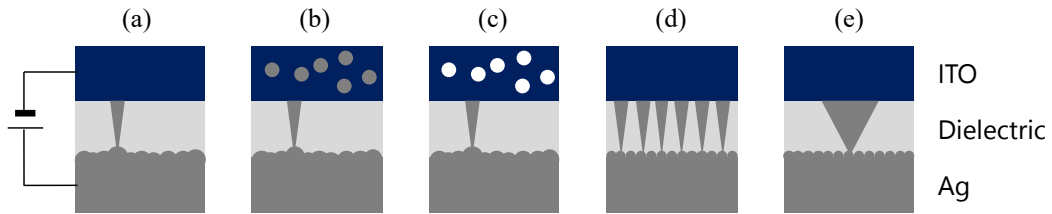


Figure 2.39 Schematic diagram illustrating ways to improve optical modulation in the Ag/dielectric/ITO device: (a) Few filament formations due to a non-uniform Ag layer. (b) Increase the diffusion of Ag into the ITO. (c) Increase the number of oxygen vacancies in the ITO. (d) Increase the density of Ag filaments. (e) Thicken the Ag filaments.

PROBING ION MIGRATION IMPACTS ON THE OPTICAL RESPONSE IN OXIDE-BASED ACTIVE METASURFACES

3.1 Introduction

Active metasurfaces offer dynamic wavefront control by electrically tuning the refractive index, but their performance can be degraded by ion migration effects in the gate dielectric. This work investigates ion migration impacts on the frequency response and phase modulation of indium tin oxide (ITO)-based active metasurfaces. Oxygen vacancy defects acting as mobile ions are identified in the atomic layer deposited gate dielectric through hysteretic current-voltage characteristics. Post-annealing processes are employed to optimize oxygen vacancy concentrations in the dielectric and ITO layers. Annealing at 150°C in vacuum effectively reduces defects while preserving ITO properties, mitigating hysteresis in electrical and optical responses. Time-resolved reflectance measurements reveal improved quasi-static resonance stabilization and enhanced high-frequency switching speeds in annealed metasurfaces compared to unannealed devices. Implementing suitable post-fabrication annealing allows defect removal, enabling high-performance active metasurfaces with rapid optical modulation across low and high frequencies for wavefront engineering, beam steering, and ultrafast applications.

Metasurfaces are two-dimensional periodic arrays of sub-wavelength scatterers that manipulate the wavefront of light. However, their optical functionality is passive and fixed at the time of fabrication. Consequently, researchers have investigated active metasurfaces that enable dynamic control of light by applying an external stimulus (electrical gating, magnetic field, chemical doping, mechanical force, thermal energy, or optical pumping) to an active material, thereby tuning its refractive index even after fabrication. Transparent conducting oxide (TCO)-based active metasurfaces have been experimentally demonstrated, where the refractive index of

the TCO at the interface between a gate dielectric and the TCO can be modulated by the field effect of electrical gating^{80,81,115–119}.

Nonetheless, during the application of an electrical bias, not only electrons or holes but also ions within the dielectric can migrate as a parasitic effect. In certain cases, electrochemical metallization through ion migration can be intentionally utilized for electrical modulation, known as memristors, or optical modulation, such as active spectral tuning of antennas. On the other hand, this ion migration effect has been observed in complementary metal-oxide-semiconductor (CMOS) devices, posing a significant challenge in maintaining reliability and performance^{120–127}. The issue becomes more severe as gate dielectrics become thinner and more defective. Oxygen anions (which are typically described by the motion of the corresponding vacancies, i.e., oxygen vacancies) are the main types of intrinsic defects. To remove defects in the dielectric, post-annealing at high temperature is proceeded with^{128–131}. The device performance relies on the quality of the gate dielectric. However, the impact of ion migration on optical responses in optoelectronic devices is not yet fully explored.

Here, we employ electrically tunable ITO-based metasurfaces. First, we demonstrate that our gate dielectric material deposited by atomic layer deposition (ALD) contains mobile ions, specifically oxygen vacancies. Next, we control the level of oxygen vacancies in the dielectric and ITO by post-annealing processes at different temperatures in ambient air or vacuum. As the optical properties of the ITO are prone to changes at high temperatures, there was a limitation in applying excessively high temperatures during annealing. We propose a mechanism for the transport of oxygen vacancies during the annealing process at the interface between the gate dielectric and the ITO. The reduced hysteresis in the current-voltage curves after the annealing process indicates diminished ionic transport during electrical gating. The time response and phase of the reflectance from the metasurfaces are measured in the quasi-static regime and the high-frequency regime (>1 MHz) before and after the

annealing process. The reduced ionic transport resulting from the removal of oxygen vacancies in the dielectric helps improve the speed of the optical response from the metasurface. This investigation paves the way for a rapid optical response at both low and high frequencies in active metasurfaces.

3.2 Electro-optic response

Active metasurfaces offer dynamic wavefront To confirm the presence of ions in our gate dielectric, we fabricated a simple capacitance device without ITO. The device comprised a 5nm-thick alumina layer deposited by atomic layer deposition (ALD) sandwiched between 50nm gold electrodes on both sides (Figure 1(a)). To fabricate Au/ Al₂O₃/Au planar heterostructures, a 2nm germanium (Ge) adhesion layer and 50 nm of gold (Au) were deposited via electron beam evaporation onto 1μm thick silicon dioxide (SiO₂) on silicon (Si) substrates. Subsequently, 5nm of aluminum oxide (Al₂O₃) was deposited by ALD, followed by another 2nm Ge adhesion layer and 50 nm of Au. The active area of the devices was 100 μm by 100 μm. Using a probe station, we applied voltages ranging from +/- 4V in 10mV steps across the device and measured the current under a compliance current setting of 100nA to prevent permanent dielectric breakdown. We tested 13 devices, and 11 out of 13 exhibited hysteresis in the current-voltage (I-V) curve, as shown in Figure 3.1(b). The hysteretic behavior in the I-V curve indicates ion migration. By applying a high electric field, an abrupt increase in current occurs due to the formation of a conductive filament. Since gold is an inert material, it does not undergo electrochemical reactions during electrical gating. Therefore, oxygen vacancies in the alumina are the only mobile species. The motion of oxygen vacancies leads to a valence change in aluminum, causing a resistance change in the alumina. It has been reported that for highly defective films with electron trap energy levels in the insulator bandgap, electron transport is governed by a trap-assisted mechanism such as Frenkel–Poole emission or hopping conduction¹²⁰.

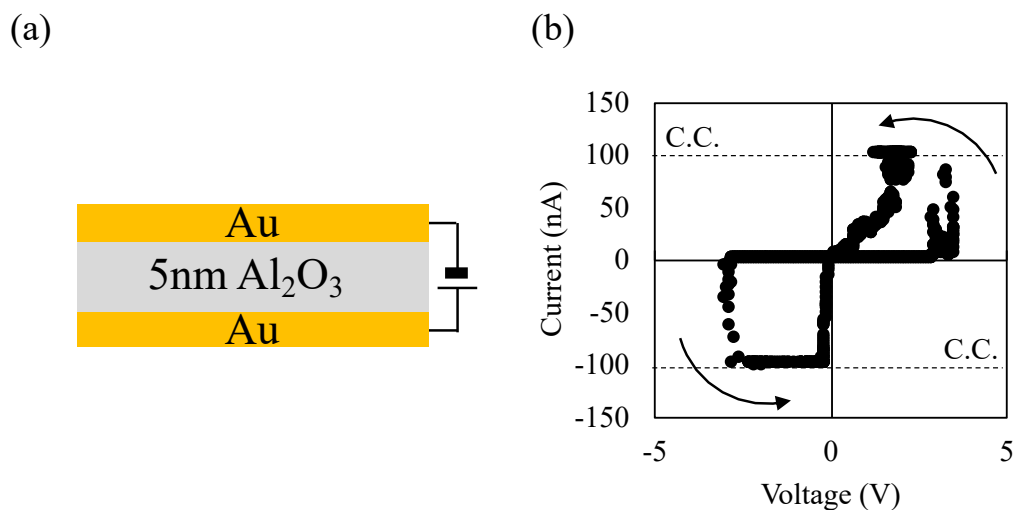


Figure 3.1 An indication of ion migration in the gate dielectric under electrical bias (a) Schematic diagram of a metal-insulator-metal (MIM) capacitor with inert gold electrodes. (b) Current-voltage curve with a compliance current (C.C.) of 100nA.

Post-annealing processes at high temperatures after gate dielectric deposition are known to improve the dielectric quality by reducing ions or defects. However, our metasurface incorporates sputtered ITO underneath the gate dielectric, and the optical and electrical properties of the ITO can be affected by the annealing process^{72,132–136}. Since changes in the carrier concentration of the ITO alter the overall metasurface resonance wavelengths, it is crucial to optimize the post-annealing conditions. Therefore, we investigated the changes in carrier concentration and mobility of the ITO when post-annealed under different conditions with or without a 5nm ALD-deposited alumina layer using Hall measurements. Samples were annealed up to 250°C in ambient air for 1-2 hours or in a vacuum on the order of 10×10^{-3} Torr in the ALD chamber for longer durations. As seen in Figure 3.2(a), the carrier concentration in the ITO decreased with increasing annealing temperature when annealed in ambient air. In contrast, when alumina was present on the ITO and annealed, there was a slight increase in the carrier concentration. This indicates that oxygen in the air fills the oxygen vacancy sites in the ITO, resulting in a decrease in the carrier concentration when annealed alone. However, the carrier concentration of the ITO

increased with increasing annealing temperature in all cases when annealed in vacuum (Figure 3.2(b)). This implies that oxygen ions in the ITO diffuse into the alumina, filling oxygen vacancies in the alumina and consequently increasing oxygen vacancies in the ITO. The less hysteretic I-V curve in Figure 3.4(b) also supports this explanation, as it signifies reduced ion migration in the dielectric. In Figure 3.2(e), the mobility is dramatically decreased in all cases, implying that the ITO starts to crystallize during high-temperature annealing. The decrease in carrier mobility is due to a change in the dominant electron carrier scattering mechanism from grain boundary scattering to ionized impurity scattering by trapping free electron carriers⁷². By increasing the annealing duration at 150°C in a vacuum chamber, both carrier concentration and mobility in the ITO increased, but not as significantly as when the ITO was covered with alumina.

Based on these results, the annealing condition was optimized to 150°C in a vacuum chamber for 24 hours, as neither the carrier concentration nor the mobility of the ITO was significantly altered, while defects in the dielectric were effectively reduced. During the annealing process, oxygen ions from the ITO diffused into the gate dielectric and filled the oxygen vacancies in the dielectric layer (Figure 3.3). This mechanism explains well the reason for the increase in the carrier concentration of the ITO after the annealing process, and it also supports the reason for the less hysteretic current-voltage (IV) curve, implying the mitigation of ion migrations within the gate dielectric after the annealing process.

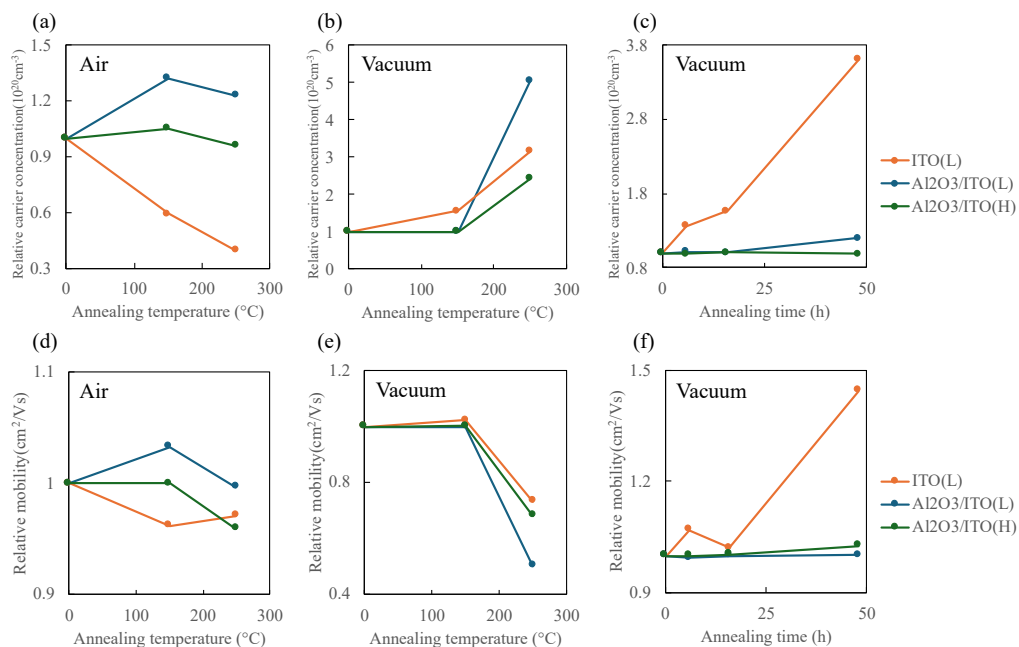


Figure 3.2 Relative carrier concentration and relative mobility of the ITO under different annealing conditions. (a)-(c) The absolute carrier concentration of ITO(L) is 0.12 cm^{-3} , $\text{Al}_2\text{O}_3/\text{ITO}(\text{L})$ is 0.21 cm^{-3} , and $\text{Al}_2\text{O}_3/\text{ITO}(\text{H})$ 1.76 cm^{-3} . Relative carrier concentration as a function of annealing temperature (a) in air for 1-2 hours (b) in vacuum for 14-16 hours. (c) Relative carrier concentration as a function of annealing time when annealed in vacuum at $150 \text{ }^\circ\text{C}$. (d)-(f) The absolute mobility of ITO(L) is $32.6 \text{ cm}^2/\text{Vs}$, $\text{Al}_2\text{O}_3/\text{ITO}(\text{L})$ is $48.7 \text{ cm}^2/\text{Vs}$, and $\text{Al}_2\text{O}_3/\text{ITO}(\text{H})$ $38.9 \text{ cm}^2/\text{Vs}$. Relative mobility as a function of annealing temperature (d) in air for 1-2 hours (e) in vacuum for 14-16 hours. (f) Relative mobility as a function of annealing time when annealed in vacuum at $150 \text{ }^\circ\text{C}$.

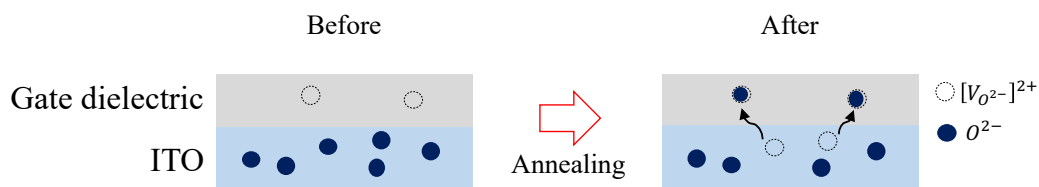


Figure 3.3 Mechanism showing the removal of oxygen vacancies in the gate dielectric during the annealing process.

Additionally, an alumina and hafnia laminate (HAOL) was chosen instead of alumina to enhance the dielectric constant and dielectric strength. The 17 nm ITO deposition was performed using an RF magnetron sputtering system with a 90/10 wt% $\text{In}_2\text{O}_3/\text{SnO}_2$ target at a pressure of 3 mTorr and a power of 100 W, while flowing 20 sccm argon (Ar) and 4 sccm Ar/O₂ mixture (90/10 wt%). The HAOL was deposited through a shadow mask via thermal ALD at 150 °C. The deposition consisted of 2 repetitions of 1nm Al_2O_3 and 3nm HfO_2 layers without breaking vacuum, accumulating a total thickness of 8 nm.

Figure 3.4(a) shows a schematic diagram of the ITO-based active metasurfaces. As observed in Figure 3.4(b), the resonance wavelength of the metasurface exhibits a red-shift when transitioning from a positive to a negative bias. The resonance wavelength of the metasurface before applying any bias is determined by the geometrical parameters, such as the width of the stripe, periodicity, and the bulk refractive index of the ITO. To confirm ion migration in the HAOL, current-voltage (I-V) curves were compared between devices without any post-annealing process and those with post-annealing at 150°C in a vacuum chamber for 24 hours. The annealing process was conducted in the ALD chamber immediately after the deposition of HAOL, without any vacuum break. The metasurface with post-annealing exhibited superior dielectric properties (Figure 3.4(c)), including a higher breakdown voltage exceeding 5V and a less hysteretic I-V curve, indicating reduced defects or fewer ions in the dielectric layer. However, hysteresis was still observed after the annealing process when applying a negative bias. This trend is also observed in p-MOS transistors operating with negative gate-to-source voltage, known as negative bias temperature instability (NBTI). In this phenomenon, positively charged holes are trapped at the interface between the dielectric and the semiconductor, and these traps can be emptied when the voltage is removed over time.

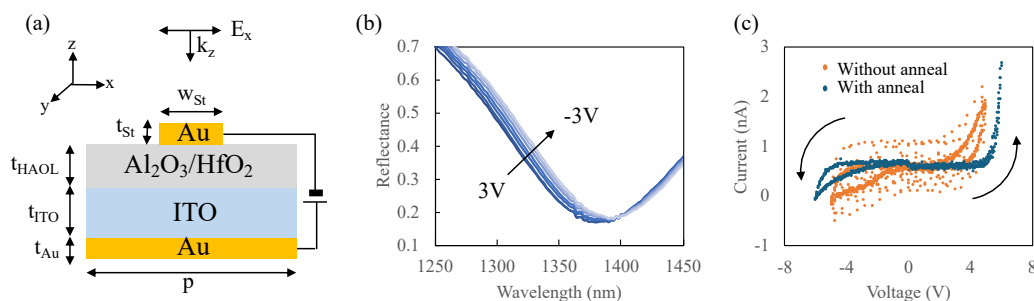


Figure 3.4 (a) Schematic diagram of ITO-based active metasurface unit cell. The structure is periodic ($p=400\text{nm}$), and the top gold stripe antenna is lengthy in the y -direction. $t_{\text{Au}}=100\text{nm}$, $t_{\text{ITO}}=17\text{nm}$, $t_{\text{HAOL}}=8\text{nm}$ (two pairs of alternating layers of 1nm alumina and 3nm hafnia), $t_{\text{St}}=40\text{nm}$, $w_{\text{St}}=220\text{nm}$. (b) Measured reflectance spectra of the metasurface by applying voltage from 3V to -3V . (c) Comparison of current-voltage (I-V) curves between the metasurface without and with post-annealing process in vacuum, with a compliance current of 100nA .

As the ionic transport effect in the dielectric was reduced after the annealing process, the phase profile also exhibited less hysteretic behavior as a function of the applied voltage, as shown in Figure 3.5(a) and (b).

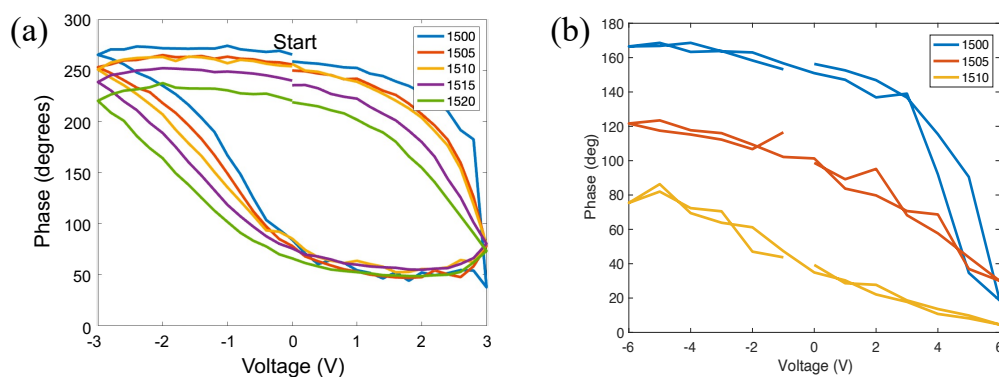


Figure 3.5 Comparison of phase profiles between the metasurface (a) without post-annealing process, or a thinner gate dielectric and (b) with post-annealing process, or a thicker gate dielectric as a function of the applied voltage.

The quasi-static amplitude response of the metasurfaces without and with post-annealing was investigated by slowly sweeping the applied voltage, as shown in Figure 3.6 (a)-(c). The reflectance was measured every 2-3 minutes in the near-infrared range around the resonance wavelength of each metasurface under applied bias. Each curve was fitted using a Lorentzian function to define the resonance wavelength. In Figure 3.6(a), without annealing, the resonance wavelength continued shifting even when the voltage was held constant (e.g., 3V or -3V). This indicates a slow metasurface response due to ionic transport in the unannealed dielectric, where trapped charges at defect sites are slowly recovered under the applied field. In contrast, the annealed device in vacuum (Figure 3.6(b)) responded faster. Comparing the slopes at 3V and -3V, the optical response was faster under positive bias, corroborating the IV curve in Figure 3.4(c) and supporting the negative bias temperature instability (NBTI) explanation. Figure 3.4(c) shows the response of the metasurface annealed in ambient air for 24 hours. The quasi-static response was not as significantly improved as when annealed in vacuum. Additionally, the resonance wavelength did not fully recover to the starting point after measurements over ~150 minutes, implying an irreversible device state due to ionic transport in the gate dielectric, behaving like a memristor device.

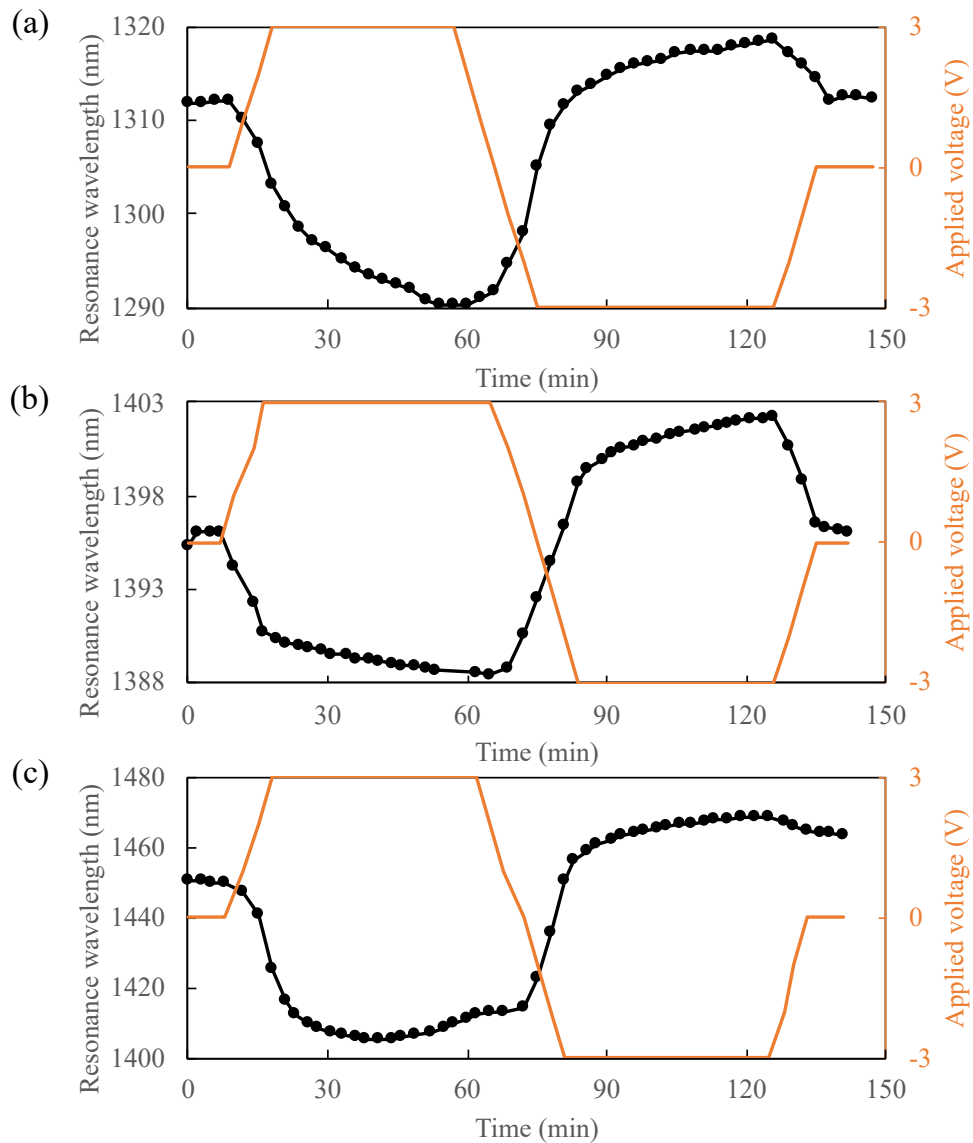


Figure 3.6. Quasi-static amplitude response at different applied voltages. Each graph shows the resonance wavelength of a metasurface while slowly sweeping the applied voltage. (a) The metasurface response without any annealing process. (b) The metasurface response with annealing at 150°C in a vacuum chamber for 24 hours. (c) The metasurface response with annealing at 150°C in ambient air for 24 hours.

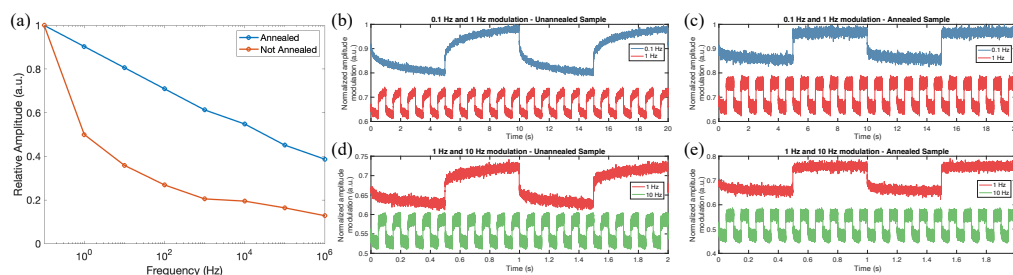


Figure 3.7 (a) Measured reflectance modulation with frequencies ranging from 0.1 Hz to 1 MHz for devices with and without a 150°C anneal in a vacuum chamber. (b) and (d) Normalized amplitude modulation of the unannealed device on (b) a longer time scale of 20 seconds, showing modulation frequencies of 0.1 Hz and 1 Hz, and (d) a shorter time scale of 2 seconds, showing modulation frequencies of 1 Hz and 10 Hz. (c) and (e) Normalized amplitude modulation of the annealed device on (c) a longer time scale of 20 seconds, showing modulation frequencies of 0.1 Hz and 1 Hz, and (e) a shorter time scale of 2 seconds, showing modulation frequencies of 1 Hz and 10 Hz.

High-frequency amplitude modulation was conducted alongside quasi-static amplitude modulation by varying the speed from 0.1 Hz to 1 MHz, as depicted in Figure 3.7(a). The figure shows the normalized modulation amplitude as a function of frequency when modulating with a 6 V peak-to-peak (VPP) square wave, normalized to the modulation amplitude at 0.1 Hz. The amplitude decreases with increasing frequency for both annealed and unannealed devices. However, the amplitude declines more gradually for the annealed device, indicating an improved device response speed. This improvement is due to the removal of mobile oxygen vacancy defects from the gate dielectric, which mitigates undesirable ion migrations within the dielectric. The actual time-domain data are shown in Figure 3.7(b)-(e). Figures 3.7(b) and 3.7(d) show the frequency response of the unannealed device at different time scales, revealing a slow increment/decrement in optical response over time. In contrast, the frequency response of the annealed device is much faster, as shown in Figures 3.7(c) and 3.7(e).

3.3 Conclusion and future work

We investigated the impact of ion migration effects on the frequency response and phase modulation of electrically tunable ITO-based active metasurfaces. The presence of mobile oxygen vacancy defects in the ALD-deposited gate dielectric was confirmed through hysteretic IV curve. The effect of post-annealing process on both the gate dielectric and the ITO was investigated through hall measurements by analyzing the oxygen vacancy concentrations. Annealing at 150 °C in a vacuum chamber helps reduce the vacancy concentration in the dielectric. With post annealing, both IV curve and the phase modulation are less hysteretic. Time-resolved reflectance measurements revealed that the annealed metasurfaces exhibited an improved quasi-static optical response, as well as high-frequency response. Overall, implementing suitable post-fabrication annealing strategies allows for the effective removal of these defects, thereby improving the modulation speed across both low and high frequencies. This work paves the way for the realization of high-performance active metasurfaces with rapid optical response times, enabling applications in dynamic wavefront engineering, beam steering, and ultrafast optical modulation.

MONOLAYER TRANSITION METAL DICHALCOGENIDES (1L-TMDS) FOR DYNAMICALLY TUNABLE METASURFACES

4.1 Introduction

Monolayer transition metal dichalcogenides (1L-TMDs) are widely recognized for their significant gate tunability of refractive indices, extending from excitonic resonances within visible wavelengths to telecom wavelengths. Despite their potential for active nanophotonic devices, exploration of their applications in the near-infrared remains incomplete. In this study, we propose two distinct high-Q dielectric metasurfaces integrated with 1L-TMDs for both amplitude and phase modulation, functioning in both transmission and reflection modes. The first tunable metasurface utilizes a Fabry-Perot resonator comprising two dielectric mirrors with 1L-TMDs strategically positioned at regions of maximum electric field intensity, achieving quality factors (Q-factors) exceeding 8900. We demonstrate the versatility of these devices as amplitude modulators or phase modulators by adjusting the number of dielectric mirror pairs. The amplitude modulation configuration achieves an 80% transmittance modulation and 97% reflectance modulation. Meanwhile, the phase modulation configuration exhibits nearly a π -phase shift in transmission and a 2π -phase shift in reflection. The second tunable metasurface features an array of silicon pillars on a silica substrate, with Q-factors exceeding 12000. With a transmission phase shift of over π , we propose this metasurface for potential applications in 2D beam steering. Overall, our findings highlight the promising capabilities of 2D TMD-based metasurfaces with low loss for advanced optical modulation and manipulation.

Metasurfaces, two-dimensional periodic arrays with subwavelength features, have garnered significant attention as thin, versatile optical components capable of manipulating light functionalities. However, the performance of these devices is

inherently limited by their fixed geometrical structures, prompting researchers to explore the integration of active materials with tunable refractive indices into passive antenna arrays. This combination allows dynamic control over optical properties through external stimuli, even after fabrication.

While metallic antenna arrays have been widely studied for their plasmonic effects in confining light within the visible to near-infrared range, metals exhibit considerable losses, hindering the achievement of the complete 2π phase shift. Dielectric metasurfaces, employing dielectric resonators, offer a compelling alternative with their high-quality factors and reduced losses.

1L-TMDs have emerged as promising 2D materials alongside graphene, exhibiting exceptional resonant properties. In the monolayer limit, TMDs possess uniquely strong light-matter interactions due to excitonic effects, with binding energies over ten times stronger than conventional semiconductors like silicon at room temperature (<26 meV)¹³⁷. Remarkably, the refractive index of 1L-TMDs can be substantially tuned near excitonic resonances through external stimuli such as strain, electrical gating, or electric/magnetic fields. This pronounced optical tunability presents opportunities for their integration as active materials in dynamic nanophotonic devices.

While active metasurfaces incorporating 1L-TMDs have been experimentally demonstrated, the tunability of the imaginary part (k) of the refractive index, corresponding to absorption, often increases significantly near excitonic resonances, introducing undesirable losses. Ideally, the real part (n) should exhibit substantial modulation while maintaining a low absolute value of k , maximizing the figure of merit expressed by $\Delta n/k$.

Owing to the Kramers-Kronig relation, k decays faster than n , suggesting the potential for exploiting 1L-TMDs beyond excitonic resonances in the near-infrared range, particularly around 1550 nm for telecommunication applications. I. Datta et al. experimentally demonstrated that the refractive index of monolayer WS_2 and

WSe₂ could be significantly modulated through electrical gating, achieving Δn up to 0.69 while maintaining Δk below 0.01 when integrated with a high-Q micro-ring resonator^{138,139}. Despite their promising potential, the exploration of 1L-TMDs in active nanophotonic devices remains largely unexplored.

In this chapter, we demonstrate the feasibility of employing 1L-TMDs in active nanophotonic devices operating in the near-infrared range for optical modulation and beam steering applications through Lumerical finite-difference time-domain (FDTD) simulations. We introduce two distinct high-Q dielectric metasurfaces designed to effectively confine the mode for 1L-TMDs: a Fabry-Perot resonator comprising dual distributed Bragg reflectors (DBR) and an array of silicon pillars on a silica substrate supporting quasi-bound states in the continuum (BICs) mode. The first tunable metasurface, embedded with 1L-TMDs, exhibits 80% transmittance modulation and 97% reflectance modulation, while the phase modulation configuration achieves nearly π phase shift in transmission and 2π phase shift in reflection. The second tunable metasurface achieves over π phase shift, demonstrating beam steering capabilities. Our findings highlight the promising potential of low-loss 2D TMD-based metasurfaces for advanced optical modulation and manipulation.

4.2 Fabry-Perot resonators embedded with 1L-TMDs

Optical simulations were performed using the finite difference time domain method (FDTD Lumerical) as well as transfer matrix calculations. In our optical simulations, a normally incident linearly polarized plane wave illuminates the metasurface from within the substrate. The real part refractive index change of 0.69 in 1L-TMD with electrical doping is taken from calculations in ¹³⁸. We assume that the imaginary part refractive index of 1L-TMD does not change with electrical doping but keeping at 0.01. The thickness of 1L-TMD is 0.618nm.

When simulating Fabry-Perot resonator, transfer matrix calculations were used. The refractive index of SiO₂ and TiO₂ are taken as 1.44, and 2.71, and we assume that the repeated pairs all have a quarter-wave thickness. The real part conductivity of graphene is taken as 60.85 μ S and -0.04 μ S of the imaginary part of conductivity.

Figure 4.1(a) illustrates our high-Q Fabry-Perot resonator, comprising dual distributed Bragg reflectors (DBRs) with n pairs of alternating silica (SiO₂) and titania (TiO₂) layers. A quarter-wave thickness of SiO₂ is employed as the gate dielectric between two electrodes, sandwiching the 1L-TMD and a monolayer graphene sheet. Strategically positioning the 1L-TMD at the region of maximum electric field intensity is crucial to effectively couple the mode with the monolayer. Due to the symmetric structure with an equal number of DBR pairs on both sides, the maximum electric field is located at the cavity's center.

As depicted in Figure 4.1(b), we investigate the effect of varying the number of DBR pairs on the amplitude modulation depth for both transmission and reflection modes to maximize the modulation capability. The Q-factor of the Fabry-Perot resonator is governed by the reflectivity of each mirror, which increases with the number of DBR pairs, leading to a higher-Q cavity. However, a higher quality factor does not necessarily translate to larger amplitude modulation, as illustrated in Figure 4.1(b). As the number of DBR pairs increases, the peak separation between the undoped ($n = 3.75$) and doped ($n = 3.06$) monolayer states widens.

Consequently, the maximum transmittance peak decreases, while the maximum reflectance peak increases, as light becomes more tightly confined within the cavity. Figures 4.1 (c) and (d) depict the transmittance and reflectance spectra, respectively, around the resonance, demonstrating the evolution of the spectra with increasing DBR pair numbers. Our analysis reveals an optimized number of 6 DBR pairs, which maximizes both transmission and reflection amplitude modulation depths, achieving over 80% in transmission modulation and 97% in reflection modulation.

An asymmetric configuration of the DBRs demonstrates superior phase modulation capabilities compared to a symmetric design. We investigated and optimized various combinations of DBR pair numbers using transfer matrix calculations to maximize phase modulation while minimizing amplitude attenuation. The optimal configuration comprises a 7-pair top DBR and an 8-pair bottom DBR, exhibiting the best performance.

Figures 4.2(a) and (b) depict the transmission and reflection spectra, respectively, along with the corresponding phase shift when the 1L-TMD is in its undoped state. By fitting the amplitude spectrum with a Lorentzian curve, the Q factor is found to exceed 8900, indicating a high-quality resonance. Remarkably, at an operating wavelength of 1555.14 nm, the device can achieve nearly a π phase shift in transmission mode, as illustrated in Figure 4.2(c), and an impressive 2π phase shift in reflection mode, shown in Figure 4.2(d).

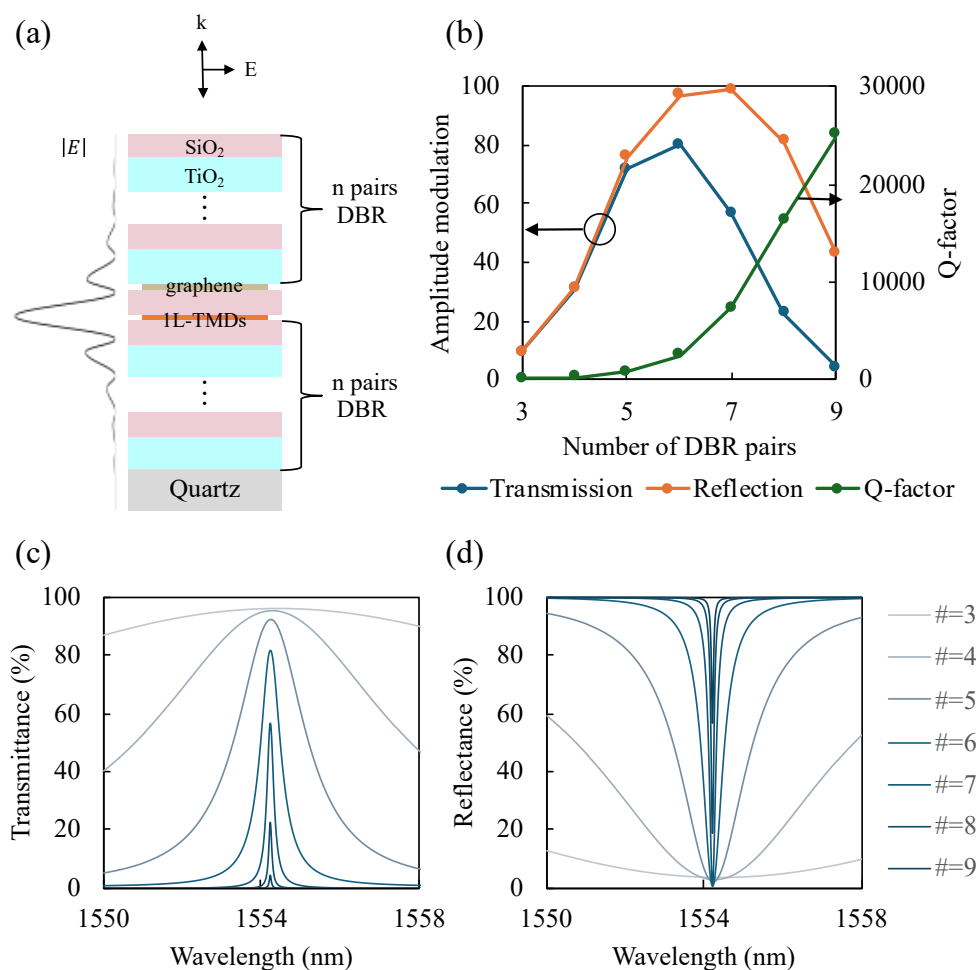


Figure 4.1 High-Q Fabry-Perot resonators embedded with van der Waals materials for amplitude modulation. (a) Schematic of dual distributed Bragg reflectors (DBRs) with an equal number of pairs. (b) Maximum achievable amplitude modulation depth in both transmission and reflection modes as a function of the number of DBR pairs in the dual DBRs. (c) Transmittance spectra and (d) reflectance spectra around the resonance, illustrating the spectral variation with increasing number of DBR pairs.

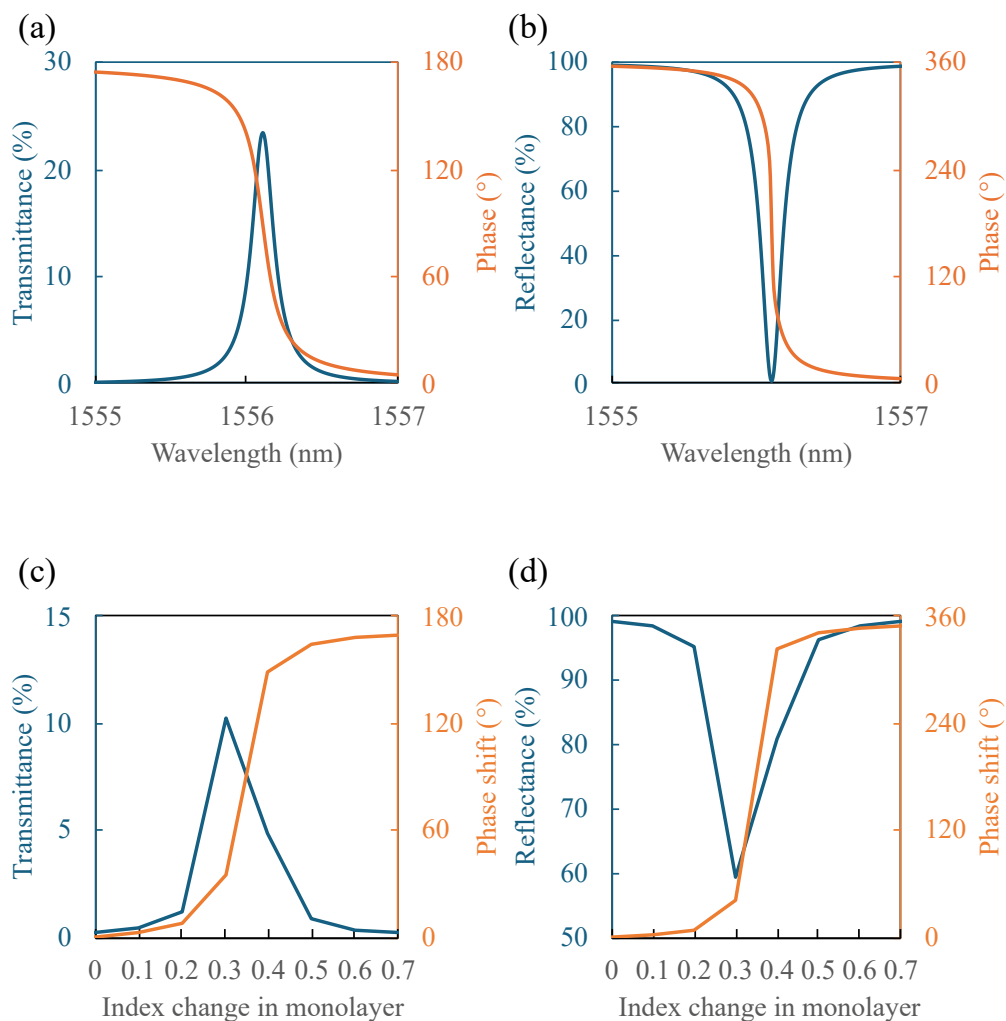


Figure 4.2 High-Q Fabry-Perot resonators for a phase modulator, comprised of a 7-pair top DBR and an 8-pair bottom DBR. (a) and (b) depict transmittance and reflectance, alongside the corresponding phase, as a function of wavelength when 1L-TMD is undoped. (c) and (d) illustrate transmittance and reflectance modulation, along with the corresponding phase shift, as a function of the index change in 1L-TMD at a wavelength of $\lambda = 1555.14$ nm.

4.3 Si-pillar resonators embedded with 1L-TMDs

In prior research, a high-quality factor (Q) metasurface supporting quasi-bound states in the continuum (BIC) mode was demonstrated through simulations for dynamic beam switching or beam steering in transmission mode by exploiting thermo-optic modulation in amorphous silicon¹⁴⁰.

In this study, the tunable metasurface features an array of silicon pillars on a silica substrate, with Q -factors exceeding 9900. Monolayer two-dimensional transition metal dichalcogenides (1L-TMDs) are situated between the pillars and the substrate, serving as active materials through electrical gating. With a transmission phase shift exceeding π , we propose this metasurface for potential applications in 2D beam steering. Overall, our findings highlight the promising capabilities of 1L-TMD-based metasurfaces with low loss for advanced optical modulation and manipulation.

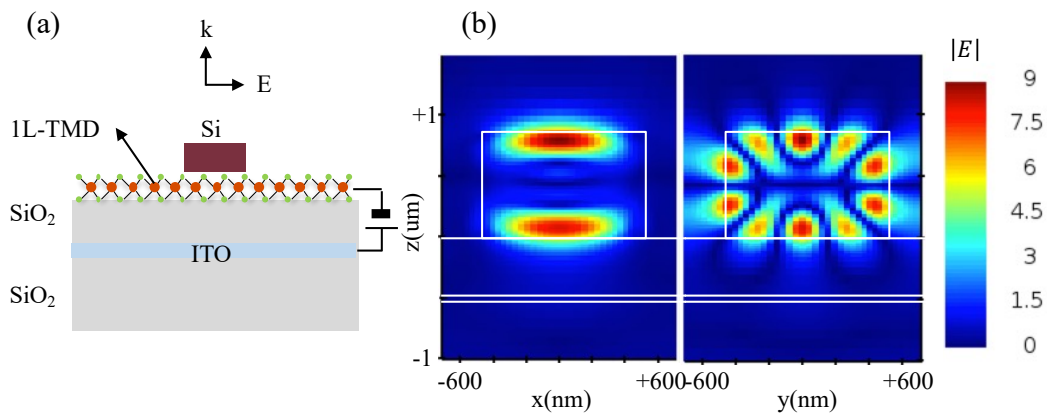


Figure 4.3 High- Q transmissive metasurfaces with van der Waals materials for a phase modulator, comprising an array of amorphous a-Si rectangular pillars on a SiO₂ substrate. (a) Schematic of a unit cell of the metasurfaces. (b) Spatial distribution of the electric field amplitude in the metasurface unit cell in x - y and y - z planes, respectively.

Figure 4.3(a) depicts an alternative geometry of dielectric metasurfaces for transmission, consisting of an array of silicon (Si) rectangular pillars on a silica (SiO₂) substrate. As indicated by the spatial mode profile in Figure 5.1(b), moderate electric field enhancement is observed above and below the pillar. To effectively couple the mode with the monolayer, the monolayer covered with a 1nm-thick hexagonal boron nitride (hBN) layer is positioned directly below the pillar structure. To enable doping of the monolayer, a gate dielectric and a counter electrode are required. We have chosen a 60nm-thick silica layer as the gate dielectric and incorporated a 5nm-thick indium tin oxide (ITO) layer underneath.

The initial geometrical parameters were adopted from ¹⁴⁰. First, to optimize the Si pillar height h , the height was varied from 850nm to 860nm at a metasurface period of $P_x = P_y = 1425$ nm. At shorter h , the lineshape exhibited a more Fano-like form, indicating asymmetrical resonance; however, it transitioned to a more symmetric quasi-Lorentzian form. (Figure 4.4 (a)) Interestingly, at the height of 860nm, the phase span suddenly dropped below 120°. Therefore, we closely examined the height between 858nm and 860nm. The corresponding transmittance and phase spectra are shown in Figure 4.4 (c) and (d), respectively. As the pillar height increased, the resonance was red-shifted. For $h > 859.2$ nm, the phase variation was limited, although the lineshape was not significantly different. The transmittance spectra were fitted to the Fano formula ¹⁴¹ in equation 4.1:

$$T = T_{bg} + A \frac{(q\gamma_0 + \omega - \omega_0)^2}{\gamma_0^2 + (\omega - \omega_0)^2} \quad 4.1$$

where T_{bg} is the constant offset, A is the resonance amplitude, ω is the frequency of light, ω_0 is the resonant frequency, γ_0 is the damping rate, and q is the Fano asymmetry parameter.

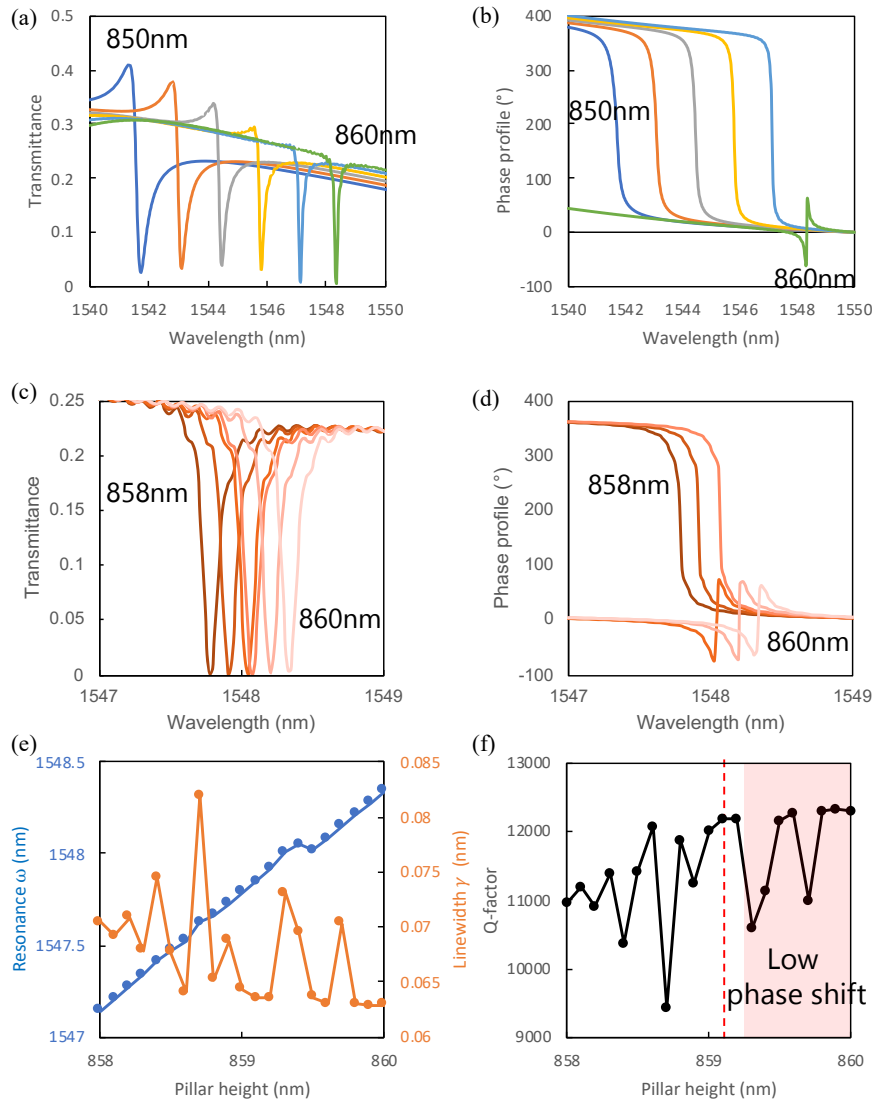


Figure 4.4 Optical response change when varying the Si pillar height (a) Transmission spectrum, and (b) corresponding phase profile when varying height from 850nm to 860nm. (c) Transmission spectrum, and (d) corresponding phase profile when varying height from 858nm to 860nm. (e) Resonance wavelength and linewidth change as a function of pillar height. (f) Q-factor as a function of Si pillar height. Red region indicates the low phase shift even though Q-factor is still high.

$$Q = \frac{\omega_0}{2\gamma_0} \quad 4.2$$

And, the Q-factor in Figure 4.4 (f) was calculated following equation 4.2. We found that the pillar height should be below 859.2 nm, where the Q-factor is high, while maintaining a high phase span for wavefront shaping applications.

Since ITO exhibits some losses in the near-infrared range, the low carrier concentration of ITO was used as it has lower extinction coefficient (k). The experimental ITO value was utilized for the simulation. (Figure 2.17 (d)) Additionally, we have avoided overlapping the ITO with the mode to prevent a reduction in the Q-factor. Based on the simulation, positioning the ITO more than 40nm away resulted in no change in the Q-factor without sacrificing a substantial phase span. Therefore, the ITO was positioned 60nm away from the Si pillar and SiO₂ interface.

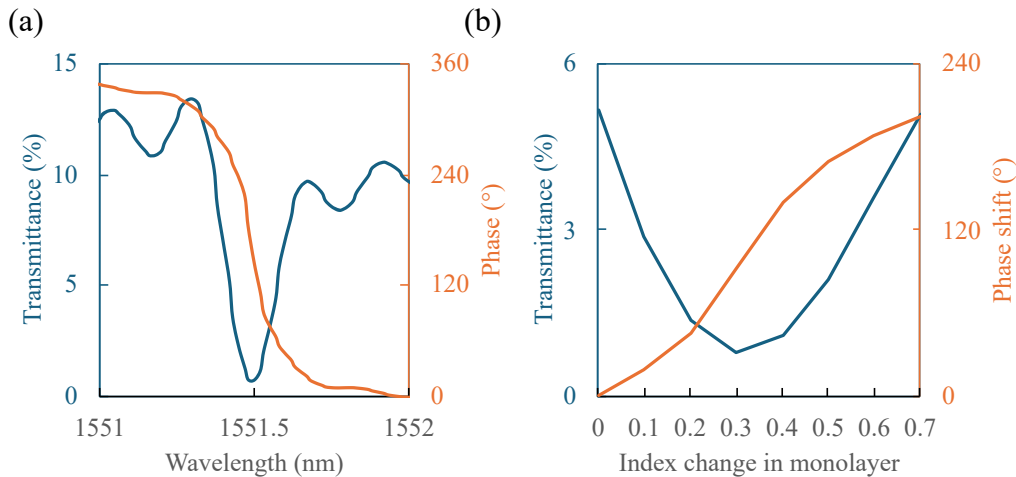


Figure 4.5 (a) Transmittance and phase as a function of wavelength when 1L-TMD is undoped. (b) Transmittance modulation, along with the corresponding phase shift, as a function of the refractive index change in 1L-TMD at a wavelength of $\lambda = 1551.42$ nm.

Figure 4.5(a) illustrates the transmission spectrum along with the phase profile. Despite assuming a certain absorption coefficient (k) of 0.01 for the monolayer, the corresponding Q-factor exceeds 9900, indicating a high-quality resonance. As shown in Figure 4.5(b), the phase gradually increases with decent transmittance as a function of the refractive index change in the monolayer, covering over a π phase shift in transmission at the wavelength of 1551.42nm.

Since our single system indicates that the phase shift is sufficient to enable beam steering, we simulate a two-level phase grating system to achieve this functionality. The beam steering is performed in a one-dimensional manner, where the phases of all metasurface elements along the y-direction are identical, while the phases of neighboring elements in the x-direction differ. The geometrical parameters are identical to those shown in Figure 4.3(a), but the refractive indices of the monolayer are distinct, with $n_1 = 3.75$ and $n_2 = 3.06$, yielding a π phase shift between neighboring elements in the x-direction (Figure 4.5(b)).

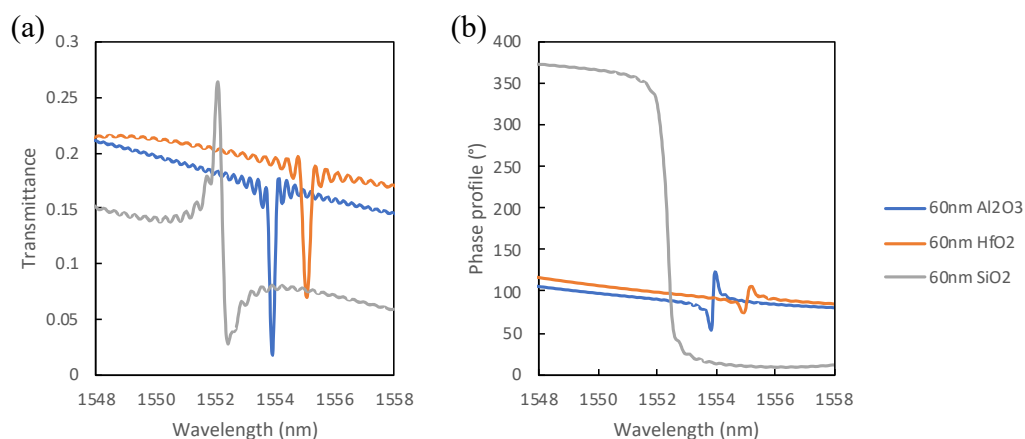


Figure 4.6 (a) Transmittance spectrum when changing the gate dielectric materials. (b) Corresponding phase profile.

In addition to SiO₂ as a gate dielectric, HfO₂ and Al₂O₃ were also analyzed to determine whether higher refractive index materials would improve the device

performance. The refractive indices of 1.41 for SiO_2 , 1.7467 for Al_2O_3 , and 1.8777 for HfO_2 were used in the calculations. Although the Q-factor was improved when using high-index gate dielectric materials, the phase span decreased, posing a drawback for beam steering applications.

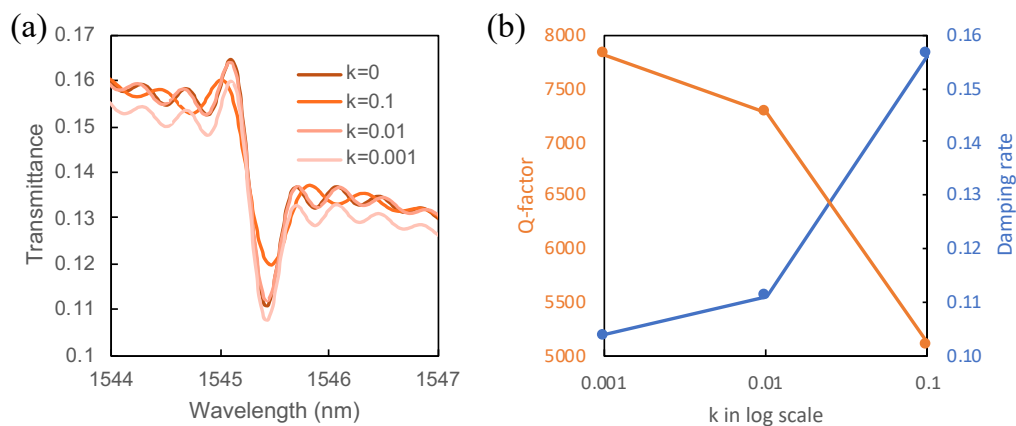


Figure 4.7 (a) Transmittance spectrum when changing the imaginary part k of the refractive index of the 1L-TMD from 0 to 0.0001. (b) Q-factor and damping rate, or the linewidth, as a function of k in 1L-TMD.

Thus far, the assumed k value of 0.01 in 1L-TMD was used in the previous simulations. However, this has not been experimentally demonstrated yet. The only reported parameter was k of 0.01 in ¹³⁸. Therefore, to confirm the device's tolerance even if the k value differs, the transmittance spectrum, Q-factor, and damping rate were examined as a function of k . (Figure 4.7) Due to the insertion of loss in the system by increasing k in the 1L-TMD, the Q-factor decreased, as expected, as the linewidth broadened. However, the phase span did not change significantly.

After the single-level optimization, the two-level system was analyzed. Figure 4.8 demonstrates the possibility of utilizing a monolayer TMD for beam steering applications. Here, by individually controlling the doping level of 1L-TMDs, different n_1 and n_2 can generate distinct wavefronts, leading to beam steering.

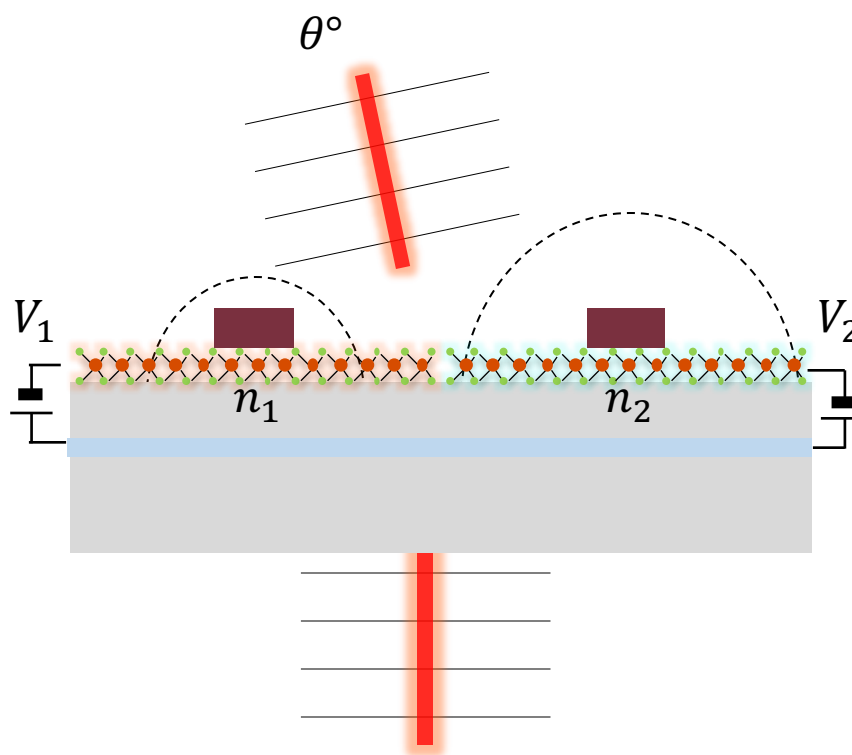


Figure 4.8. Schematic of a two-level phase grating system in High-Q transmissive metasurfaces with 1L-TMDs having two distinct refractive indices, n_1 and n_2 .

When n_1 was set to 3.75, n_2 was varied from 3.95 to 4.45 to analyze the beam steering effect. As confirmed in Figure 4.9(a), the two-level phase grating system exhibits clear beam steering, especially at angles of $\pm 33^\circ$. Upon closely examining the far-field intensity at a specific wavelength where the maximum ± 1 order beam is achieved, and at an angle of 33° , as shown in Figure 4.9(b) to (d), the intensity increased as the refractive index difference (Δn) was augmented. Specifically, $\Delta n = 0.46$ was chosen as this value corresponds to a phase difference of exactly 180° between neighboring elements; however, this did not result in a better intensity. With a three-level system, beam steering within the range of $\pm 20^\circ$ can be achieved, as shown in Figure 4.10. Although the neighboring resonators are still coupled in the near-field, resulting in an incomplete suppression of the zeroth-order beam, this

can be further improved by optimizing the geometrical parameters. Each finite-difference time-domain (FDTD) simulation takes more than 100 hours because the 0.618nm-thick monolayer, 2nm-thick hexagonal boron nitride (hBN), and 5nm-thick indium tin oxide (ITO) require small meshes to obtain reliable simulation data.

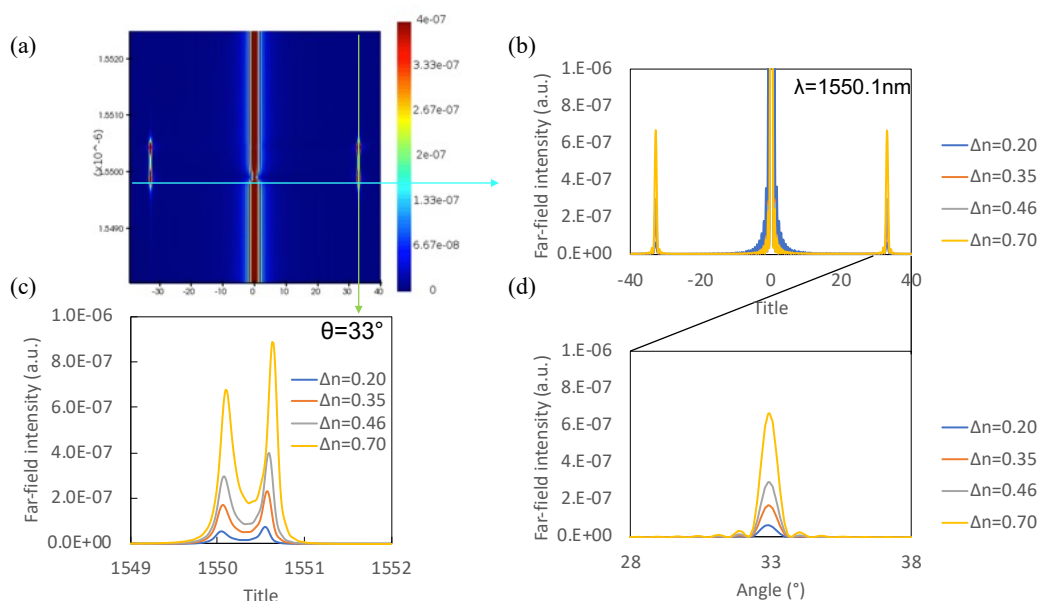


Figure 4.9 (a) 3D image of far-field intensity of the electric field for a two-level phase grating when the refractive index change between neighboring 1L-TMD is $\Delta n = 0.2$ to 0.7 in the steering angle range of -40° to 40° . (b) Far-field intensity at the wavelength of 1550.1 nm, (c) Far-field intensity at the steering angle of 33° , (d) Magnified view of (b) to closely analyze the intensity change as a function of Δn .

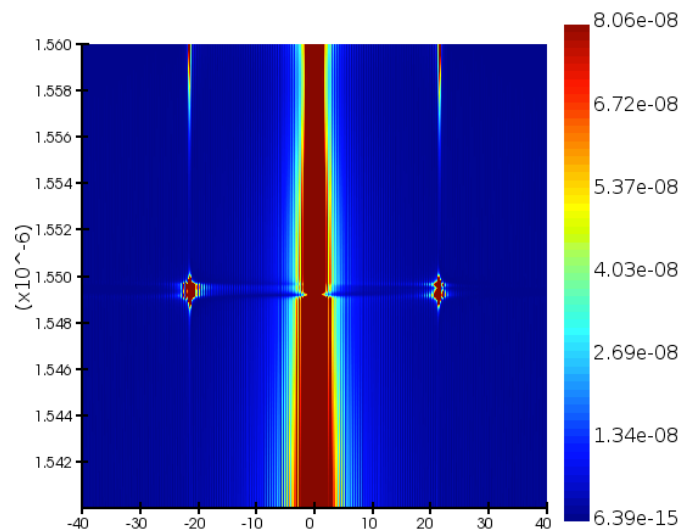


Figure 4.10 3D image of far-field intensity of the electric field for a three-level phase grating when the refractive index change between neighboring 1L-TMD is 3.795, 3.367, and 3.050, respectively, in the steering angle range of -40° to 40° .

To reduce the simulation time, a Rigorous Coupled-Wave Analysis (RCWA) solver can be employed to analyze the optical response of simulations requiring longer computation times in FDTD. The RCWA method is a semi-analytical technique for solving Maxwell's equations in multilayer structures. In this method, the structure is divided into a series of uniform layers along the direction of propagation¹⁴². However, as seen in Figure 4.11, I was unable to match the transmittance spectrum between the values from FDTD and RCWA simulations, even though different propagation vector k values were used in RCWA. If k is increased further, it also requires a very long simulation time, similar to the FDTD simulation. The monolayer with a thickness less than 1 nm is still technically challenging to solve through RCWA simulation.

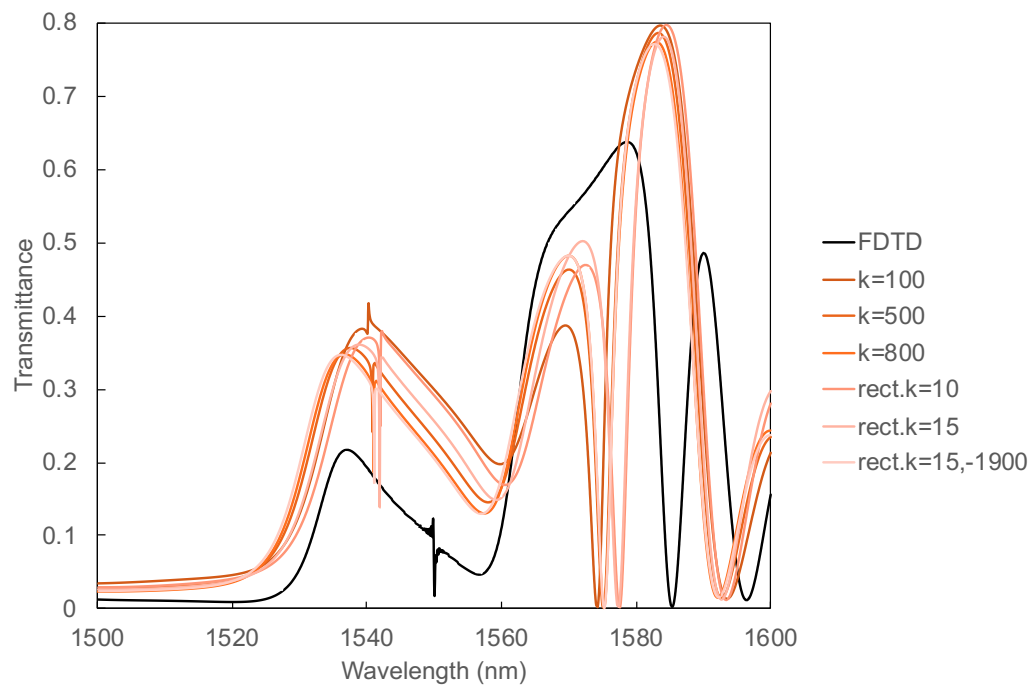


Figure 4.11 The transmittance spectrum mismatch between FDTD simulation and RCWA simulations trying different propagation vector k values in RCWA.

4.4 Conclusion and future work

In this study, we have demonstrated the promising capabilities of integrating 1L-TMD into high-Q dielectric metasurfaces for advanced optical modulation and manipulation in the near-infrared range. Through comprehensive simulations, we have introduced two distinct metasurface designs tailored for amplitude modulation, phase modulation, and beam steering applications.

The first metasurface, a Fabry-Perot resonator comprising dual DBRs with strategically positioned 1L-TMD layers, exhibited exceptional performance. By optimizing the number of DBR pairs, we achieved an impressive 80% transmittance modulation and a remarkable 97% reflectance modulation in the amplitude modulation configuration. Moreover, the phase modulation configuration, employing an asymmetric DBR design, enabled nearly a π phase shift in transmission and a full 2π phase shift in reflection at an operating wavelength of 1555.14 nm.

The second metasurface, featuring an array of silicon pillars on a silica substrate, demonstrated equally promising results. With Q-factors exceeding 9900, this design achieved a transmission phase shift of over π at 1551.42 nm, paving the way for potential beam steering applications. By simulating a two-level phase grating system, we showcased the feasibility of utilizing 1L-TMDs for one-dimensional beam steering, albeit with room for further optimization to suppress the zeroth-order beam.

Our findings highlight the remarkable potential of 1L-TMD-based metasurfaces for low-loss, dynamically tunable optical devices in the near-infrared range. The integration of these atomically thin, optically tunable materials with high-Q dielectric resonators presents a powerful platform for realizing advanced functionalities, such as optical modulators, beam steering devices, and potentially other innovative applications.

While our work focused on simulations, the successful realization of these metasurface designs could pave the way for revolutionary developments in active nanophotonic devices, offering unprecedented levels of control and versatility in optical signal processing and manipulation. Future research efforts should concentrate on optimizing the metasurface geometries, exploring alternative 2D material combinations, and investigating scalable fabrication techniques to facilitate the practical implementation of these promising technologies.

HIGH-Q FABRY-PEROT RESONATOR EMBEDDED WITH 1L-TMDS**5.1 Introduction**

Monolayer transition metal dichalcogenides (1L-TMDs) are emerging materials as their refractive indices can be dynamically tuned around excitonic resonances under external stimuli. Due to the intrinsic strong resonances in monolayers, they are attractive for active nanophotonic device applications. Here, we experimentally demonstrate how four types of 1L-TMDs interact with visible light under electrical bias at room temperature. By measuring the reflectance response of each material, we extracted the refractive index, including the resonance wavelength, oscillator strength, and linewidth, respectively, as a function of the applied bias. The results can guide the selection of appropriate materials for different electro-optic applications. Additionally, we envision the possibility of employing their electro-optic modulation in telecommunication band applications.

Two-dimensional materials have garnered attention due to their exceptional properties compared to their bulk counterparts. Notably, 1L-TMDs exhibit an indirect-to-direct bandgap transition and prominent excitonic resonances in the visible wavelength range, even at room temperature^{137,143–150}. As these materials possess strong light-matter interaction while being atomically thin, they could be powerful candidates for flat optics applications, thereby attracting significant interest. Moreover, their optical properties can be dynamically modulated under external stimuli such as electric/magnetic fields, electrical gating, chemical doping, optical pumping, or mechanical force^{151–155}. Despite important advances in exploring these reconfigurable phenomena, a comparison of electrical doping effects between various 1L-TMDs remains largely unexplored.

These materials can be deposited onto a desired surface via chemical vapor deposition (CVD), or they can be exfoliated from bulk materials. CVD-grown 1L-

TMDs are sufficiently large to employ conventional ellipsometry measurements for extracting the refractive index, but they intrinsically possess numerous defects introduced during deposition. On the other hand, exfoliated 1L-TMDs are on the millimeter scale, but they have fewer defects. In this case, their refractive index can be obtained through Kramers-Kronig consistent transfer matrix calculations^{156–161} by measuring their reflectance spectra on a substrate.

Here, we measure reflectance spectra from 550 nm to 850 nm for distinctive 1L-TMDs on 20 nm alumina and 100 nm gold on a silicon substrate. The monolayers were respectively exfoliated from bulk materials onto a pre-deposited surface. While measuring the spectra, each monolayer is electrically gated through 20 nm alumina from 0 V to 8 V to understand the gate dependence of each excitonic resonance. By fitting the gate-dependent differential reflectance measurements using transfer matrix calculations with a three Lorentz oscillators model, we extracted the refractive index, including exciton parameters such as the resonance wavelength, oscillator strength, and linewidth at each voltage. As materials are naturally doped from the bulk state, the charge neutral point can differ, leading to different trends with electrical gating. To evaluate which material is suitable for electro-optic device applications, the most important figure of merit (FOM) is a large refractive index change in the real part (Δn), while maintaining a small refractive index in the imaginary part (k), expressed as $\Delta n/k$. We evaluate the FOM of each material at the materials' resonance and at 1550 nm, the telecom band wavelength. WSe₂ is the most promising material for visible wavelength applications, and WS₂ is the best candidate for near-infrared applications. Depending on the operating wavelength of electro-optic devices and the desired optical functionality to be modulated, different materials can be selected based on the results. Our experimental demonstration of a comparison between four distinctive 1L-TMDs could guide the selection of suitable materials for various optoelectronic device applications.

5.2 Gate tunability of refractive index in various 1L-TMDs

We designed a simple capacitor structure to electrically dope four 1L-TMDs, respectively: WS₂, WSe₂, MoS₂, and MoSe₂ (Figure 5.1(a)). An optically thick 100 nm gold layer was deposited by electron-beam evaporation to serve as both a back reflector and an electrode. Subsequently, a 20 nm thick alumina layer was deposited onto the gold by atomic layer deposition (ALD). After patterning top gold electrodes, each monolayer was exfoliated from bulk crystals and transferred onto the top gold electrodes. Each monolayer's size exceeded the beam spot size for reflectance measurement, as shown in Figure 5.1(b)-(e).

To fabricate Au/ Al₂O₃/1L-TMDs planar heterostructures, a 10 nm titanium (Ti) adhesion layer and 100 nm of gold (Au) were deposited onto 1 μm thick silicon dioxide (SiO₂) on silicon (Si) substrates using electron beam evaporation. Subsequently, a 20 nm aluminum oxide (Al₂O₃) layer was deposited by atomic layer deposition (ALD), followed by exfoliation and transfer of the respective 1L-TMDs onto the Al₂O₃ surface. Monolayer MoS₂, MoSe₂, WS₂, and WSe₂ were obtained from bulk crystals (hq-graphene and 2D semiconductors) and mechanically exfoliated onto polydimethylsiloxane (PDMS) stamps using blue Nitto tape. Each monolayer was then sequentially transferred from the PDMS to a patterned Au electrode array employing an all-dry transfer technique.

The voltage was applied from 0 V to 8 V through the 20 nm alumina gate dielectric. The charge density was estimated using a parallel plate capacitor model, and the monolayer could be doped up to $2 \times 10^{13}/\text{cm}^2$ when applying 8 V, with the charge neutral point at 0 V. A voltage was applied between the back gold reflector and the top gold electrode in contact with the monolayers. The charge accumulated within a monolayer was estimated using a parallel plate capacitor model. In our devices, we employed a 20 nm thick alumina layer as the dielectric capacitor, enabling the formation of a 2D electron gas within the monolayer TMDs.

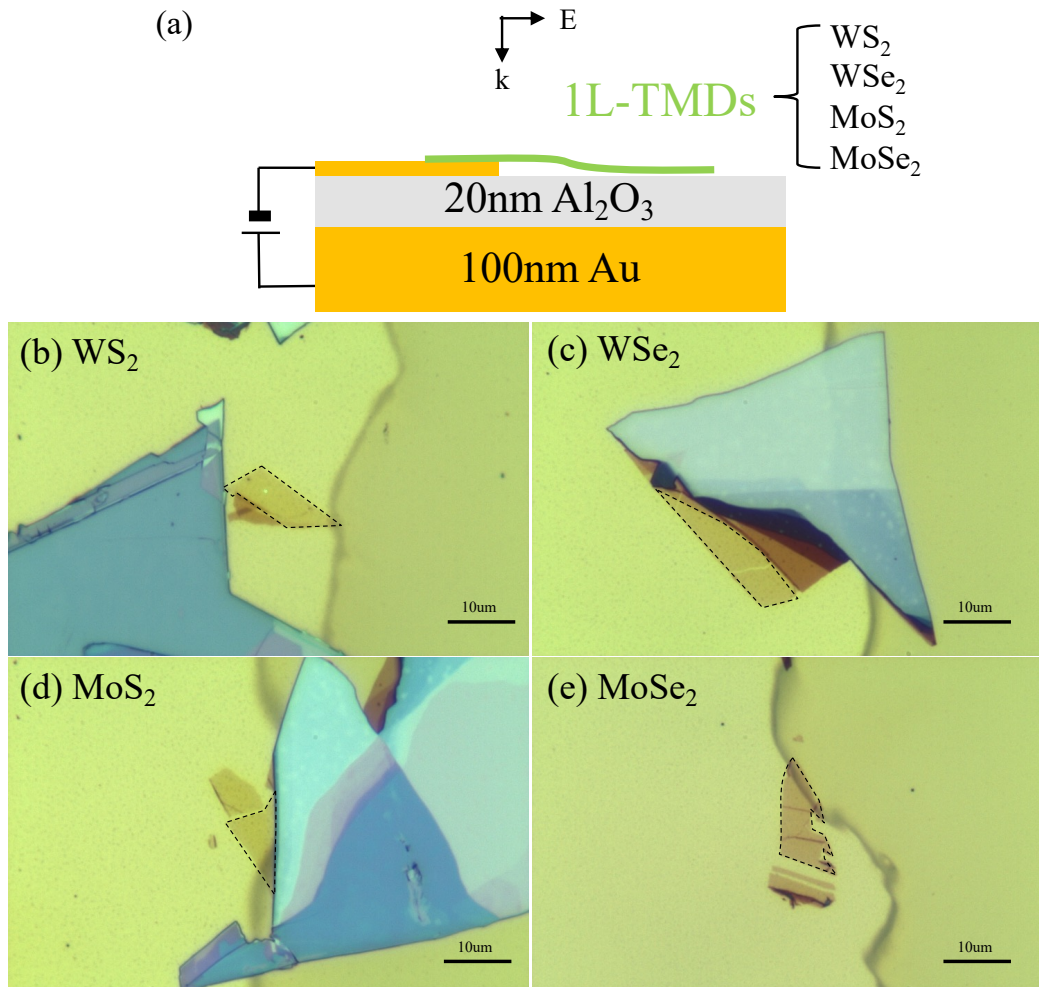


Figure 5.1 (a) Schematic diagram depicting the side view of the capacitor geometry with four 1L-TMDs. (b)-(e) Optical microscopic images of exfoliated monolayers: (b) WS₂, (c) WSe₂, (d) MoS₂, and (e) MoSe₂. The scale bar represents 10 μ m, and the dotted area indicates the presence of the monolayer for each case.

The capacitance is calculated as follows in equation 5.1:

$$C = \frac{\epsilon_0 \epsilon_R A}{d} \quad 5.1$$

where C is the capacitance, ϵ_0 is the vacuum permittivity, ϵ_R is the relative dielectric permittivity of alumina, A is the area of the capacitor, and d is the thickness of the alumina layer.

The charge density can be determined as follows in equation 5.2:

$$n[cm^{-2}] = \frac{C}{A}(V - V_{cnp}) = \frac{\epsilon_0 \epsilon_R}{d}(V - V_{cnp}) \quad 5.2$$

where n is the induced charge density, V is the applied voltage, V_{cnp} is the voltage at the charge neutral point (CNP). Therefore, n can be expressed as:

$$n = 2.485 (V - V_{cnp}) \cdot 10^{12} \quad 5.3$$

These calculations assume a relative dielectric permittivity (ϵ_R) value of 9 for alumina.

Figure 5.2 shows the reflectance spectra of the devices, including four monolayers measured at room temperature, and the extracted real and imaginary parts of the refractive index when the material is undoped and doped with an 8 V application. During the measurements, we gradually increased the voltage in 1 V steps.

We obtained the refractive index from the measured spectral reflection using Kramers-Kronig constraint analysis. We fit the reflectance spectra of our full stack with transfer matrix calculations to account for all interface effects, and model the complex refractive index of each monolayer as a sum of contributions from three Lorentz oscillators for the A exciton, B exciton, and A trion:

$$n_{TMD}^2 = \epsilon_{TMD}(\omega) = \epsilon_\infty + \sum_j \frac{f_j}{\omega_j^2 - \omega^2 - i\omega\gamma_j} \quad 5.4$$

where n_{TMD} is the complex refractive index of the 1L-TMD, ϵ_{TMD} is the complex dielectric function, ω is the frequency/wavelength, ϵ_∞ is the high-frequency

dielectric constant, f_j is the oscillator strength, ω_j is the resonant energy, and γ_j is the linewidth, or damping factor of the j -th oscillator, respectively. We use the thickness of each material with 6.18 Å for WS₂, 6.49 Å for WSe₂, 6.15 Å for MoS₂, and 6.46 Å for MoSe₂. We use the distinct value of ϵ_∞ for each material with 12.81 for WS₂, 12.93 for WSe₂, 17.9 for MoS₂, and 17.7 for MoSe₂.

We observe that modeling the refractive index of each 1L-TMD with three Lorentz oscillators yields a good fit to the data (Figure 5.2(a), (d), (g), and (j)). Comparing the spectra between 0 V and 8 V, the intensity is remarkably modulated, and the resonance wavelength is shifted around the excitonic peaks. For some mismatches at longer wavelengths, beyond the excitonic resonance wavelengths, we can discuss this later in this section, but it implies that the model is not perfect at longer wavelengths because the free carrier plasma dispersion effect becomes dominant. For the best fit even at longer wavelengths, the plasma dispersion effect should be accounted for using the Drude model. The second row (Figure 5.2(b), (e), (h), and (k)) and third row (Figure 5.2(c), (f), (i), and (l)) represent the extracted real and imaginary parts of the refractive index of each 1L-TMD, respectively. It is shown that each 1L-TMD has distinctive excitonic peaks within the visible wavelength range, and the refractive index at both the A and B excitonic energies exhibits significant gate tunability. The extracted refractive indices of each 1L-TMD reasonably match previous studies. The modulation in the refractive index n and k of each 1L-TMD at the wavelength where the maximum $\Delta n/k$ between 0V and 8V occurs is expressed in Figure 5.3.

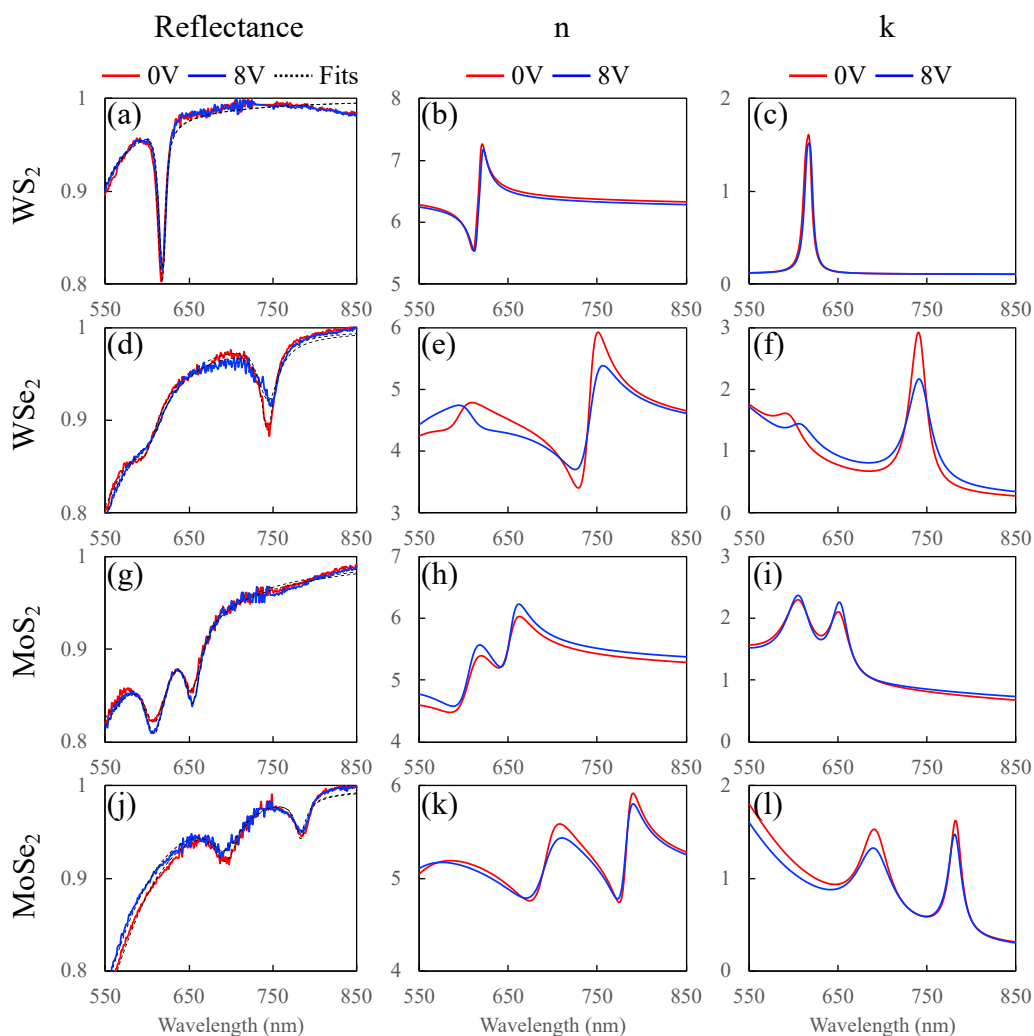


Figure 5.2 Optical response of monolayers of WS_2 , WSe_2 , MoS_2 , and MoSe_2 exfoliated on 20 nm alumina and 100 nm gold on a silicon substrate. (a), (d), (g), (j) Measured reflectance spectra. (b), (e), (h), (k) Real part of the refractive index (n). (c), (f), (i), (l) Imaginary part of the refractive index (k). The red curve represents the optical response at 0 V, and the blue curve represents the response at 8 V. The black dotted curve represents the fitted curve with three oscillator models obtained by transfer matrix calculations.

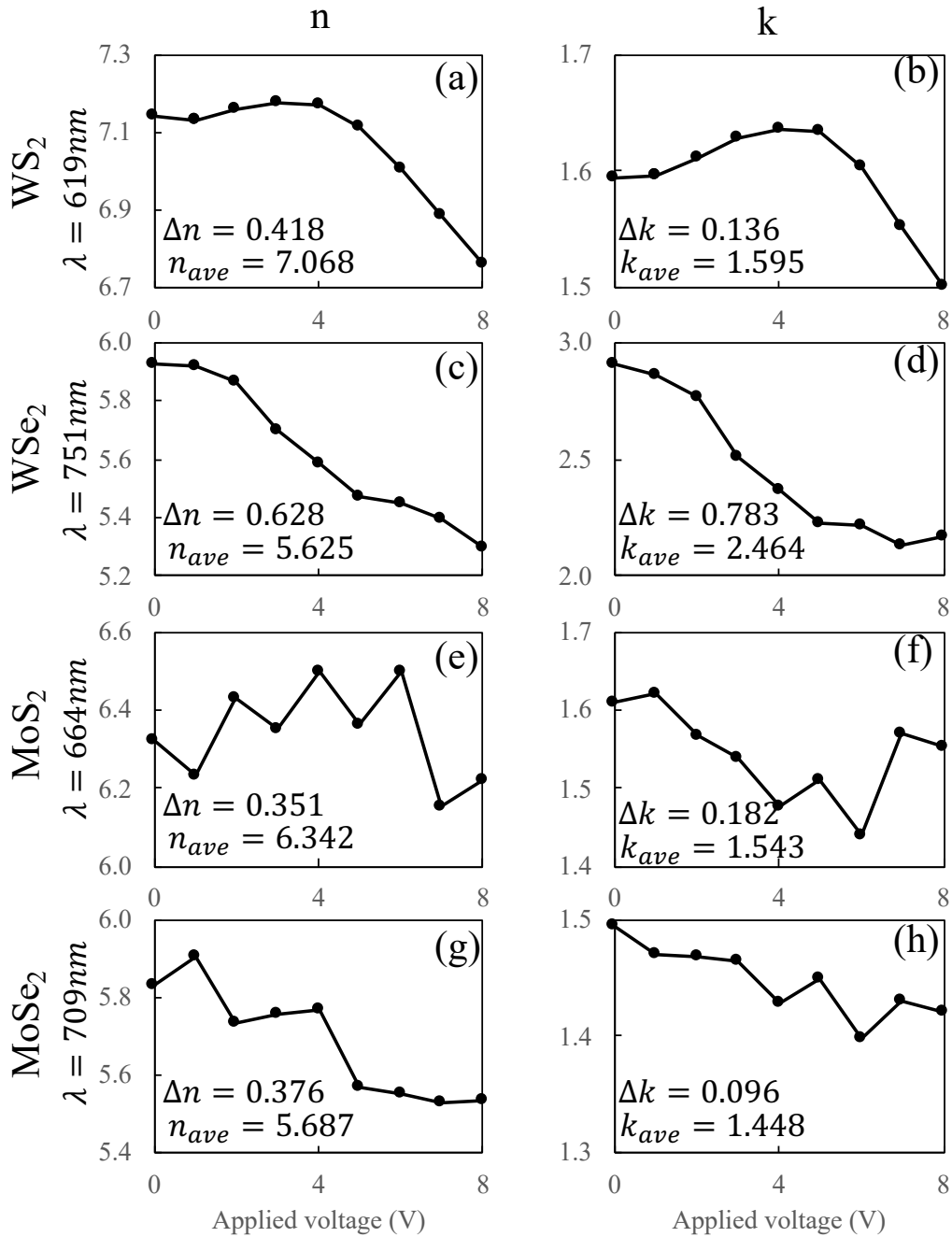


Figure 5.3 Refractive index change at the wavelength where the largest $\Delta n/k$ between 0V and 8V is observed.

To better understand the gate dependency of each 1L-TMD around the excitonic resonances, the resonant energy, linewidth, and oscillator strength are expressed as a function of the applied voltage. (In Figure 5.4) A positive bias injects electrons into the monolayer. The resonant energy is red-shifted for WS₂, WSe₂, and MoSe₂, and blue-shifted for MoS₂ when applying a positive bias. The opposite trend is attributed to the intrinsic doping in the bulk material. For WS₂, WSe₂, and MoSe₂, their charge neutral point (CNP) is below 8 V, implying that they are naturally electron-doped. However, the CNP of MoS₂ is beyond 8 V, indicating that it is naturally hole-doped. The linewidth is inversely proportional to the resonant energy. Increased scattering of the excitons by free charges increases the effective linewidth of the transition. The Coulomb screening from the excessive injected carriers reduces the binding energy of the exciton and lowers its oscillator strength.

Based on the experimental demonstration of gate tunability in optical parameters around excitonic resonances of four distinctive 1L-TMDs, useful parameters for active nanophotonic device applications in the visible wavelength range are denoted in Table 5.1. The modulation wavelength of each 1L-TMD was selected where the largest figure of merit (FOM) is observed. This wavelength is not necessarily at the resonance but is still around the excitonic resonance of each monolayer. For optical modulator application, maximizing $\Delta n/k_{ave}$ is a key metric for nanophotonic devices. In some cases, maximizing $\Delta n/\Delta k$ may be more important, depending on the application. From this perspective, WS₂ or MoSe₂ is a promising material for visible wavelength applications. For applications requiring a high refractive index (n), WS₂ or MoS₂ can be candidate materials. If the device requires high absorption, such as in a Salisbury screen, WSe₂ is the best material.

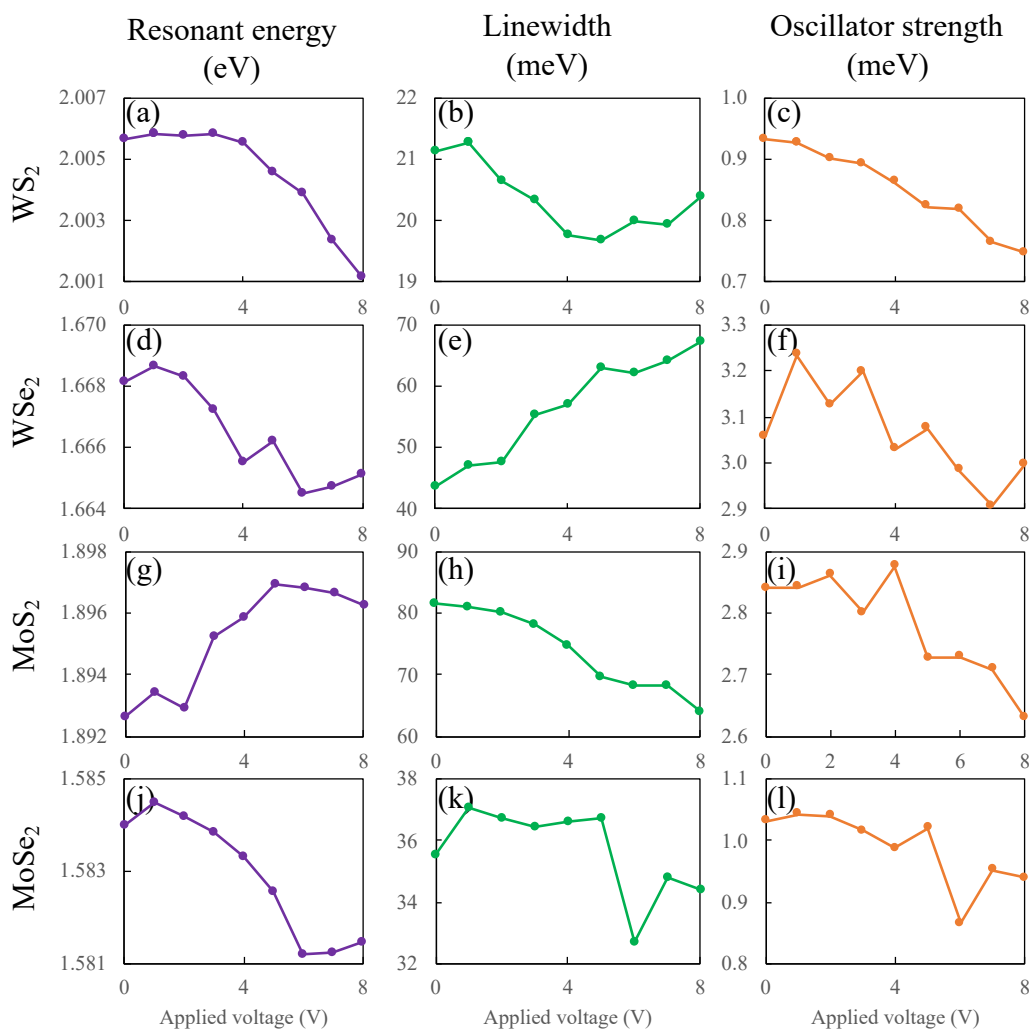


Figure 5.4 Exciton parameters of WS₂, WSe₂, MoS₂, and MoSe₂ extracted through transfer matrix calculations employing three Lorentz oscillator models. (a), (d), (g), (j) Resonant energy in eV. (b), (e), (h), (k) Linewidth in meV. (c), (f), (i), (l) Oscillator strength in meV.

In this work, we experimentally investigated the gate-tunable optical properties of four distinct 1L-TMDs — WS₂, WSe₂, MoS₂, and MoSe₂ — in the visible and near-infrared wavelength ranges. By measuring the reflectance spectra under varying

electrical bias and employing transfer matrix calculations with a three Lorentz oscillator model, we extracted the refractive index parameters, including resonance wavelength, oscillator strength, and linewidth, as a function of the applied voltage.

Our results demonstrated significant gate tunability of the refractive index around the excitonic resonances in the visible range for all four 1L-TMDs. The modulation behavior and trends were found to depend on the intrinsic doping nature of the bulk materials. We identified promising candidate materials for different optoelectronic applications by evaluating the figure of merit (FOM) based on the refractive index change (Δn) and absorption (k). Specifically, WS_2 and MoSe_2 exhibited the highest FOM for visible wavelength optical modulator applications.

Furthermore, we extrapolated the optical properties to the near-infrared regime (1550 nm) and observed a trade-off between increased refractive index due to the excitonic effect and increased absorption due to the free carrier plasma dispersion effect. WS_2 and WSe_2 emerged as suitable candidates for telecom band applications, exhibiting a higher FOM in this wavelength range.

To extend the applications to the near-infrared wavelength, the optical properties of 1L-TMDs at the wavelength of 1550 nm have been evaluated by extrapolating the physical values obtained from 550 nm to 850 nm. (Table 5.2) The wavelength is far beyond the excitonic resonance peak, and a smaller real part refractive index change is expected, at least 10 times smaller than the change around excitonic resonances. However, simultaneously, the absorption parameter, k , becomes smaller as k decays faster than n , obligating Kramers-Kronig constraints. Overall, a higher FOM in the near-infrared range could be expected. When comparing the FOM of these materials, WS_2 and WSe_2 are good candidates for telecom band applications.

It is important to note that in the Table 5.2, the values are only accounted for by the excitonic effect with electrical doping. However, in the longer wavelength range, the free carrier dispersion effect is also pronounced, so it cannot be neglected. This effect can be well described by the Drude model in equation 5.5:

$$\varepsilon_{Drude} = \varepsilon_{\infty} - \frac{\omega_p^2}{\omega^2 + i\omega\gamma} \quad 5.5$$

where ε_{∞} is the high frequency permittivity, ω_p is the plasma frequency, γ is the damping constant.

Table 5.3 Electro-Optic properties of four types of 1L-TMDs around excitonic resonances. FOM: Figure of Merit. Averaged value represents the extracted values as a function of the applied voltage between 0 V and 8 V, averaged over this range.

| <i>Optical properties of 1L-TMDs</i> | <i>WS₂</i> | <i>WSe₂</i> | <i>MoS₂</i> | <i>MoSe₂</i> |
|--------------------------------------|-----------------------|------------------------|------------------------|-------------------------|
| Modulation wavelength (nm) | 619 | 751 | 664 | 709 |
| Resonant energy (eV) | 2.00 | 1.65 | 1.87 | 1.75 |
| Averaged linewidth (meV) | 20.43 | 56.36 | 74.03 | 35.66 |
| Averaged oscillator strength (meV) | 0.86 | 3.07 | 2.78 | 0.99 |
| Averaged n | 7.07 | 5.63 | 6.34 | 5.69 |
| Δn | 0.42 | 0.63 | 0.35 | 0.38 |
| Averaged k | 1.60 | 2.46 | 1.54 | 1.45 |
| Δk | 0.14 | 0.78 | 0.18 | 0.10 |
| $\Delta n/\Delta k$ | 3.00 | 0.81 | 1.94 | 3.8 |
| <i>FOM</i> ($\Delta n/k_{ave}$) | 0.26 | 0.25 | 0.23 | 0.26 |

The plasma frequency is denoted by the following equation 5.6:

$$\omega_p^2 = \frac{Nq^2}{\epsilon_0 m^*} \quad 5.6$$

where N is the carrier density, q is the electron charge, ϵ_0 is the dielectric permittivity of vacuum, and m^* is the effective mass. An increase in the plasma frequency affects an increase in absorption. To lower the plasma frequency, a heavier effective mass and smaller electrical doping are required. Therefore, the optical properties of 1L-TMDs in the near-infrared have a trade-off between an increase in refractive index due to the excitonic effect and an increase in absorption due to the plasma dispersion effect with injected carriers. Based on the reference, the electron (hole) effective mass of WS₂ is 0.33 (0.43), WSe₂ 0.35 (0.46), MoS₂ 0.56 (0.64), and MoSe₂ 0.62 (0.72). Consequently, the heaviest MoSe₂ can minimally introduce loss in the system if all other parameters are assumed to be the same. However, the damping constant has not yet been reported for these materials, making it challenging to conclude the refractive index change due to the free carrier dispersion effect. Experimental demonstration is still required to fully understand the optical properties of 1L-TMDs in the near-infrared range.

While our analysis accounted for the excitonic effect under electrical doping, incorporating the free carrier dispersion effect through the Drude model is crucial for accurate modeling, particularly in the longer wavelength regime. Additionally, experimental investigations are still needed to fully understand the optical properties of 1L-TMDs in the near-infrared range, as the damping constant for the plasma dispersion effect remains unreported for these materials.

This comprehensive study highlights the potential of gate-tunable 1L-TMDs for active nanophotonic device applications across various wavelength ranges. The insights gained from our comparative analysis can guide the selection of appropriate materials based on the desired optical functionality and operating wavelength, paving the way for the development of reconfigurable and versatile optoelectronic devices.

Table 5.4 Electro-Optic properties of four types of 1L-TMDs at the wavelength of 1550 nm. Values are extrapolated based on the reflectance measurements from 550 nm to 850 nm.

| <i>Optical properties of 1L-TMDs</i> | <i>WS₂</i> | <i>WSe₂</i> | <i>MoS₂</i> | <i>MoSe₂</i> |
|--------------------------------------|-----------------------|------------------------|------------------------|-------------------------|
| Averaged n | 6.214 | 4.183 | 5.068 | 4.787 |
| Δn | 0.048 | 0.029 | 0.100 | 0.013 |
| Averaged k | 0.095 | 0.099 | 0.359 | 0.101 |
| Δk | 0.014 | 0.014 | 0.022 | 0.030 |
| <i>FOM</i> ($\Delta n/k_{ave}$) | 0.506 | 0.289 | 0.278 | 0.130 |

5.3 Distributed Bragg reflector (DBR)

A distributed Bragg reflector (DBR) is a dielectric mirror. Unlike metallic mirrors, which are lossy in the visible to near-infrared range, DBRs are composed of dielectric materials, rendering them lossless mirrors. A DBR consists of an alternating sequence of layers of two different optical materials. The thickness of each layer corresponds to one quarter of the wavelength of interest to achieve constructive interference. Various dielectric materials with different refractive indices can be utilized. According to equation 5.7, the reflectivity of the mirror depends on the refractive index contrast between the two materials and the number of pairs.

$$R_{DBR} = \left[\frac{n_0(n_2)^{2N} - n_s(n_1)^{2N}}{n_0(n_2)^{2N} + n_s(n_1)^{2N}} \right]^2 \quad 5.7$$

where n_0 is the refractive index of medium, n_1 is the refractive index of alternating material 1, n_2 is the refractive index of alternating material 2, n_s is the refractive index of substrate, and N is the number of repeated pair.

The oxide, nitride, and arsenide materials listed in Table 5.3 can be selected as DBR materials. Since two materials alternate as a pair, their fabrication compatibility and thermal conductivity must be considered. Figure 5.5 depicts the reflectance spectrum as a function of the refractive index contrast and the number of pairs based on transfer matrix calculations, assuming each layer's thickness is perfectly one-quarter of the target wavelength of 1550nm. Interference effects appear at specific wavelengths. When the refractive index between n_1 and n_2 is larger, and N is larger, the reflectivity of the DBR increases.

Table 5.3 Dielectric materials candidate and their real part refractive index at 1550nm.

| Materials | n at 1550nm |
|-----------|-------------|
| SiOx | 1.44 |
| AlOx | 1.75 |
| HfOx | 1.88 |
| SiNx | 1.99 |
| TaOx | 2.09 |
| ZrOx | 2.11 |
| NbOx | 2.24 |
| TiOx | 2.71 |
| AlAs | 2.91 |
| AlGaAs | 2.97 |

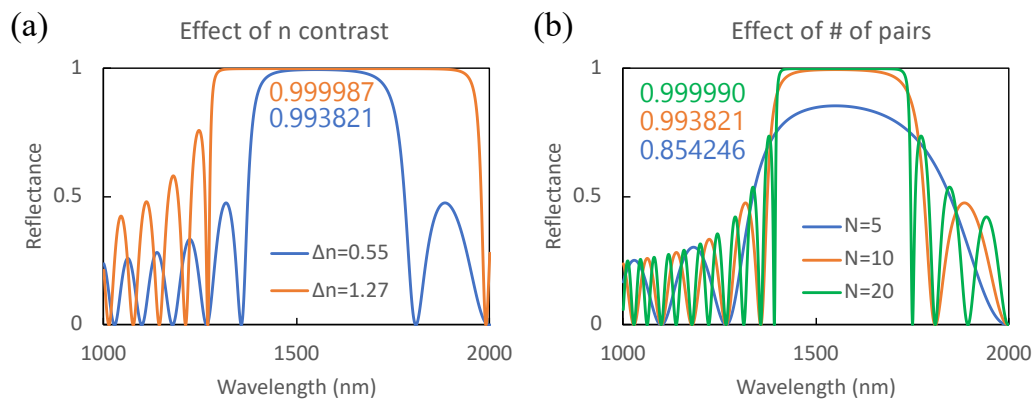


Figure 5.5 (a) Effect of the refractive index contrast on the reflectance spectrum. The blue graph assumes 10 pairs of SiOx and SiNx ($n=0.55$), and the orange graph assumes 10 pairs of SiOx and TiOx ($n=1.27$). (b) Effect of the number of pairs N on the reflectance spectrum. All cases assume SiOx and TiOx pairs.

As the DBR structure is highly sensitive to the thickness of each layer, the smoothness of each layer and precise thickness control are crucial to match theoretical limits. Chemical vapor deposition (CVD) is typically used for DBR fabrication, but electron-beam evaporation was employed due to equipment access limitations. Silicon dioxide (SiO_2) and titanium dioxide (TiO_2) were selected as the low and high refractive index layers, respectively. Based on ellipsometer measurements, the refractive index of SiO_2 was 1.4441 at 1550nm, and the refractive index of TiO_2 was 2.0567 at 1550nm. Consequently, the target thicknesses were 268nm for SiO_2 and 188nm for TiO_2 .

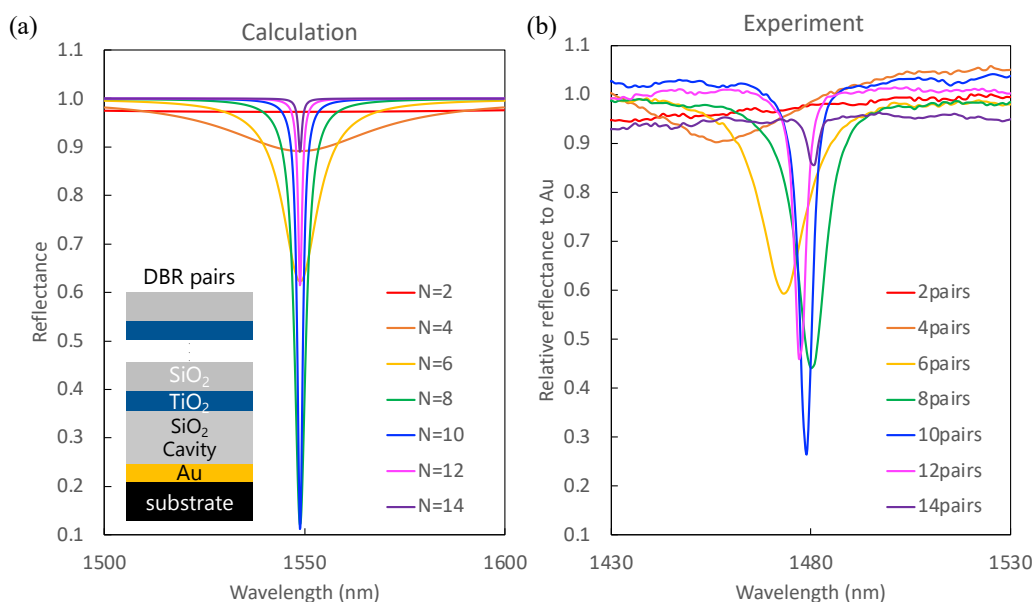


Figure 5.6 (a) Reflectance spectrum as a function of the number of top DBR pairs obtained by transfer matrix calculations. (b) Measured reflectance spectrum as a function of the number of evaporated top DBR pairs.

To analyze the optical properties of the evaporated DBRs, a Fabry-Perot resonator structure was fabricated. A 10nm-thick titanium (Ti) layer and a 170nm-thick gold (Au) layer were evaporated onto a silica-on-silicon substrate as the bottom mirror. Subsequently, a half-wavelength-thick (513nm) SiO_2 layer was deposited as the

cavity. Finally, between 2 and 14 pairs of TiO₂ and SiO₂ were evaporated onto the cavity as the top DBR. The reflectance of each resonator with a different number of pairs in the top DBR was measured, as shown in Figure 5.6(b), and the values were compared with transfer matrix calculations.

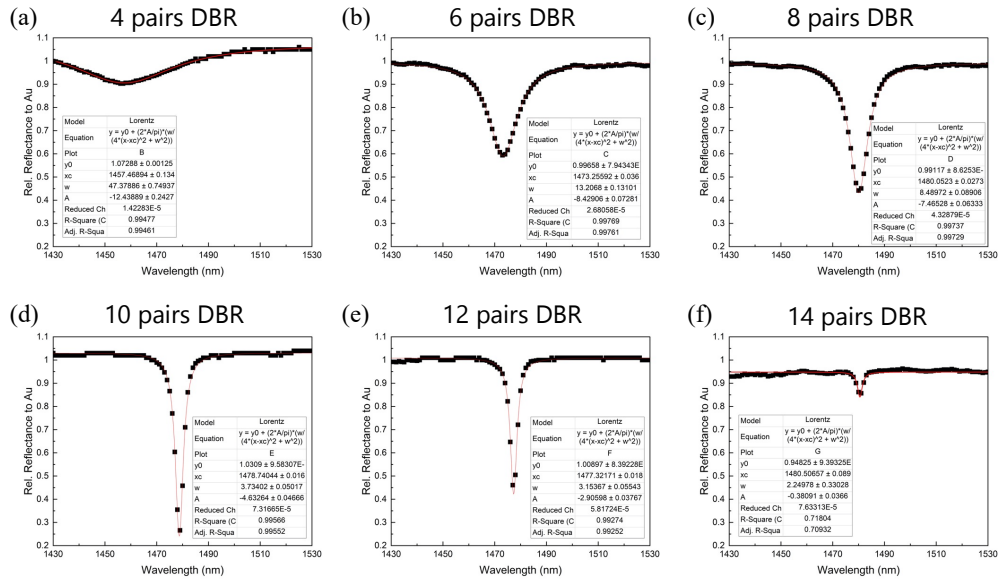


Figure 5.7 Measured reflectance spectrum fitted by a Lorentzian curve (a) 4 pairs, (b) 6 pairs, (c) 8 pairs, (d) 10 pairs, (e) 12 pairs, (f) 14 pairs.

The measured reflectance spectrum was well-fitted by a Lorentzian curve. (Figure 5.7) Through curve fitting, the resonance wavelength and linewidth were extracted. Figure 5.8 shows the theoretical and experimental full width at half maximum (FWHM) as a function of the number of DBR pairs. Theoretically, the linewidth of 1.1nm does not decrease further but saturates when more than 14 pairs are used. Experimentally, a FWHM of 2.2nm was achieved with a quality factor (Q-factor) exceeding 658, corresponding to a reflectivity greater than 99% with 14 DBR pairs.

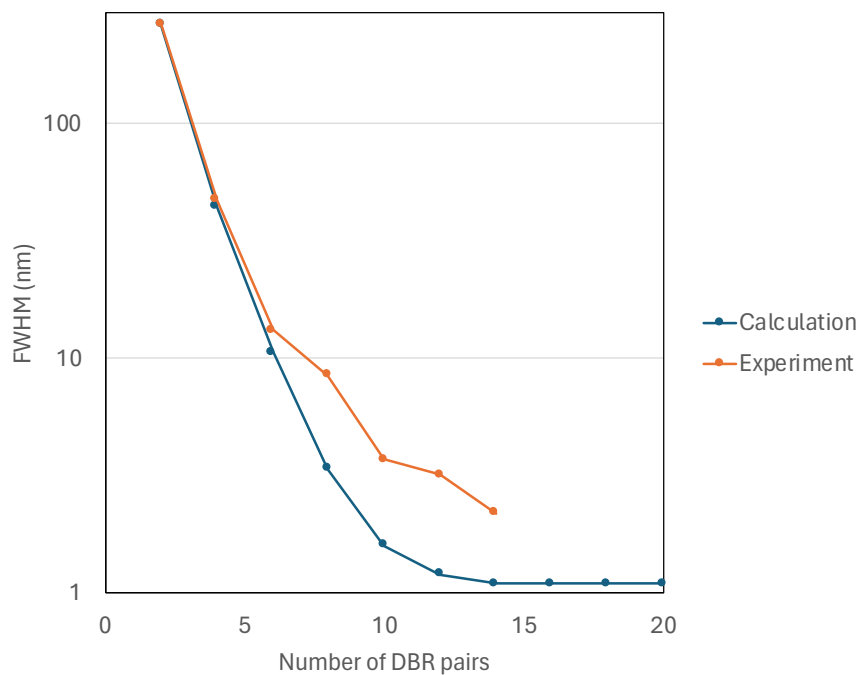


Figure 5.8 Comparison of FWHM of the resonance between calculation and experiment as a function of the number of DBR pairs.

The reflectivity of the DBR can be further enhanced by optimizing the deposition parameters. Each material was evaporated at a deposition rate of 0.5 \AA/s . During the deposition of each layer, which took approximately 90 minutes for a few hundred nanometers, the chamber temperature increased from room temperature to over 40°C due to the high-power electron beam. As the process temperature increases, the surface roughness also increases, leading to a lower quality of the deposited layer. If the e-beam deposition system contains a temperature controller in the chamber, the deposition layer quality is expected to be better.

5.4 1L-TMDs compatibility with deposition techniques

For nanophotonic device applications, it is crucial to assess their compatibility with conventional deposition techniques^{143,144,162}. However, their unique surface chemistry poses challenges^{163–168}. Atomic Layer Deposition (ALD), a widely used thin-film deposition method, enables uniform, dense deposition and precise thickness control, making it suitable for gate dielectric applications. This study investigates the impact of ALD deposition conditions, such as temperature, surface treatment, and duration, on the optical properties and surface morphologies of 1L-WS₂ by employing photoluminescence (PL) measurements and atomic force microscopy (AFM). Additionally, the variability in optical and surface characteristics among different monolayers is explored. Finally, alternative deposition techniques to ALD are proposed for these materials.

The integration of 1L-TMDs into practical device architectures requires careful consideration of their compatibility with conventional deposition techniques. There are several vacuum deposition techniques, categorized as physical vapor deposition (PVD) and chemical vapor deposition (CVD). The most common PVD processes are sputtering and evaporation, which involve vaporization of target materials and subsequent condensation to form thin films on a substrate. On the other hand, one widely employed CVD technique is Atomic Layer Deposition (ALD), which has gained popularity due to its ability to produce uniform, conformal coatings with precise thickness control at the nanometer scale. ALD is particularly attractive for the deposition of high-quality gate dielectrics in electronic devices, as it enables the formation of densely packed and pinhole-free films with excellent step coverage, even on high-aspect-ratio structures. However, the process involves chemical reactions at the interface of gaseous reactants and the solid surface of a substrate, and surface properties affect the overall thin film quality. As 1L-TMDs lack dangling bonds on their surface, combined with their atomic-scale thickness, this poses significant challenges in achieving high-quality interfaces and preserving their intrinsic properties during device fabrication processes.

In the context of 1L-TMDs, the ALD process holds promise for the integration of these materials into advanced device architectures. However, the impact of ALD deposition conditions, such as temperature, surface treatment, and deposition duration, on the optical properties and surface morphology of 1L-TMDs remains to be thoroughly investigated. Understanding these effects is crucial for optimizing device performance and ensuring the preservation of the desired material characteristics.

This study focuses on examining the influence of ALD deposition conditions on the optical and surface properties of 1L-WS₂, a representative member of the 1L-TMD family. By employing photoluminescence (PL) measurements and atomic force microscopy (AFM), the changes in the optical response and surface morphology of 1L-WS₂ are systematically explored under various ALD process parameters, including deposition temperature and surface pretreatment. Additionally, the variability in optical and surface characteristics among different 1L-TMDs, such as WS₂, WSe₂, MoS₂, and MoSe₂, is explored. Furthermore, the study investigates alternative deposition techniques, such as electron-beam evaporation and exfoliated dielectrics, to ALD for the integration of 1L-TMDs into device architectures. Each deposition method has its own advantages and limitations in terms of film quality, conformality, and compatibility with the delicate surface chemistry of 1L-TMDs. This study could provide valuable insights into the integration of 1L-TMDs into nanophotonic and optoelectronic device architectures and contribute to the development of strategies for preserving the exceptional optical properties of these materials while enabling their successful incorporation into practical device platforms.

Monolayer MoS₂, MoSe₂, WS₂, and WSe₂ were obtained from bulk crystals (h-graphene and 2D semiconductors) and mechanically exfoliated onto polydimethylsiloxane (PDMS) stamps using blue Nitto tape. Each monolayer was then sequentially transferred from the PDMS to a patterned Au electrode array employing an all-dry transfer technique.

We employed mechanically exfoliated 1L-TMDs instead of CVD-grown ones as they are more pristine with fewer defects. The exfoliated 1L-TMDs were transferred onto a 1 μ m-thick silica-on-silicon substrate. After measuring PL, the samples were placed in the ALD chamber for alumina deposition. We targeted a 20nm-thick alumina film with two or three-step processes. Higher temperatures above 300°C can damage 1L-TMDs, so the ALD process temperature did not exceed 270°C. To gently increment the process temperature and avoid damaging 1L-TMDs, different process steps were conducted: Process 1: 10nm alumina deposited at 150°C, followed by 10nm at 200°C. Process 2: 10nm alumina deposited at 150°C, followed by 10nm at 270°C. Process 3: 10nm alumina deposited at 200°C, followed by 10nm at 270°C. Process 4: 7nm alumina deposited at 150°C, followed by 7nm at 200°C, and 6nm at 270°C. After deposition, the PL of 1L-TMDs was tested again, and the surface morphologies were analyzed by AFM.

Figure 5.9 (a)-(d) shows a smooth surface profile of the 20nm-thick alumina on the 1 μ m-thick silica-on-silicon substrate with a root mean square (RMS) roughness of less than 0.7nm, without significant differences between processes. However, Figure 5.9 (e)-(h) exhibits distinctive surface profiles of the 20nm-thick alumina on monolayer WS₂, depending on the process. Notably, the initial deposition temperature is crucial for determining uniform thin-film deposition and coverage. When depositing alumina at 150°C, as seen in Figure 5.9 (e), (f), and (h), there is a high density of pinholes with low alumina coverage.

The ALD deposition process involves both physisorption and chemisorption. Based on the Lennard-Jones potential model, the attraction force between the solid (substrate) and gas (reactants) during physisorption is lower with a larger distance than in chemisorption. Therefore, physisorption occurs first at the interface before the chemical reaction, and it is affected by the process temperature. Because 1L-TMDs lack dangling bonds on their surface, meaning chemisorption is very limited with abnormal nucleation growth, active physisorption must accompany

chemisorption. In this regard, 150°C was insufficient to facilitate physisorption, leading to numerous voids and pinholes. If the subsequent process temperature was higher than 150°C, the density of pinholes decreased, as seen in Figure 5.9 (f) and (h). However, due to the self-limiting growth characteristics of ALD, the pinholes were not perfectly filled. On the other hand, in Figure 5.9(g), the starting process temperature was 200°C, and perfect coverage with uniform thin alumina deposition was achieved.

The effect of the ALD process on the excitonic resonance in 1L-WS₂ was also investigated. Even though uniform thin dielectrics can be well-deposited on the monolayers, it is meaningless if the prominent optical property of the monolayer is not preserved or is damaged. PL quenching (decrease in intensity), peak shift, and linewidth broadening can indicate how the excitonic resonances are affected. In Figure 5.9(i)-(l), the resonance peak is red-shifted for all cases, indicating that electrons are doped after the ALD deposition. PL quenching occurs for all cases when comparing before and after deposition, mainly due to the dielectric screening effect from the alumina deposition, but it is even more severe when the sample is exposed to high temperatures for longer durations (Figure 5.10). The peak is a superposition of two Lorentzian peaks representing the exciton resonance and trion resonance. With two-Lorentzian superposition fitting, the exciton peak and trion peak were distinguished, with their respective resonance wavelengths and linewidths. In the case of Process 3, both the exciton and trion peaks were significantly broadened as 1L-WS₂ was exposed to higher temperatures for an extended time.

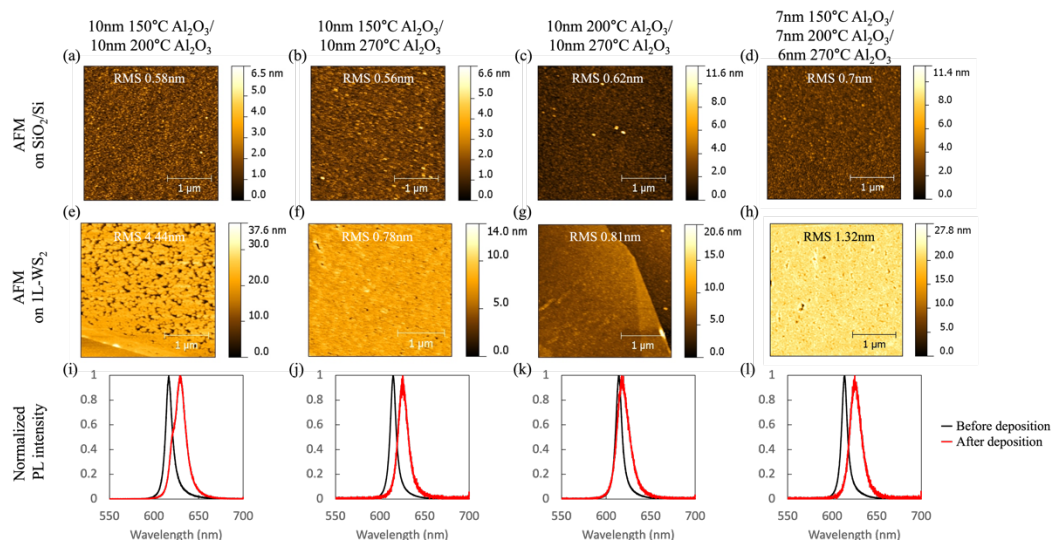


Figure 5.9 Impact of ALD process temperature during the deposition of 20nm alumina on the surface morphology and photoluminescence of 1L- WS_2 . Process 1: 10nm alumina deposited at 150°C, followed by 10nm at 200°C. Process 2: 10nm alumina deposited at 150°C, followed by 10nm at 270°C. Process 3: 10nm alumina deposited at 200°C, followed by 10nm at 270°C. Process 4: 7nm alumina deposited at 150°C, followed by 7nm at 200°C, and 6nm at 270°C. (a)-(d) depict the surface morphology of the deposited alumina on a bare silica-on-silicon substrate. (e)-(h) illustrate the surface morphology of the deposited alumina on exfoliated 1L- WS_2 . (i)-(l) represent the normalized PL intensity before and after deposition.

We investigated how physisorption can affect the morphology and optical resonances in 1L- WS_2 after alumina deposition, comparing different process temperatures. Now, to facilitate active chemisorption, we explored surface pre-treatment for functionalization. There are two common pre-treatment methods to activate the surface: oxygen plasma treatment and UV-ozone treatment. Oxygen plasma treatment promotes the nucleation of ALD by generating hydroxyl species on the surface. However, it has a critical obstacle: the pristine substrate may sustain

damage after plasma ignition due to ion bombardment from high-kinetic-energy ion/electron species (Figure 5.11).

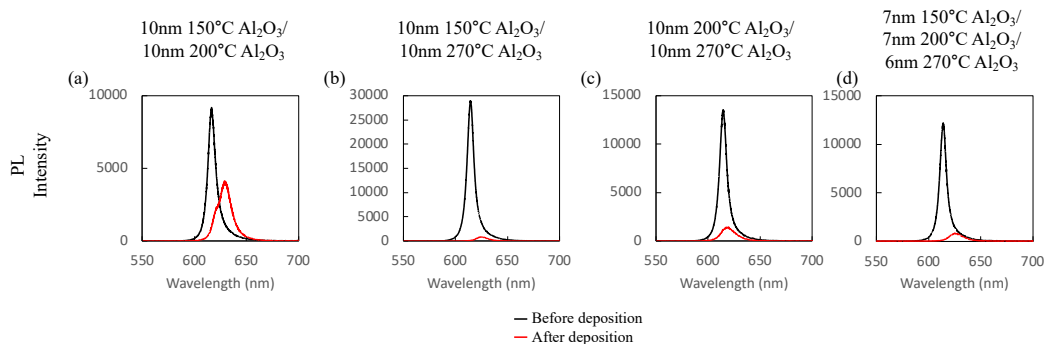


Figure 5.10 Impact of ALD process temperature during the deposition of a 20nm alumina film on the photoluminescence of 1L-WS₂. Process 1: 10nm alumina deposited at 150°C, followed by 10nm at 200°C. Process 2: 10nm alumina deposited at 150°C, followed by 10nm at 270°C. Process 3: 10nm alumina deposited at 200°C, followed by 10nm at 270°C. Process 4: 7nm alumina deposited at 150°C, followed by 7nm at 200°C, and 6nm at 270°C. (a)-(d) represent the PL intensity before and after deposition.

Room-temperature UV-ozone treatment is known to be a gentler method for the substrate. A hydrophilic surface with UV-ozone treatment and reactive radical formation can promote chemisorption during alumina deposition. By comparing Figure 5.12(a) and 2(b), the surface roughness was improved by 60% after UV-ozone treatment. Even on 1L-WS₂, the surface roughness was improved (Figure 5.12 (c) and (d)). Although the process was at 150°C, a 30nm thickness was sufficient to fill the voids or pinholes, leading to better coverage with improved smoothness when compared to the results with 20nm deposition shown in Figure 5.9. However, the PL intensity decreased by 5% after UV-ozone treatment, and both the exciton and trion peaks were twice as broad. This indicates that while UV-

ozone treatment can improve the surface quality of the alumina, it damages the optical resonances in 1L-WS₂ (Figure 5.12 (e) and (f)).

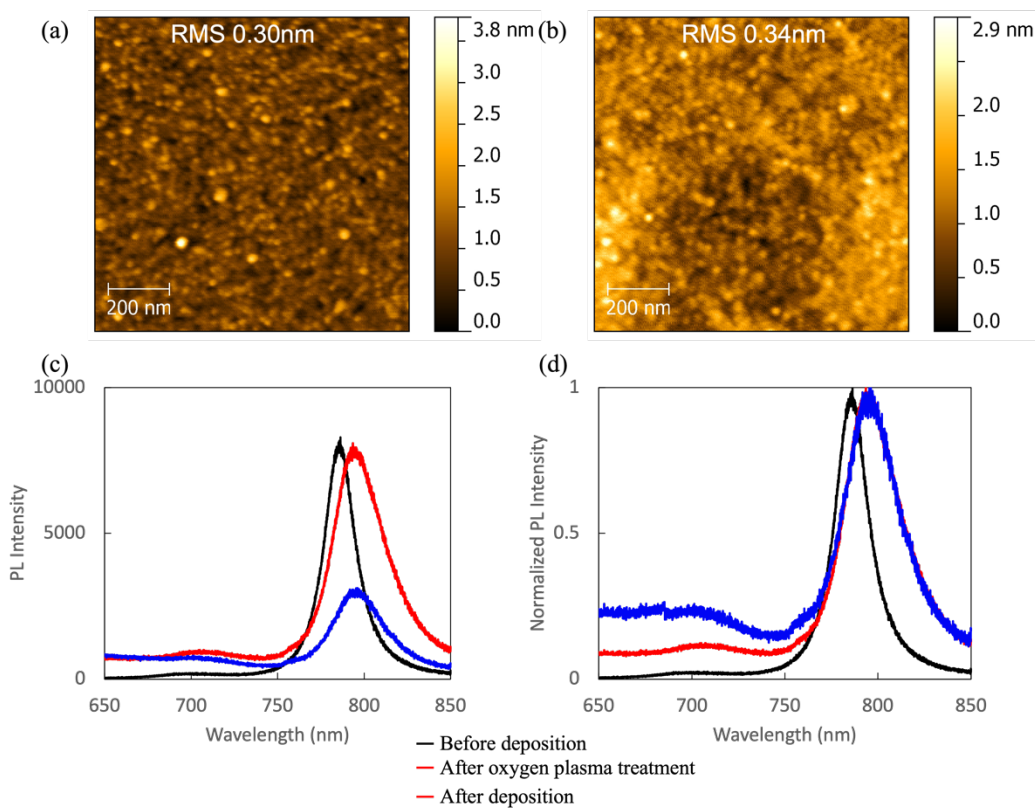


Figure 5.11 Influence of oxygen plasma surface treatment prior to alumina deposition. The first column presents the results from the deposition of a 30nm alumina film without surface treatment. The second column shows the results from the deposition of a 30nm alumina film after UV-ozone treatment. (a) depicts the surface morphology of the deposited alumina on a bare silica-on-silicon substrate. (b) illustrates the surface morphology of the deposited alumina on exfoliated 1L-MoSe₂. (c) represents the PL intensity, and (d) represents the normalized PL intensity before deposition, after treatment, and after deposition, respectively.

Next, the effect of a thicker ALD-deposited alumina layer on the morphological and optical properties of various 1L-TMDs was investigated. (Figure 5.14) The ALD process was conducted at 150°C. Overall, the grains are larger than those observed with thinner films, and this effect is even more pronounced when depositing on 1L-TMDs, with an RMS roughness of over 0.84 nm. Regarding photoluminescence (PL) quenching, 1L-MoS₂ was less affected, but the linewidth was severely broadened, similar to 1L-WS₂. All 1L-TMDs exhibited electron doping after deposition, confirmed by a red-shift in the PL peak, with 1L-WSe₂ and 1L-MoS₂ being more susceptible. The exciton linewidth of 1L-WSe₂ and 1L-MoS₂ did not change significantly, while the trion peak was broadened. Therefore, although all 1L-TMDs experienced optical degradation after the thick alumina deposition, the surface morphology remained smooth without any voids.

Higher process temperatures, thicker layer deposition, and surface treatment help improve the surface morphology of alumina on 1L-TMDs, resulting in full coverage without any voids or pinholes. However, ALD deposition optically damages 1L-TMDs, as evidenced by PL quenching and linewidth broadening. Here, we investigated different dielectric deposition methods: 2D dielectric exfoliation, PVD by electron-beam evaporation, and plasma-enhanced chemical vapor deposition (PECVD). Hexagonal boron nitride (hBN) is well-known for its good compatibility with 1L-TMDs as it is also a 2D material.

Hexagonal boron nitride (hBN) flake was transferred using a hot pick-up technique. The hBN flakes were obtained from bulk crystals (hq-graphene) and cleaved onto a pre-cleaned 300nm SiO₂ on a Si wafer (sonicated for 30 minutes in Acetone and Isopropanol (IPA), followed by oxygen plasma treatment: 100 W, 250 mTorr for 10 minutes) using Scotch tape. Desired thickness ranges of hBN flakes were identified using a combination of optical microscopy and atomic force microscopy (AFM). A dome-shaped polypropylene carbonate (PPC) coated PDMS stamp was employed to pick up the hBN flakes at temperatures between 100-110°C. The hBN flakes were then placed on each monolayer TMDs at 130-140°C. Subsequently,

after melting the PPC film at 200°C for 20 minutes, it was washed by rinsing the sample overnight in chloroform and finally in IPA.

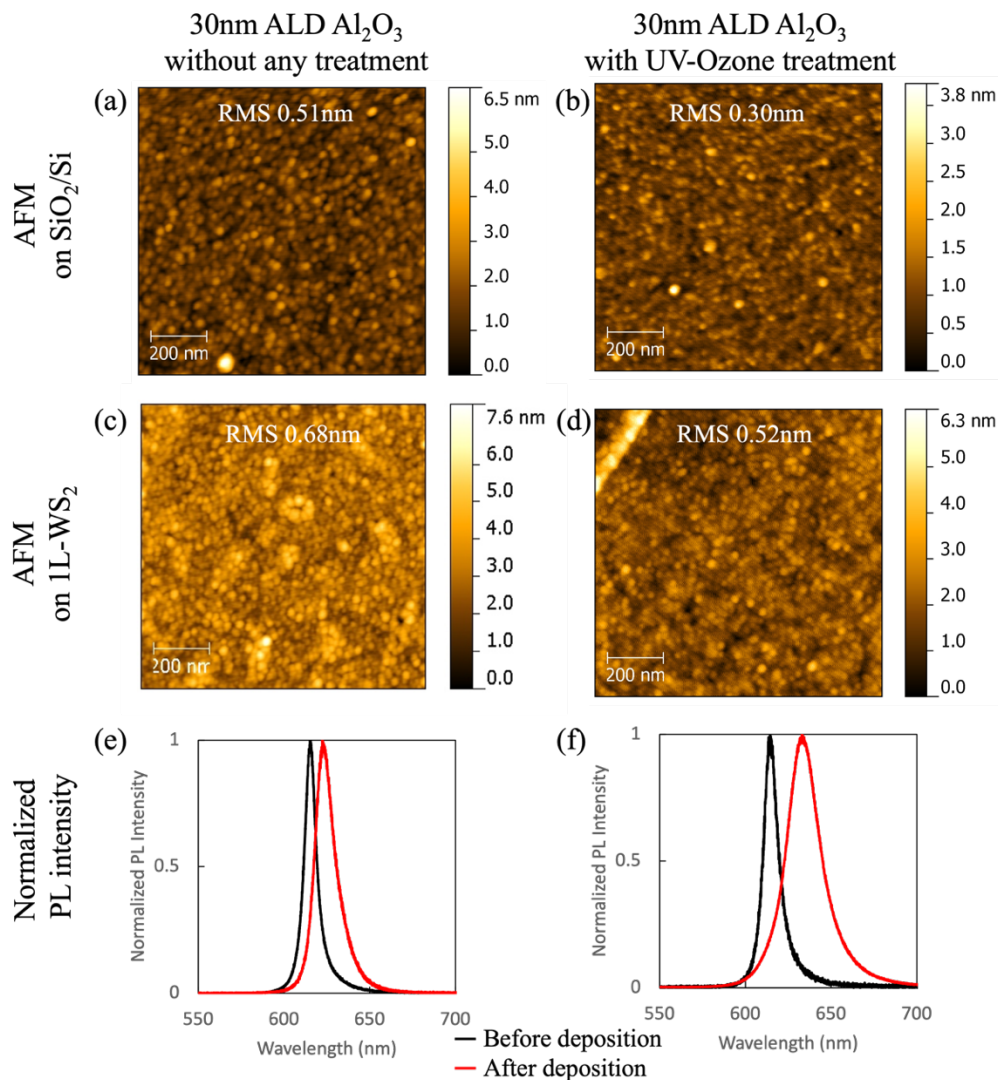


Figure 5.12 Influence of UV-ozone surface treatment prior to alumina deposition. The first column presents the results from the deposition of 30nm alumina without surface treatment. The second column shows the results from the deposition of 30nm alumina after UV-ozone treatment. (a)-(b) depict the surface morphology of the deposited alumina on a bare silica-on-silicon substrate. (c)-(d) illustrate the surface morphology of the deposited alumina on exfoliated 1L-WS₂. (e)-(f) represent the normalized PL intensity before and after deposition.

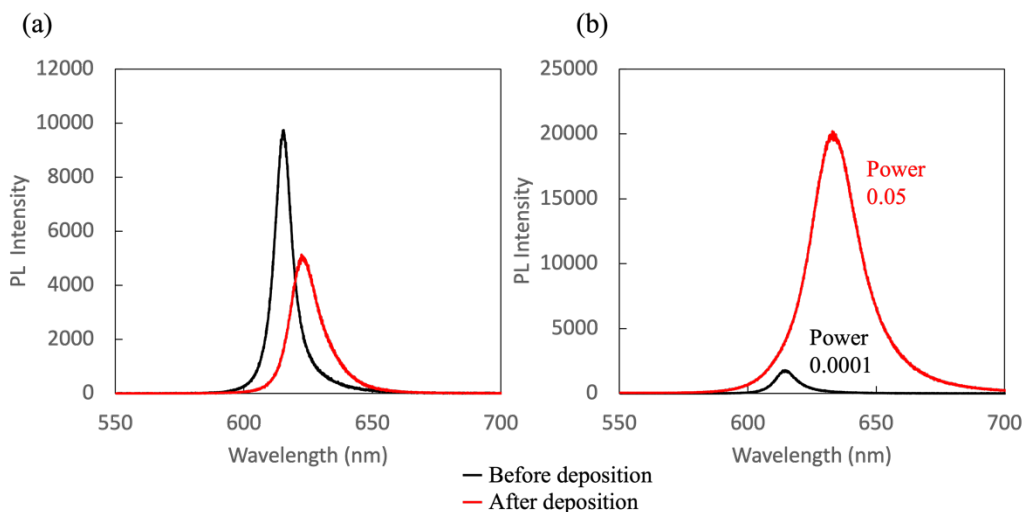


Figure 5.13 Influence of UV-ozone surface treatment prior to alumina deposition. (a) represents the PL intensity from the deposition of a 30nm alumina film without surface treatment, before and after deposition. (b) represents the PL intensity from the deposition of a 30nm alumina film after UV-ozone treatment.

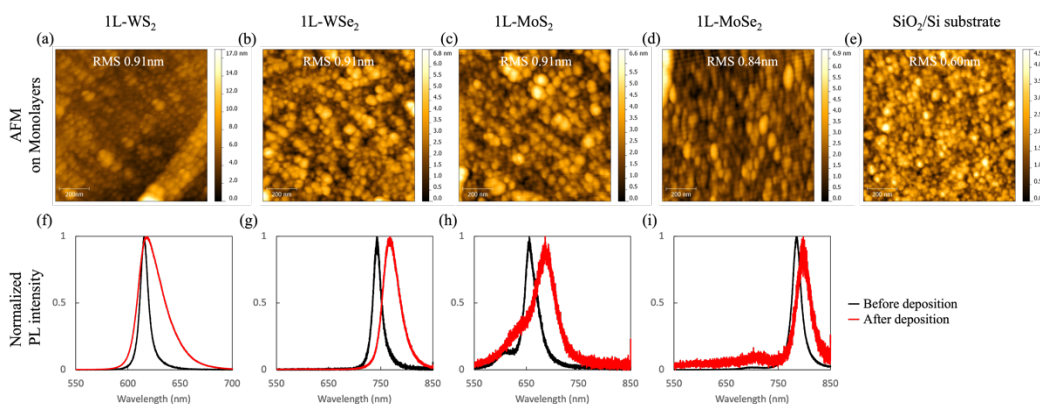


Figure 5.14 Variability in surface morphology and optical properties, as probed by PL, among different 1L-TMDs. Each column corresponds to results from 1L- WS_2 , WSe_2 , MoS_2 , MoSe_2 , and a bare SiO_2 -on-Si substrate, respectively. (a)-(e) depict the surface morphology of the deposited 179nm-thick alumina on the exfoliated monolayers. (f)-(j) represent the normalized PL intensity before and after deposition.

In Figure 5.15(a), the linewidths of the exciton and trion did not change, while a small red-shift in the peak was observed due to the dielectric screening effect. However, obtaining a large-area dielectric and aligning the flake on a desired 1L-TMD are challenging due to the exfoliation and transfer method.

Evaporated alumina and silica were also explored. Electron-beam evaporation is a type of PVD. Although an evaporated dielectric layer is not suitable for gate dielectric applications, the linewidths of the exciton and trion in 1L-WS₂ were well-preserved, as seen in Figures 4.17(b) and (c). However, PL quenching after evaporation was more severe than after ALD deposition, with evaporated alumina quenched by 14% and evaporated silica quenched by 0.4%. PECVD-deposited silica was processed at a lower temperature of 200°C than the conventional method of 300°C to minimize damage to the monolayer. However, PECVD caused the most significant damage to 1L-WS₂, as an unknown peak arose at 807 nm, which requires further investigation.

In this comprehensive study, the impact of ALD conditions on the optical and surface properties of 1L-WS₂, a representative TMD, was meticulously investigated. PL and AFM analyses unveiled the changes in surface morphology and optical characteristics of 1L-WS₂ after alumina deposition under varying process parameters, such as temperature, the number of deposition cycles, and surface pre-treatment. Uniform thin film coverage without voids was achieved by employing higher temperature processes (200-270°C) with thinner alumina layers, lower temperature processes with thicker alumina films, or UV-ozone surface pre-treatment. However, 1L-WS₂ and other monolayer TMDs suffered optical degradation after the ALD deposition, evidenced by PL quenching and linewidth broadening.

The exploration of alternative deposition techniques, including exfoliated hexagonal boron nitride, electron-beam evaporation, and plasma-enhanced chemical vapor deposition, unveiled trade-offs between preserving excitonic linewidths and challenges in obtaining large-area dielectrics or mitigating severe

photoluminescence quenching. This work underscores the delicate balance between achieving desired film properties and preserving the exceptional optical characteristics of monolayer transition metal dichalcogenides. The findings pave the way for optimizing device performance while harnessing the full potential of these two-dimensional materials in optoelectronic and nanophotonic applications.

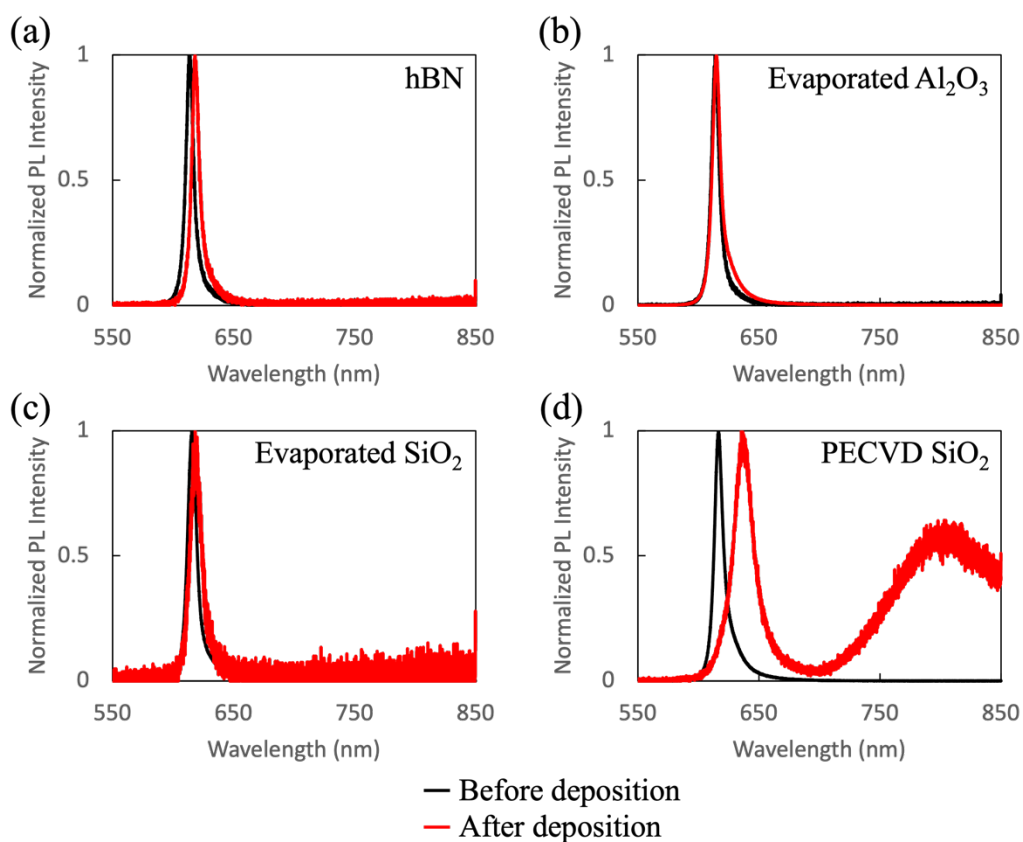


Figure 5.15 Normalized PL intensity of various gate dielectric candidates before and after deposition with (a) exfoliated and transferred hexagonal boron nitride (hBN), (b) electron-beam evaporated Al_2O_3 , (c) electron-beam evaporated SiO_2 , and (d) plasma-enhanced chemical vapor deposited SiO_2 .

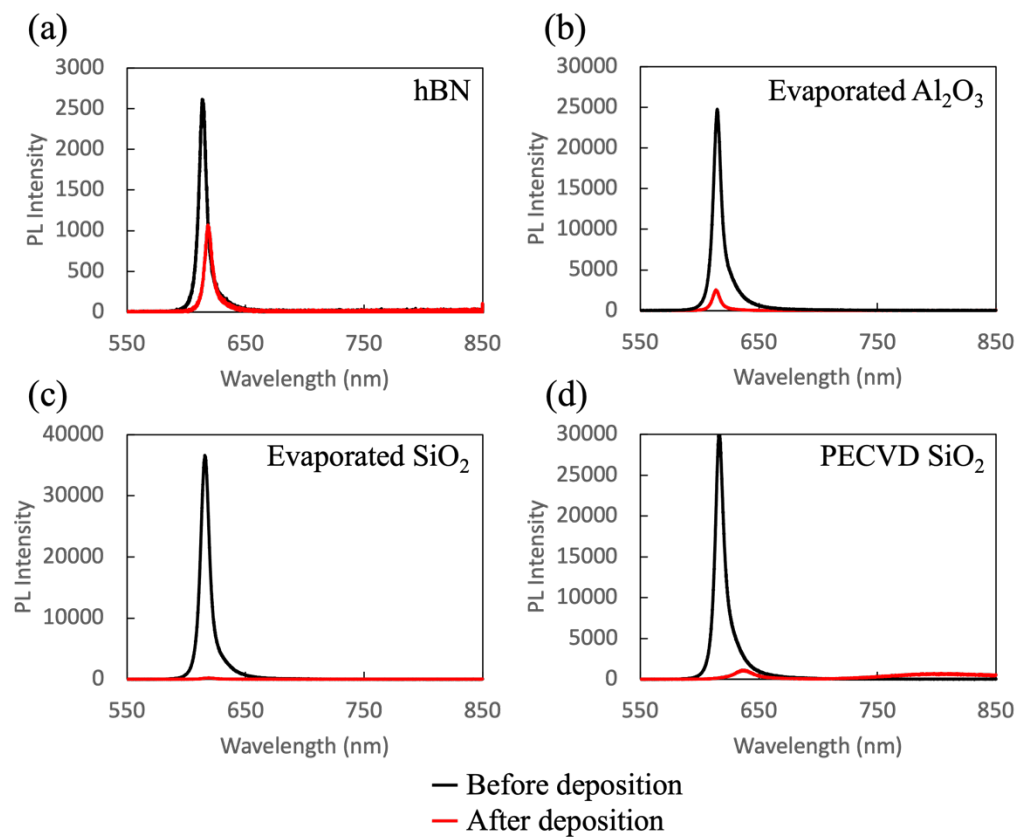


Figure 5.16 PL intensity of various gate dielectric candidates before and after deposition with (a) exfoliated and transferred hexagonal boron nitride (hBN), (b) electron-beam evaporated Al₂O₃, (c) electron-beam evaporated SiO₂, and (d) plasma-enhanced chemical vapor deposited SiO₂.

5.5 Optical response

A Fabry-Perot resonator is an optical cavity formed by two parallel reflecting mirrors. By adjusting the distance between the two mirrors, the resonant wavelength can be tuned, as described by equation 5.8:

$$d = \frac{\lambda}{2n} \quad (5.8)$$

where d is the distance between two mirrors, n is the refractive index of the cavity material, and λ is the wavelength of interest. Through transfer matrix calculations, 1L-TMDs were strategically positioned at the maximum electric field location to effectively incorporate them into the resonator. If the structure is symmetric, i.e., the reflectivity of the top and bottom mirrors is the same, the maximum electric field is situated at the center of the cavity. Researchers have studied Fabry-Perot resonator integrating 2D materials to understand the optical functionality of them^{139,169–174}. Figure 5.17 illustrates the calculated reflectance spectrum around the resonance wavelength when the mirrors are metallic or dielectric, respectively. The imaginary part of the refractive index of Au is 10.2 at 1550 nm, and since the material itself is lossy, the Q-factor of the device is low, around 95, due to the high absorption in Au. However, DBRs are lossless, resulting in a high Q-factor of around 50,000. Therefore, when 1L-TMDs are incorporated into these Fabry-Perot resonators, the optical response of the high-Q resonator is more sensitive to the loss from 1L-TMDs. However, because two dielectric mirrors require many complex fabrication steps, an Au/Au resonator was experimentally demonstrated first, followed by an Au/DBR resonator for this project.

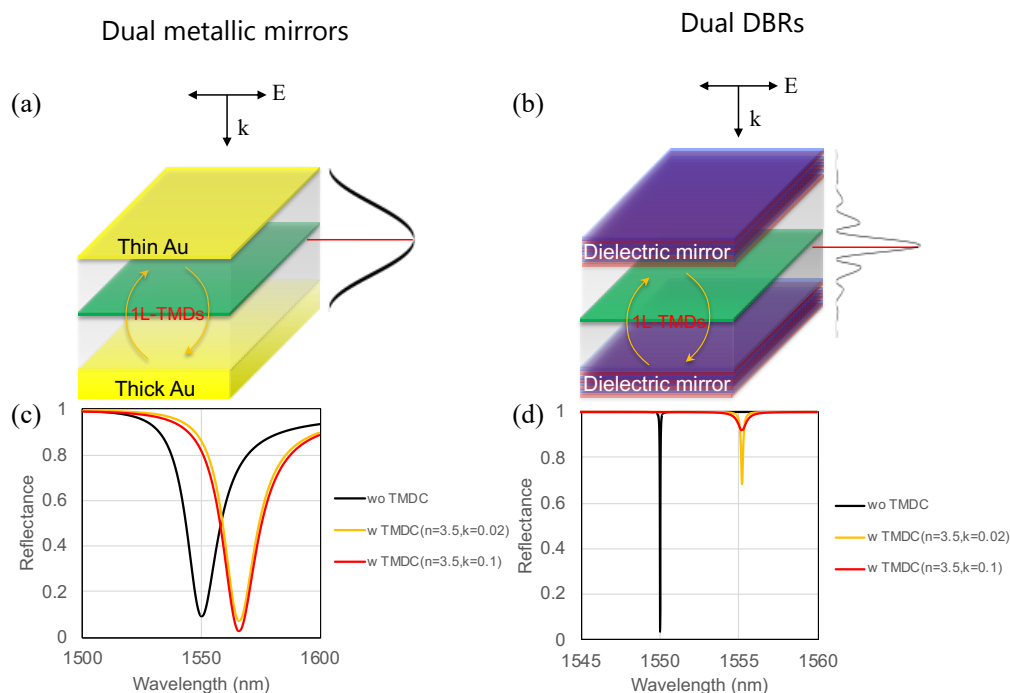


Figure 5.17 (a) Schematic diagram of a Fabry-Perot resonator consisting of dual metallic mirrors. (b) Schematic diagram of a Fabry-Perot resonator consisting of dual dielectric mirrors. (c) Reflectance spectrum of the structure in (a) depending on the presence or absence of 1L-TMDs. (d) Reflectance spectrum of the structure in (b) depending on the presence or absence of 1L-TMDs.

For the experimental demonstration of the Au/Au cavity, a 170 nm-thick Au layer was deposited onto the SiO₂ on a Si substrate, followed by the evaporation of a 236 nm SiO₂ layer as the bottom cavity. The deposition rate was 0.5 Å/s, and 4 sccm of oxygen flow was maintained during the e-beam evaporation process. Five distinct 1L-TMDs, namely WS₂, MoS₂, WSe₂, MoSe₂, and MoTe₂ were exfoliated and transferred onto the layer, as depicted in Figure 5.18 (a)-(e). After the transfer process, a PMMA layer was spin-coated as the top cavity. PMMA 495 A4 was used, and the spin-coating process was carried out at 3500 rpm with an acceleration of 10. Subsequently, the PMMA was baked at 180°C for 3 minutes. Finally, a 20

nm-thick Au layer was evaporated at a deposition rate of 1 Å/s on top of the entire structure as the top mirror.

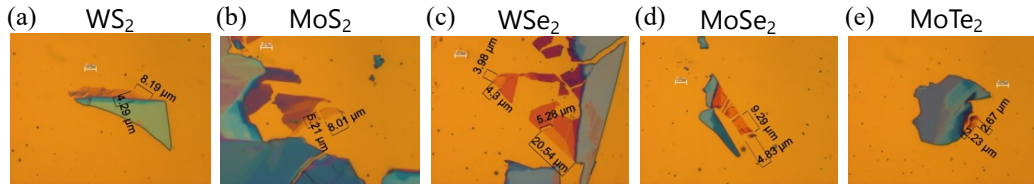


Figure 5.18 Exfoliated and transferred 1L-TMDs onto SiO₂/Au on a substrate. (a) WS₂, (b) MoS₂, (c) WSe₂, (d) MoSe₂, (e) MoTe₂.

Figure 5.19 shows the measured reflectance spectrum around the resonance for each 1L-TMD. As each material has a distinct refractive index, the resonance was red-shifted, and the linewidth was broadened. The Q-factor of the device was about 23, which is four times lower than the calculated value due to a rough surface. Because of the lossy and rough nature of Au, the position-to-position variation was larger than the shift caused by the presence of 1L-TMDs, making it difficult to distinguish the effect of 1L-TMDs (Figure 5.19 (b)-(d)). In conclusion, a higher Q Fabry-Perot resonator was required to utilize 1L-TMDs for active nanophotonics applications.

To achieve a higher Q-factor device, an Au/DBR Fabry-Perot resonator was devised. The top Au layer serves a dual role as the top mirror and the top electrode to inject carriers into the 1L-TMDs. The bottom DBR was coated with 13 pairs of SiO₂ and Nb₂O₅ on a double-sided polished silica substrate, providing a reflectivity of 99.984% at a wavelength of 1550 nm.

The optical setup configuration is described in Figure 5.20. The Fabry-Perot resonator exhibits angle dependence; therefore, beam collimation is crucial to

obtain an appropriate optical response from the resonator. To collimate the beam, a lens was positioned at the back focal plane, as illustrated in Figure 5.20 (b).

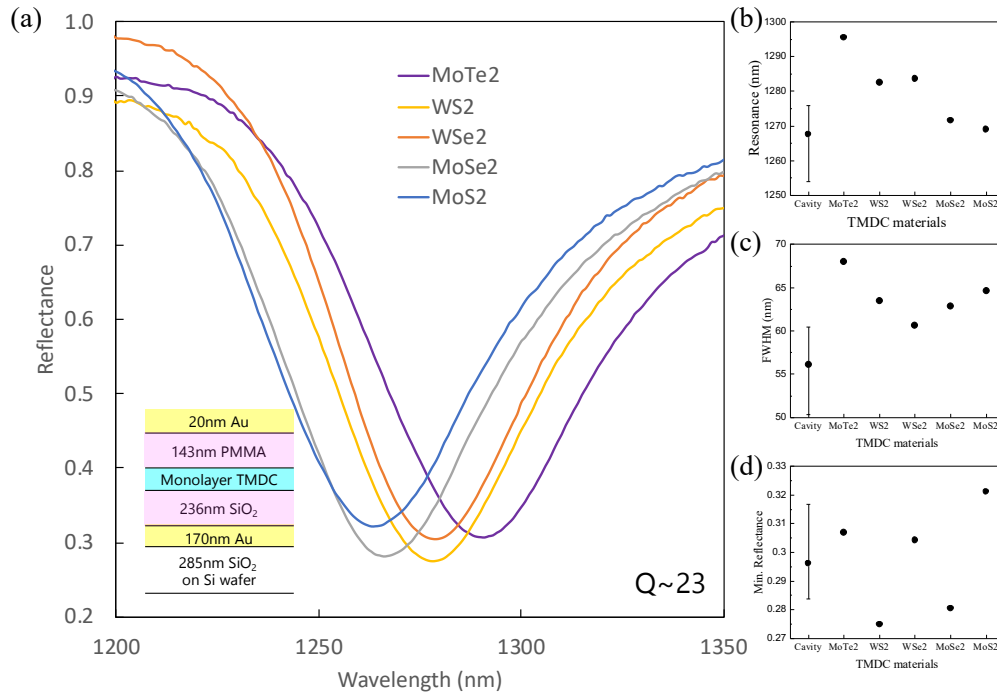


Figure 5.19 (a) Reflectance spectrum of 5 distinct 1L-TMDs embedded in an Au/Au Fabry-Perot resonator. (b) Resonance wavelength of each material. (c) Full-width at half-maximum (FWHM) of the reflectance response fitted by a Lorentzian curve. (d) Minimum reflectance of the reflectance response.

With the optical setup, the effect of varying the top Au thickness from 50 nm to 70 nm on the reflection and transmission responses was analyzed. The same device was used for the reflectance measurements shown in Figure 5.21 (a) and (b), and the response differed significantly depending on whether the beam was collimated or not. These experiments and analyses demonstrate the importance of beam collimation.

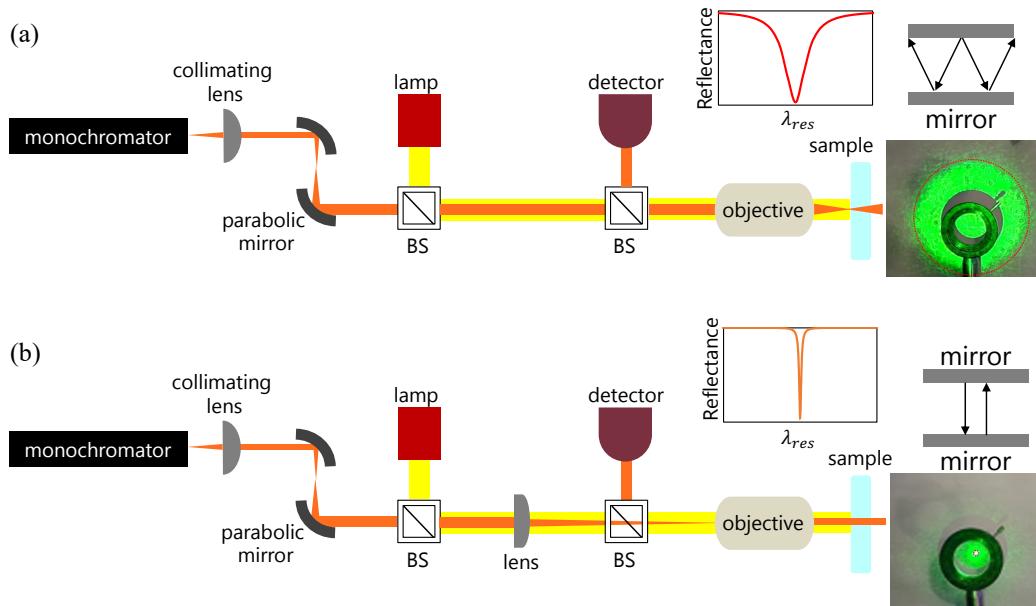


Figure 5.20 Optical setup configuration for NIR reflection response. (a) No beam collimation. (b) Beam collimation achieved by locating a lens at the back focal plane of an objective.

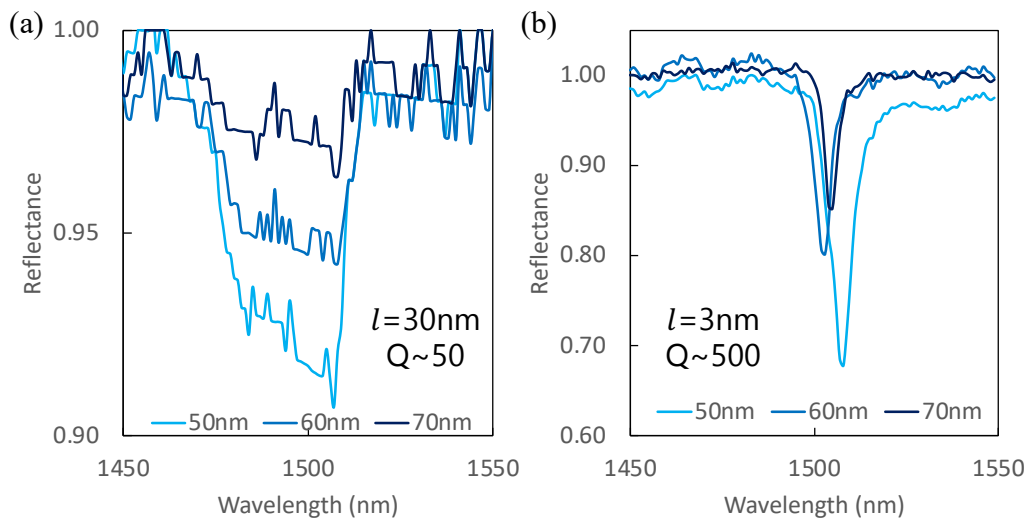


Figure 5.21 Reflectance spectrum as a function of top Au thickness from 50 nm to 70 nm. (a) Reflectance spectrum measured by the setup without beam collimation. (b) Reflectance spectrum measured by the setup with beam collimation.

However, with the setup, the linewidth of the beam was 4.23 nm with a slit width of 300 μm , and the wavelength sensitivity was too low to detect the small wavelength shift caused by the presence of 1L-TMDs. Therefore, an optimized setup was employed for the optical analysis (Figure 5.22). We improved the measurement setup to achieve a high-Q transmittance response with a fitting error margin of only 0.1 nm.

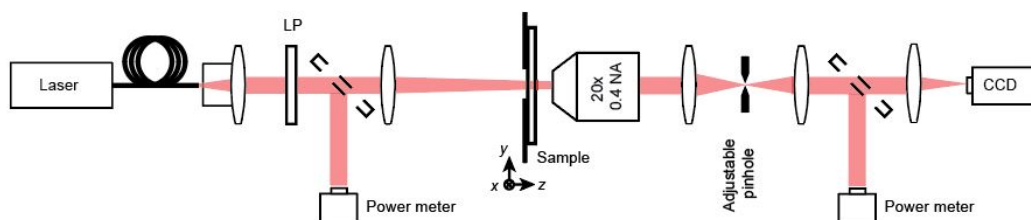


Figure 5.22 Optical setup configuration for NIR transmission response.

By increasing the thickness of the top Au layer, the linewidth narrowed from 3.2 nm to 1.2 nm when decreasing from 50 nm to 70 nm. (Figure 5.23) These values were in good agreement with the transfer matrix calculations, and the theoretical limit was reached. In this device, a Q-factor of 1219 was successfully achieved without the incorporation of 1L-TMDs.

As discussed in the previous section, the compatibility between 1L-TMDs and conventional deposition processes is crucial for incorporating 1L-TMDs into the Fabry-Perot resonator. Additionally, the optical response of the Fabry-Perot resonator is angle-dependent, so the smoothness and uniformity of each layer, as well as precise thickness control to achieve the desired resonance wavelength, are also essential. The selection of the cavity material and the process was the most challenging part because the cavity itself also serves as the gate dielectric.

Nine dielectric materials were selected as candidate materials, as shown in Figure 5.24 (a). Ideally, a material with a large dielectric constant and a substantial dielectric strength can provide effective carrier injection into the 1L-TMDs.

However, not only the gate dielectric properties but also the process compatibility with 1L-TMDs and the smoothness of the layer for achieving a high Q-factor in the Fabry-Perot device must be considered. Therefore, various processes, including e-beam evaporation, PECVD, ALD, exfoliation and transfer, and spin coating, were explored. Figure 5.25 illustrates how each material was evaluated based on three main criteria.

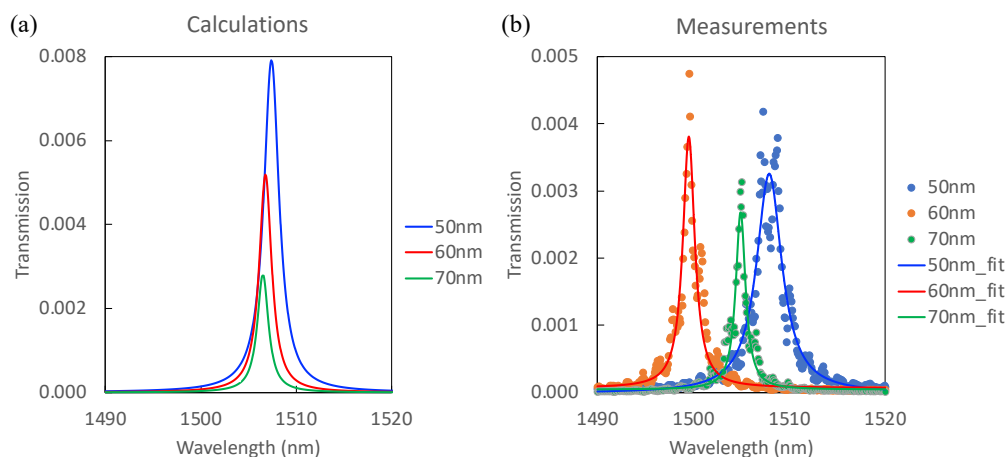


Figure 5.23 (a) Calculated and (b) Measured transmittance spectrum as a function of the top Au thickness.

Not only inorganic gate dielectrics but also organic gate dielectrics that can be spin-coated were explored, as the spin-coating process was assumed to be gentler than conventional vacuum deposition techniques. (Figure 5.26) However, it transpired that SU-8 and HSQ inflicted damage on 1L-TMDs, as evidenced by PL measurements before and after the coating process. The emergence of additional peaks, excluding exciton and trion peaks, implied the introduction of defects or undesirable chemical reactions subsequent to the coating. PMMA appeared promising, as it did not degrade 1L-TMDs; however, its gate dielectric properties were suboptimal, as devices with a PMMA gate dielectric readily reached breakdown.

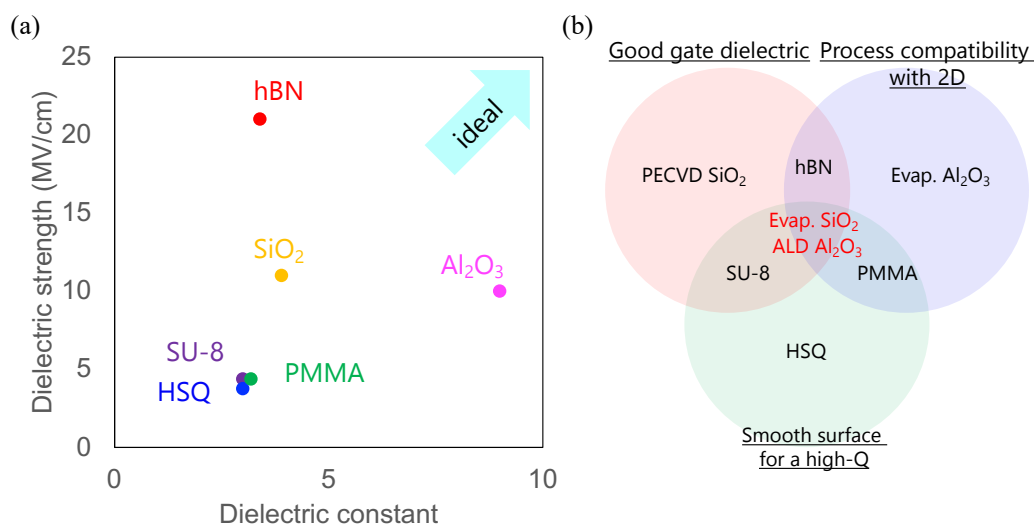


Figure 5.24 (a) Dielectric constant and dielectric strength of various gate dielectric candidate materials. (b) Gate dielectric evaluation and selection rules.

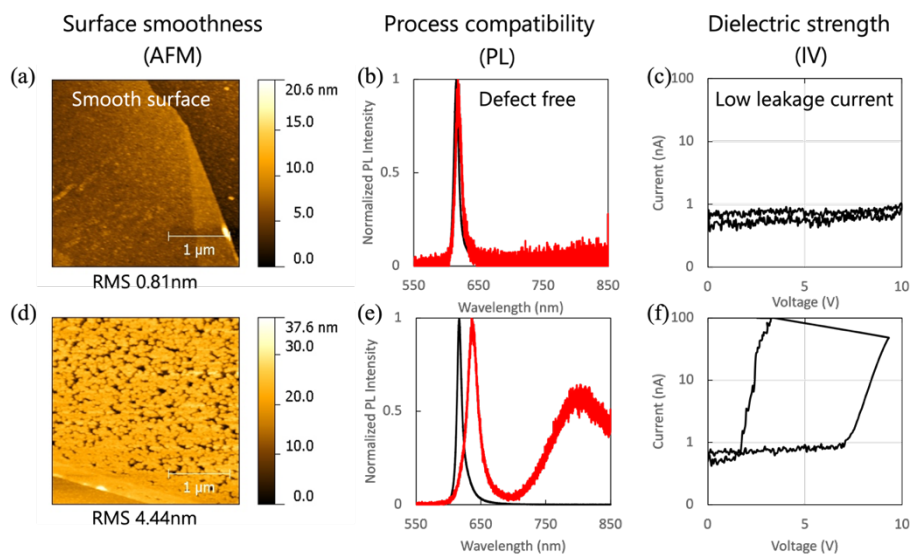


Figure 5.25 Three main criteria to select a gate dielectric. The first row represents an ideal example, and the second row depicts an unfavorable scenario. (a) and (d) Surface smoothness measured by atomic force microscopy (AFM). (b) and (e) Process compatibility evaluated by photoluminescence (PL) measurements. (c) and (f) Dielectric strength assessed by current-voltage (I-V) measurements using a probe station.

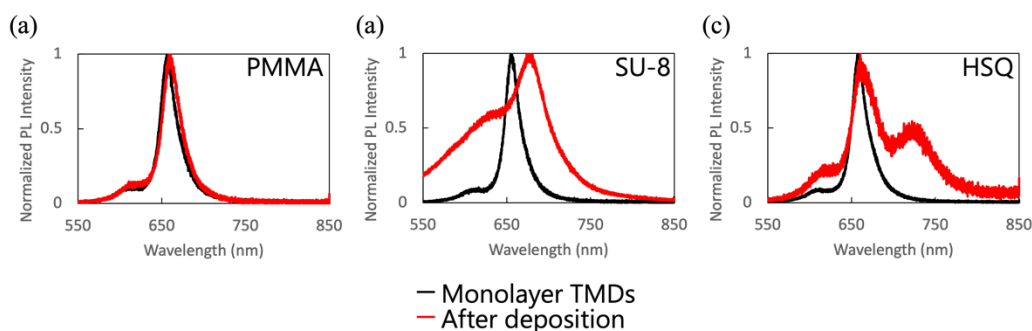


Figure 5.26 Normalized PL intensity before and after spin-coating of (a) PMMA, (b) SU-8, (c) HSQ.

E-beam evaporated SiO_2 , exfoliated and transferred hexagonal boron nitride (hBN), and ALD-deposited Al_2O_3 were selected and incorporated with 1L-TMDs. Figure 5.27 depicts an initial device comprising 1L- WS_2 as the active material, evaporated SiO_2 as the gate dielectric, and a 50 nm-thick Au layer as the top electrode. The resonance existed in the near-infrared (NIR) region, and an IR camera was employed to locate the monolayer at the specific wavelength of interest. After defining the active region with an iris, the transmittance spectrum was measured using the IR setup. By comparing the optical response of the Fabry-Perot resonator without 1L- WS_2 to the response from 1L- WS_2 , it was observed that the 1L- WS_2 response exhibited red-shifted and broader peaks. This implied that 1L- WS_2 possessed a distinct refractive index with absorption. By injecting carriers to analyze the electrical doping effect of 1L-TMDs on the optical response, the resonance peak was analyzed. However, the linewidth was 5.4 nm due to a low Q-factor, and the peak shift was less than the linewidth, implying that the errors from measurements and fitting were larger than the actual peak shift arising from electrical doping. Consequently, efforts were undertaken to deposit each layer as smoothly as possible to improve the Q-factor.

Therefore, a Q-factor of 1000 was achieved with evaporated SiO_2 (Figure 5.28 (a)). SiO_2 evaporation was challenging since oxide materials undergo sublimation.

Consequently, the beam shape was modified from a small circle to a fast-frequency large spiral sweep. Additionally, the grain size of the SiO₂ target source material was reduced from 3-6 μm to 1-3 μm to improve uniform sublimation. Furthermore, there was a trade-off in determining the deposition rate. A faster deposition rate yielded a rougher surface, but the increase in chamber temperature could be marginal. A slower deposition rate produced a smoother surface, but the chamber temperature increase was substantial, leading to an increase in root-mean-square (RMS) roughness. Deposition rates ranging from 0.1 $\text{\AA}/\text{s}$ to 4 $\text{\AA}/\text{s}$ were explored to optimize the smoothness of the SiO₂ layer. The optimized value was 2 $\text{\AA}/\text{s}$.

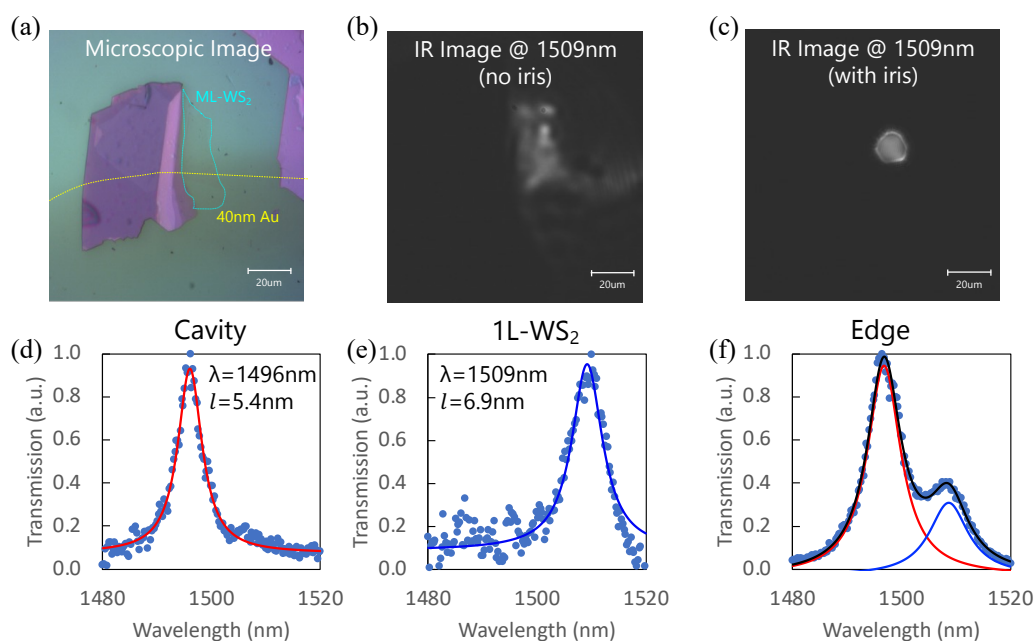


Figure 5.27 Optical responses of a 1L-WS₂ embedded Fabry-Perot resonator. (a) Microscopic image of the device. (b) IR image measured at the wavelength of 1509 nm. (c) IR image taken at the same position as in (b), but with an iris to limit the measurement area. Transmittance spectrum at (d) the cavity without 1L-WS₂, (e) the cavity with 1L-WS₂, (f) the edge of 1L-WS₂ and the cavity.

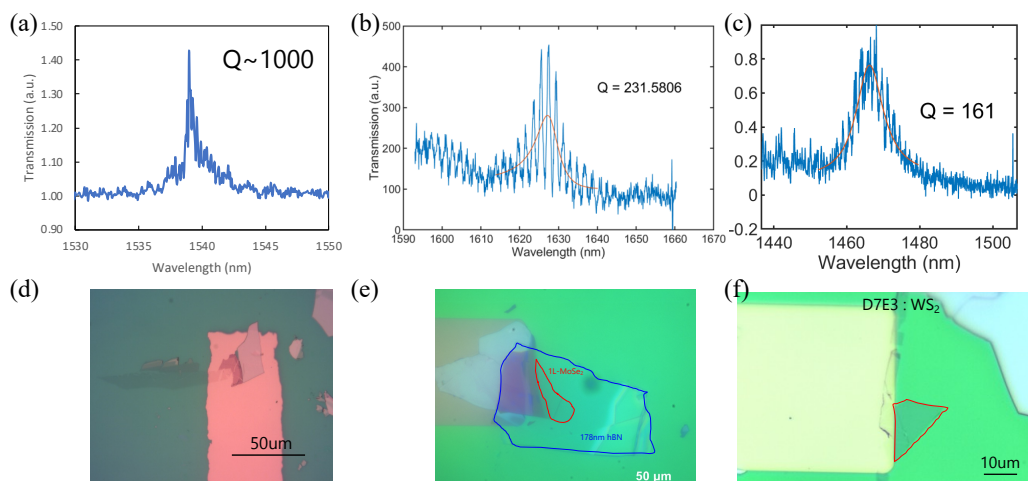


Figure 5.28 Transmittance spectrum of different Fabry-Perot resonators: (a) evaporated SiO_2 , (b) exfoliated and transferred hBN, (c) thin ALD-deposited Al_2O_3 and thick PECVD-deposited SiO_2 . (d)-(e) are corresponding microscopic images of each device.

Figure 5.28 (b) and (c) showcase a different Fabry-Perot resonator that employed an hBN flake and a 30 nm ALD-deposited Al_2O_3 layer followed by a 170 nm PECVD-deposited SiO_2 layer as the gate dielectric, respectively. hBN is a well-known material for a good gate dielectric with compatibility for 1L-TMDs, as it is also exfoliated and transferred. However, it was found that an hBN flake was not an ideal match for the Fabry-Perot resonator, exhibiting a low Q-factor optical response. Based on AFM analysis, a thick hBN flake exhibited thickness variations from one position to another¹⁷⁵, and the flake size was not sufficiently large, leading to interference effects at the edges in the optical response. The combination of a 30 nm ALD-deposited Al_2O_3 layer and a 170 nm PECVD-deposited SiO_2 layer was selected because PECVD significantly damages 1L-TMDs but offers prominent dielectric strength. On the other hand, ALD is a gentler process for 1L-TMDs compared to PECVD, but the tool was not optimized for thicker dielectrics. Therefore, the combination of ALD and PECVD was attempted. However,

unfortunately, there was an air gap between the two gate dielectric materials, resulting in poor dielectric strength and a rough surface.

Figure 5.29 depicts another device comprising 1L-MoSe₂ as the active material, a 941 nm-thick SiO₂ layer as the gate dielectric, and a 62 nm-thick Au layer as the top mirror. The Q-factor of the device was around 700, as shown in Figure 5.29 (a). Figure 5.29 (b)-(c) illustrates the optical response modulation without 1L-MoSe₂, and no modulation was expected since there was no active material present. However, a 0.3 nm resonance shift was observed, attributed to measurement error. Figure 5.29 (d)-(e) shows the optical modulation in 1L-MoSe₂ with electrical gating. A substantial jump was observed at -50V, but unfortunately, this was not due to 1L-MoSe₂ but rather the breakdown of the evaporated SiO₂. By applying bias multiple times to the device, the evaporated SiO₂ readily reached breakdown.

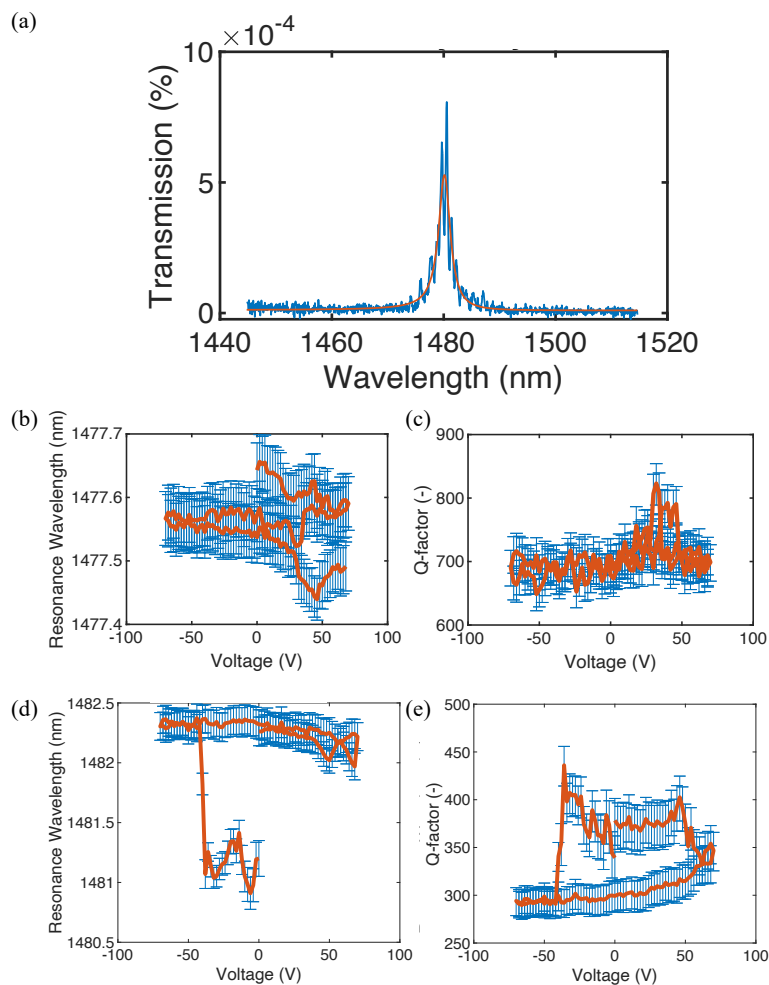


Figure 5.29 Optical response of a 1L-MoSe₂ embedded Fabry-Perot resonator. (a) Transmittance spectrum at the resonance. (b) Resonance wavelength modulation. (c) Q-factor modulation on the cavity without 1L-MoSe₂ under electrical bias. (d) Resonance wavelength modulation. (e) Q-factor modulation on the 1L-MoSe₂ under electrical bias. The voltage sweep was from 0 to positive 75V, to negative 75V, and back to 0V. The evaporated SiO₂ reached breakdown during the measurement at -50V application. The blue error bars in (b)-(e) represent the error from the fitting.

5.6 Conclusion and future work

1L-TMDs are emerging materials known for their dynamically tunable refractive indices around excitonic resonances under external stimuli. Due to the intrinsic strong resonances in monolayers, they are highly attractive for active nanophotonic device applications. We experimentally demonstrated the interaction of four types of 1L-TMDs with visible light under electrical bias at room temperature. By measuring the reflectance response of each material, we extracted the refractive index, including the resonance wavelength, oscillator strength, and linewidth, as functions of the applied bias. These results can guide the selection of appropriate materials for various electro-optic applications. Additionally, we explored the potential of employing their electro-optic modulation in telecommunication band applications beyond their excitonic resonance wavelength.

For the experimental demonstration of Fabry-Perot resonators embedded with 1L-TMDs for optical modulation under electrical doping, it is crucial to assess their compatibility with conventional deposition techniques. However, their unique surface chemistry poses challenges. ALD, a widely used thin-film deposition method, enables uniform, dense deposition and precise thickness control, making it suitable for gate dielectric applications. We investigated the impact of ALD deposition conditions, such as temperature, surface treatment, and duration, on the optical properties and surface morphologies of 1L-TMDs using PL measurements and AFM. Additionally, we explored the variability in optical and surface characteristics among different monolayers.

Finally, we experimentally demonstrated Fabry-Perot resonators embedded with 1L-TMDs. Although Au/Au resonators with 1L-TMDs were successfully fabricated, the Q-factor was too low to detect the resonance shift due to electrical doping of the 1L-TMDs. Therefore, we fabricated Au/DBR resonators with 1L-TMDs. Selecting a gate dielectric, which also serves as a cavity, was challenging because it requires an ultrasoft layer and precise thickness control while preserving the 1L-TMDs after deposition. A Q-factor of 1000, approaching the theoretical limit, was achieved with

evaporated SiO₂. However, this was still insufficient to detect optical modulation larger than the errors from fitting and measurements.

Several issues were identified: First, a thick gate dielectric over 200 nm was not suitable for creating a good gate dielectric without pinholes, as it easily reaches breakdown, making it difficult to dope the 1L-TMDs. Second, any deposition on 1L-TMDs leads to PL quenching, indicating that the 1L-TMDs are not perfectly preserved, resulting in a smaller refractive index change. Lastly, the refractive index change in the NIR might not be as significant as expected.

Higher Q-factor devices can significantly increase the sensitivity to detect small optical changes in 1L-TMDs. Additionally, developing different deposition techniques to preserve intact 1L-TMDs remains an important area of research.

BIBLIOGRAPHY

1. Maier, S. A. *Plasmonics: Fundamentals and Applications*. (Springer, New York, 2007).
2. Kamali, S. M., Arbabi, E., Arbabi, A. & Faraon, A. A review of dielectric optical metasurfaces for wavefront control. *Nanophotonics* **7**, 1041–1068 (2018).
3. Yu, N. *et al.* Light Propagation with Phase Discontinuities: Generalized Laws of Reflection and Refraction. *Science* **334**, 333–337 (2011).
4. Chen, H.-T., Taylor, A. J. & Yu, N. A review of metasurfaces: physics and applications. *Rep. Prog. Phys.* **79**, 076401 (2016).
5. Lalanne, P. From Diffractive optics to meta- surfaces: basics. 56.
6. Chang, S., Guo, X. & Ni, X. Optical Metasurfaces: Progress and Applications. *Annu. Rev. Mater. Res.* **48**, 279–302 (2018).
7. Capasso, F. Flat Optics based on Metasurfaces. 31.
8. Chen, H.-T., Taylor, A. J. & Yu, N. A review of metasurfaces: physics and applications. *Rep. Prog. Phys.* **79**, 076401 (2016).
9. Yu, N. & Capasso, F. Flat optics with designer metasurfaces. *Nat. Mater.* **13**, 139–150 (2014).
10. Hsiao, H.-H., Chu, C. H. & Tsai, D. P. Fundamentals and Applications of Metasurfaces. *Small Methods* **1**, 1600064 (2017).

11. Genevet, P., Capasso, F., Aieta, F., Khorasaninejad, M. & Devlin, R. Recent advances in planar optics: from plasmonic to dielectric metasurfaces. *Optica* **4**, 139 (2017).
12. Kuznetsov, A. I. *et al.* Roadmap for Optical Metasurfaces. *ACS Photonics* acsphotronics.3c00457 (2024) doi:10.1021/acsphotronics.3c00457.
13. Emboras, A. *et al.* Electrically Controlled Plasmonic Switches and Modulators. *IEEE J. Sel. Top. Quantum Electron.* **21**, 276–283 (2015).
14. Zhang, Y. *et al.* Electrically reconfigurable non-volatile metasurface using low-loss optical phase-change material. *Nat. Nanotechnol.* **16**, 661–666 (2021).
15. Shaltout, A. M., Shalaev, V. M. & Brongersma, M. L. Spatiotemporal light control with active metasurfaces. *Science* **364**, eaat3100 (2019).
16. Thureja, P. *et al.* Toward a universal metasurface for optical imaging, communication, and computation. *Nanophotonics* **11**, 3745–3768 (2022).
17. Qiao, P., Yang, W. & Chang-Hasnain, C. J. Recent advances in high-contrast metastructures, metasurfaces, and photonic crystals. *Adv. Opt. Photonics* **10**, 180 (2018).
18. Shaltout, A., Kildishev, A. & Shalaev, V. Time-varying metasurfaces and Lorentz non-reciprocity. *Opt. Mater. Express* **5**, 2459 (2015).
19. Cui, T., Bai, B. & Sun, H.-B. Tunable Metasurfaces Based on Active Materials. *Adv. Funct. Mater.* **29**, 1806692 (2019).
20. Valov, I. & Staikov, G. Nucleation and growth phenomena in nanosized electrochemical systems for resistive switching memories. *J. Solid State Electrochem.* **17**, 365–371 (2013).

21. Choi, B. J. *et al.* Resistive switching mechanism of TiO₂ thin films grown by atomic-layer deposition. *J. Appl. Phys.* **98**, 033715 (2005).
22. Chae, S. C. *et al.* Random Circuit Breaker Network Model for Unipolar Resistance Switching. *Adv. Mater.* **20**, 1154–1159 (2008).
23. Lee, M.-J. *et al.* Electrical Manipulation of Nanofilaments in Transition-Metal Oxides for Resistance-Based Memory. *Nano Lett.* **9**, 1476–1481 (2009).
24. Yang, J. J., Strukov, D. B. & Stewart, D. R. Memristive devices for computing. *Nat. Nanotechnol.* **8**, 13–24 (2013).
25. Emboras, A. *et al.* Nanoscale Plasmonic Memristor with Optical Readout Functionality. *Nano Lett.* **13**, 6151–6155 (2013).
26. Koch, U., Hoessbacher, C., Emboras, A. & Leuthold, J. Optical memristive switches. *J. Electroceramics* **39**, 239–250 (2017).
27. Battal, E., Ozcan, A. & Okyay, A. K. Resistive Switching-based Electro-Optical Modulation. *Adv. Opt. Mater.* **2**, 1149–1154 (2014).
28. Emboras, A. *et al.* Atomic Scale Plasmonic Switch. *Nano Lett.* **16**, 709–714 (2016).
29. Dong, S., Zhang, K., Yu, Z. & Fan, J. A. Electrochemically Programmable Plasmonic Antennas. *ACS Nano* **10**, 6716–6724 (2016).
30. Di Martino, G., Tappertzhofen, S., Hofmann, S. & Baumberg, J. Nanoscale Plasmon-Enhanced Spectroscopy in Memristive Switches. *Small* **12**, 1334–1341 (2016).

31. Schoen, D. T., Holsteen, A. L. & Brongersma, M. L. Probing the electrical switching of a memristive optical antenna by STEM EELS. *Nat. Commun.* **7**, (2016).
32. Thyagarajan, K., Sokhoyan, R., Zornberg, L. & Atwater, H. A. Millivolt Modulation of Plasmonic Metasurface Optical Response via Ionic Conductance. *Adv. Mater.* **29**, 1701044 (2017).
33. Pan, F., Gao, S., Chen, C., Song, C. & Zeng, F. Recent progress in resistive random access memories: Materials, switching mechanisms, and performance. *Mater. Sci. Eng. R Rep.* **83**, 1–59 (2014).
34. Waser, R., Dittmann, R., Staikov, G. & Szot, K. Redox-Based Resistive Switching Memories - Nanoionic Mechanisms, Prospects, and Challenges. *Adv. Mater.* **21**, 2632–2663 (2009).
35. Mohammad, B. *et al.* State of the art of metal oxide memristor devices. *Nanotechnol. Rev.* **5**, (2016).
36. Kavehei, O. *et al.* The fourth element: characteristics, modelling and electromagnetic theory of the memristor. *Proc. R. Soc. Math. Phys. Eng. Sci.* **466**, 2175–2202 (2010).
37. Sahoo, S. & Prabakaran, S. R. S. Nano-Ionic Solid State Resistive Memories (ReRAM): A Review. *J. Nanosci. Nanotechnol.* **17**, 72–86 (2017).
38. Mazumder, P., Kang, S. M. & Waser, R. Memristors: Devices, Models, and Applications [Scanning the Issue]. *Proc. IEEE* **100**, 1911–1919 (2012).
39. Gale, E. TiO₂-based memristors and ReRAM: materials, mechanisms and models (a review). *Semicond. Sci. Technol.* **29**, 104004 (2014).

40. Akinaga, H. & Shima, H. Resistive Random Access Memory (ReRAM) Based on Metal Oxides. *Proc. IEEE* **98**, 2237–2251 (2010).
41. Slesazeck, S. & Mikolajick, T. Nanoscale resistive switching memory devices: a review. *Nanotechnology* **30**, 352003 (2019).
42. Lee, J. S., Lee, S. & Noh, T. W. Resistive switching phenomena: A review of statistical physics approaches. *Appl. Phys. Rev.* **2**, 031303 (2015).
43. Jeong, D. S. *et al.* Emerging memories: resistive switching mechanisms and current status. *Rep. Prog. Phys.* **75**, 076502 (2012).
44. Sawa, A. Resistive switching in transition metal oxides. *Mater. Today* **11**, 28–36 (2008).
45. Waser, R., Dittmann, R., Staikov, G. & Szot, K. Redox-Based Resistive Switching Memories – Nanoionic Mechanisms, Prospects, and Challenges. *Adv. Mater.* **21**, 2632–2663 (2009).
46. Zhang, Y. *et al.* Compact non-volatile ferroelectric electrostatic doping optical memory based on the epsilon-near-zero effect. *Appl. Opt.* **62**, 950 (2023).
47. Emboras, A. *et al.* Opto-electronic memristors: Prospects and challenges in neuromorphic computing. *Appl. Phys. Lett.* **117**, 230502 (2020).
48. Hoessbacher, C. *et al.* The plasmonic memristor: a latching optical switch. *Optica* **1**, 198 (2014).
49. Kravets, V. G. *et al.* Plasmon-induced nanoscale quantised conductance filaments. *Sci. Rep.* **7**, (2017).

50. Baraldi, G., García Pardo, M., Gonzalo, J., Serna, R. & Toudert, J. Self-Assembled Nanostructured Photonic-Plasmonic Metasurfaces for High-Resolution Optical Thermometry. *Adv. Mater. Interfaces* **5**, 1800241 (2018).
51. Li, D. *et al.* The realization of optical switching generated from the combination of Ag/a-Si/p-Si memristor and silicon waveguide. in (eds. Zhang, X., Li, B. & Yu, C.) 1001909 (Beijing, China, 2016). doi:10.1117/12.2245695.
52. Morichetti, F. *et al.* Electrochemical optical actuators: Controlling the light through ions. in *2016 18th International Conference on Transparent Optical Networks (ICTON)* 1–4 (IEEE, Trento, Italy, 2016). doi:10.1109/ICTON.2016.7550296.
53. Emboras, A. *et al.* Plasmonic Switches. 3.
54. Babicheva, V. E., Boltasseva, A. & Lavrinenko, A. V. Transparent conducting oxides for electro-optical plasmonic modulators. *Nanophotonics* **4**, (2015).
55. Emboras, A. *et al.* Electrically Controlled Plasmonic Switches and Modulators. *IEEE J. Sel. Top. Quantum Electron.* **21**, 276–283 (2015).
56. Yang, S., Wu, J. & Christou, A. Initial stage of silver electrochemical migration degradation. *Microelectron. Reliab.* **46**, 1915–1921 (2006).
57. Whittingham, M. S. & Huggins, R. A. Transport Properties of Silver Beta Alumina. *J. Electrochem. Soc.* **118**, 1 (1971).
58. Jana, D. & De, G. Spontaneous generation and shape conversion of silver nanoparticles in alumina sol, and shaped silver nanoparticle incorporated alumina films. *J. Mater. Chem.* **21**, 6072 (2011).

59. Vu, K. Silver Migration – The Mechanism and Effects on Thick-Film Conductors. 21.
60. Busby, Y. *et al.* Direct observation of conductive filament formation in Alq₃ based organic resistive memories. *J. Appl. Phys.* **118**, 075501 (2015).
61. Palik, E. D. & Ghosh, G. *Handbook of Optical Constants of Solids*. (Academic Press, San Diego, 1998).
62. Niklasson, G. A., Granqvist, C. G. & Hunderi, O. Effective medium models for the optical properties of inhomogeneous materials. *Appl. Opt.* **20**, 26 (1981).
63. Kaiser, N. Review of the fundamentals of thin-film growth. *Appl. Opt.* **41**, 3053 (2002).
64. Thyagarajan, K., Santschi, C., Langlet, P. & Martin, O. J. F. Highly Improved Fabrication of Ag and Al Nanostructures for UV and Nonlinear Plasmonics. *Adv. Opt. Mater.* **4**, 871–876 (2016).
65. Stefaniuk, T., Wróbel, P., Trautman, P. & Szoplik, T. Ultrasmooth metal nanolayers for plasmonic applications: surface roughness and specific resistivity. *Appl. Opt.* **53**, B237 (2014).
66. Liu, H. *et al.* Enhanced Surface Plasmon Resonance on a Smooth Silver Film with a Seed Growth Layer. *ACS Nano* **4**, 3139–3146 (2010).
67. Logeeswaran VJ *et al.* Ultrasmooth Silver Thin Films Deposited with a Germanium Nucleation Layer. *Nano Lett.* **9**, 178–182 (2009).
68. Ciesielski, A., Skowronski, L., Górecka, E., Kierdaszuk, J. & Szoplik, T. Growth model and structure evolution of Ag layers deposited on Ge films. *Beilstein J. Nanotechnol.* **9**, 66–76 (2018).

69. Wróbel, P. *et al.* Ge Wetting Layer Increases Ohmic Plasmon Losses in Ag Film Due to Segregation. *ACS Appl. Mater. Interfaces* **7**, 8999–9005 (2015).
70. Ciesielski, A., Trzcinski, M. & Szoplik, T. Inhibiting the Segregation of Germanium in Silver Nanolayers. *Crystals* **10**, 262 (2020).
71. Wachs, A. L., Miller, T. & Chiang, T.-C. Evidence for germanium segregation on thin films of Ag on Ge(111). *Phys. Rev. B* **33**, 8870–8873 (1986).
72. Lee, H.-C. The behaviors of the carrier concentrations and mobilities in indium–tin-oxide thin films by DC and RF-superimposed DC reactive magnetron sputtering at the various process temperatures. *Appl. Surf. Sci.* **252**, 2647–2656 (2006).
73. Wang, Y. *et al.* Tunability of indium tin oxide materials for mid-infrared plasmonics applications. *Opt. Mater. Express* **7**, 2727 (2017).
74. Cleary, J. W., Smith, E. M., Leedy, K. D., Grzybowski, G. & Guo, J. Optical and electrical properties of ultra-thin indium tin oxide nanofilms on silicon for infrared photonics. *Opt. Mater. Express* **8**, 1231 (2018).
75. Filatova, E. O. *et al.* Transparent-conductive-oxide (TCO) buffer layer effect on the resistive switching process in metal/TiO₂/TCO/metal assemblies. *New J. Phys.* **16**, 113014 (2014).
76. Kim, H. *et al.* Electrical, optical, and structural properties of indium–tin–oxide thin films for organic light-emitting devices. *J. Appl. Phys.* **86**, 6451–6461 (1999).
77. Brewer, S. H. & Franzen, S. Indium Tin Oxide Plasma Frequency Dependence on Sheet Resistance and Surface Adlayers Determined by Reflectance FTIR Spectroscopy. *J. Phys. Chem. B* **106**, 12986–12992 (2002).

78. Characterization of Oxygen Accumulation in Indium-Tin-Oxide for Resistance Random Access Memory. *IEEE Electron Device Lett.* **35**, 630–632 (2014).
79. Ma, Z., Li, Z., Liu, K., Ye, C. & Sorger, V. J. Indium-Tin-Oxide for High-performance Electro-optic Modulation. *Nanophotonics* **4**, (2015).
80. Kafaie Shirmanesh, G., Sokhoyan, R., Pala, R. A. & Atwater, H. A. Dual-Gated Active Metasurface at 1550 nm with Wide ($>300^\circ$) Phase Tunability. *Nano Lett.* **18**, 2957–2963 (2018).
81. Huang, Y.-W. *et al.* Gate-Tunable Conducting Oxide Metasurfaces. *Nano Lett.* **16**, 5319–5325 (2016).
82. Dey, B., Sarkar, S., Banik, H. & Arshad Hussain, S. Resistive switching behaviour of organic molecules. *Mater. Today Proc.* **46**, 6290–6294 (2021).
83. Ding, X., Huang, P., Zhao, Y., Feng, Y. & Liu, L. Understanding of the Volatile and Nonvolatile Switching in Ag-Based Memristors. *IEEE Trans. Electron Devices* **69**, 1034–1040 (2022).
84. Xu, D.-P. *et al.* In Situ Analysis of Oxygen Vacancies and Band Alignment in HfO₂/TiN Structure for CMOS Applications. *Nanoscale Res. Lett.* **12**, 311 (2017).
85. Martínez-Puente, M. A. *et al.* ALD and PEALD deposition of HfO₂ and its effects on the nature of oxygen vacancies. *Mater. Sci. Eng. B* **285**, 115964 (2022).
86. Perevalov, T. V. *et al.* Oxygen deficiency defects in amorphous Al₂O₃. *J. Appl. Phys.* **108**, 013501 (2010).

87. Choi, Y., Shin, J., Moon, S. & Shin, C. Investigation on Threshold Voltage Adjustment of Threshold Switching Devices with HfO₂/Al₂O₃ Superlattice on Transparent ITO/Glass Substrate. *Micromachines* **11**, 525 (2020).
88. Saadi, M. *et al.* Ag/HfO₂-based conductive bridge memories elaborated by atomic layer deposition: impact of inert electrode and HfO₂ crystallinity on resistive switching mechanisms. *J. Mater. Sci. Mater. Electron.* **31**, 13487–13495 (2020).
89. Yoo, J., Park, J., Song, J., Lim, S. & Hwang, H. Field-induced nucleation in threshold switching characteristics of electrochemical metallization devices. *Appl. Phys. Lett.* **111**, 063109 (2017).
90. Valov, I. *et al.* Atomically controlled electrochemical nucleation at superionic solid electrolyte surfaces. *Nat. Mater.* **11**, 530–535 (2012).
91. Pevtsov, A. B. *et al.* Evidence of field-induced nucleation switching in opal: VO₂ composites and VO₂ films. *Phys. Rev. B* **85**, 024110 (2012).
92. Karpov, V. G., Kryukov, Y. A., Savransky, S. D. & Karpov, I. V. Nucleation switching in phase change memory. *Appl. Phys. Lett.* **90**, 123504 (2007).
93. Wang, W. *et al.* Volatile Resistive Switching Memory Based on Ag Ion Drift/Diffusion Part I: Numerical Modeling. *IEEE Trans. Electron Devices* **66**, 3795–3801 (2019).
94. Elshekh, H., Wang, H., Yang, C. & Zhu, S. Nonvolatile behavior of resistive switching memory in Ag/WO_x/TiO_y/ITO device based on WO_x/TiO_y heterojunction. *J. Appl. Phys.* **135**, 135107 (2024).

95. Wang, W. *et al.* Volatile Resistive Switching Memory Based on Ag Ion Drift/Diffusion—Part II: Compact Modeling. *IEEE Trans. Electron Devices* **66**, 3802–3808 (2019).
96. Melikyan, A. *et al.* Surface plasmon polariton absorption modulator. *Opt. Express* **19**, 8855 (2011).
97. Sorger, V. J., Lanzillotti-Kimura, N. D., Ma, R.-M. & Zhang, X. Ultra-compact silicon nanophotonic modulator with broadband response. *Nanophotonics* **1**, 17–22 (2012).
98. Qian, K., Han, X., Li, H., Chen, T. & Lee, P. S. Uncovering the Indium Filament Revolution in Transparent Bipolar ITO/SiO_x/ITO Resistive Switching Memories. *ACS Appl. Mater. Interfaces* **12**, 4579–4585 (2020).
99. Li, Y. *et al.* High-Uniformity Threshold Switching HfO₂-Based Selectors with Patterned Ag Nanodots. *Adv. Sci.* **7**, 2002251 (2020).
100. Busby, Y. *et al.* Direct observation of conductive filament formation in Alq₃ based organic resistive memories. *J. Appl. Phys.* **118**, 075501 (2015).
101. Shibata, N. *et al.* Nonstoichiometric Dislocation Cores in α -Alumina. **316**, 5 (2007).
102. Noh, K. DEFECT ENGINEERING OF METAL OXIDE SEMICONDUCTORS. 131.
103. Qian, W. *et al.* Microstructural characterization of α -GaN films grown on sapphire by organometallic vapor phase epitaxy. *Appl. Phys. Lett.* **66**, 1252–1254 (1995).

104. Lester, S. D., Ponce, F. A., Craford, M. G. & Steigerwald, D. A. High dislocation densities in high efficiency GaN-based light-emitting diodes. *Appl. Phys. Lett.* **66**, 1249–1251 (1995).
105. Nakamura, A., Matsunaga, K., Tohma, J., Yamamoto, T. & Ikuhara, Y. Conducting nanowires in insulating ceramics. *Nat. Mater.* **2**, 453–456 (2003).
106. Tokumoto, Y. *et al.* Fabrication of electrically conductive nanowires using high-density dislocations in AlN thin films. *J. Appl. Phys.* **106**, 124307 (2009).
107. Eltoukhy, A. H. & Greene, J. E. Diffusion enhancement due to low-energy ion bombardment during sputter etching and deposition. *J. Appl. Phys.* **51**, 4444–4452 (1980).
108. Hunt, E. M. & Hampikian, J. M. Ion implantation-induced nanoscale particle formation in Al₂O₃ and SiO₂ via reduction. *Acta Mater.* **47**, 1497–1511 (1999).
109. HUNT, E. M. & HAMPIKIAN, J. M. ION IMPLANTATION-INDUCED NANOSCALE PARTICLE FORMATION IN Al₂O₃ AND SiO₂ VIA REDUCTION. 15.
110. Chan, W. L. & Chason, E. Making waves: Kinetic processes controlling surface evolution during low energy ion sputtering. *J. Appl. Phys.* **101**, 121301 (2007).
111. Gautier, M., Duraud, J. P., Van, L. P. & Guittet, M. J. Modifications of cw-A21 0,(0001) surfaces induced by thermal treatments or ion bombardment. 10.
112. Das, S. *et al.* Controlled manipulation of oxygen vacancies using nanoscale flexoelectricity. *Nat. Commun.* **8**, (2017).

- 113.Rechtin, M. D. A transmission electron microscopy study of the defect microstructure of Al_2O_3 , subjected to ion bombardment. *Radiat. Eff.* **42**, 129–144 (1979).
- 114.Cho, S. *et al.* Self-assembled oxide films with tailored nanoscale ionic and electronic channels for controlled resistive switching. *Nat. Commun.* **7**, (2016).
- 115.Feigenbaum, E., Diest, K. & Atwater, H. A. Unity-Order Index Change in Transparent Conducting Oxides at Visible Frequencies. *Nano Lett.* **10**, 2111–2116 (2010).
- 116.Lee, H. W. *et al.* Nanoscale Conducting Oxide PlasMOSFET. *Nano Lett.* **14**, 6463–6468 (2014).
- 117.Sherrott, M. C. *et al.* Experimental Demonstration of $>230^\circ$ Phase Modulation in Gate-Tunable Graphene–Gold Reconfigurable Mid-Infrared Metasurfaces. *Nano Lett.* **17**, 3027–3034 (2017).
- 118.Shcherbakov, M. R. *et al.* Ultrafast all-optical tuning of direct-gap semiconductor metasurfaces. *Nat. Commun.* **8**, (2017).
- 119.Alam, M. Z., Schulz, S. A., Upham, J., De Leon, I. & Boyd, R. W. Large optical nonlinearity of nanoantennas coupled to an epsilon-near-zero material. *Nat. Photonics* **12**, 79–83 (2018).
- 120.Wilk, G. D., Wallace, R. M. & Anthony, J. M. High- κ gate dielectrics: Current status and materials properties considerations. *J. Appl. Phys.* **89**, 5243–5275 (2001).

121. Zafar, S., Kumar, A., Gusev, E. & Cartier, E. Threshold voltage instabilities in high- κ gate dielectric stacks. *IEEE Trans. Device Mater. Reliab.* **5**, 45–64 (2005).
122. Mannequin, C. *et al.* Dielectric relaxation in hafnium oxide: A study of transient currents and admittance spectroscopy in HfO₂ metal-insulator-metal devices. *J. Appl. Phys.* **110**, 104108 (2011).
123. Burkhardt, P. J. Dielectric relaxation in thermally grown SiO₂ films. *IEEE Trans. Electron Devices* **ED-13**, 268–275 (1966).
124. Zhao, C., Zhao, C. Z., Werner, M., Taylor, S. & Chalker, P. Dielectric relaxation of high- κ oxides. *Nanoscale Res. Lett.* **8**, 456 (2013).
125. Saville, D. A. ELECTROHYDRODYNAMICS: The Taylor-Melcher Leaky Dielectric Model. *Annu. Rev. Fluid Mech.* **29**, 27–64 (1997).
126. Pustovarov, V. A., Perevalov, T. V., Gritsenko, V. A., Smirnova, T. P. & Yelisseyev, A. P. Oxygen vacancy in Al₂O₃: Photoluminescence study and first-principle simulation. *Thin Solid Films* **519**, 6319–6322 (2011).
127. Yang, K. J. & Chenming Hu. MOS capacitance measurements for high-leakage thin dielectrics. *IEEE Trans. Electron Devices* **46**, 1500–1501 (1999).
128. Suh, D. & Liang, W. S. Electrical properties of atomic layer deposited Al₂O₃ with anneal temperature for surface passivation. *Thin Solid Films* **539**, 309–316 (2013).
129. Rafi, J. M., Zabala, M., Beldarrain, O. & Campabadal, F. Deposition Temperature and Thermal Annealing Effects on the Electrical Characteristics of

- Atomic Layer Deposited Al₂O₃ Films on Silicon. *J. Electrochem. Soc.* **158**, G108 (2011).
130. Kersten, F., Schmid, A., Bordihn, S., Müller, J. W. & Heitmann, J. Role of Annealing Conditions on Surface Passivation Properties of ALD Al₂O₃ Films. *Energy Procedia* **38**, 843–848 (2013).
131. Kim, B., Kang, T., Lee, G. & Jeon, H. The effect of an annealing process on atomic layer deposited TiO₂ thin films. *Nanotechnology* **33**, 045705 (2022).
132. Hu, Y., Diao, X., Wang, C., Hao, W. & Wang, T. Effects of heat treatment on properties of ITO films prepared by rf magnetron sputtering. *Vacuum* **75**, 183–188 (2004).
133. Gulen, M. *et al.* Role of annealing temperature on microstructural and electro-optical properties of ITO films produced by sputtering. *J. Mater. Sci. Mater. Electron.* **24**, 467–474 (2013).
134. Kerkache, L., Layadi, A., Dogheche, E. & Rémiens, D. Physical properties of RF sputtered ITO thin films and annealing effect. *J. Phys. Appl. Phys.* **39**, 184–189 (2006).
135. Pokaipisit, A., Horprathum, M. & Limsuwan, P. Vacuum and Air Annealing Effects on Properties of Indium Tin Oxide Films Prepared by Ion-Assisted Electron Beam Evaporation. *Jpn. J. Appl. Phys.* **47**, 4692 (2008).
136. Sathiaraj, T. S. Effect of annealing on the structural, optical and electrical properties of ITO films by RF sputtering under low vacuum level. *Microelectron. J.* **39**, 1444–1451 (2008).

137. Lynch, J., Guarneri, L., Jariwala, D. & Van De Groep, J. Exciton resonances for atomically-thin optics. *J. Appl. Phys.* **132**, 091102 (2022).
138. Datta, I. *et al.* 2D material platform for overcoming the amplitude–phase tradeoff in ring resonators. *Optica* **11**, 48 (2024).
139. Datta, I. *et al.* Low-loss composite photonic platform based on 2D semiconductor monolayers. *Nat. Photonics* **14**, 256–262 (2020).
140. Sokhoyan, R., Hail, C. U., Foley, M., Grajower, M. Y. & Atwater, H. A. All-Dielectric High-Q Dynamically Tunable Transmissive Metasurfaces. *Laser Photonics Rev.* 2300980 (2024) doi:10.1002/lpor.202300980.
141. Novotny, L. & Hecht, B. *Principles of Nano-Optics*. (Cambridge University Press, 2012). doi:10.1017/CBO9780511794193.
142. <https://optics.ansys.com/hc/en-us/articles/4414575008787-RCWA-Solver-Introduction>.
143. Sinatkas, G., Christopoulos, T., Tsilipakos, O. & Kriezis, E. E. Electro-optic modulation in integrated photonics. *J. Appl. Phys.* **130**, 010901 (2021).
144. Vyshnevyy, A. A. *et al.* A hidden advantage of van der Waals materials for overcoming limitations in photonic integrated circuitry.
145. Krasnok, A., Lepeshov, S. & Alú, A. Nanophotonics with 2D transition metal dichalcogenides [Invited]. *Opt. Express* **26**, 15972 (2018).
146. Liu, Y. *et al.* Van der Waals heterostructures and devices. *Nat. Rev. Mater.* **1**, 16042 (2016).
147. Liu, Y. *et al.* Promises and prospects of two-dimensional transistors. *Nature* **591**, 43–53 (2021).

148. Sebek, M. Transition Metal Dichalcogenides for Optoelectronic Applications.
149. Liu, Y. *et al.* Promises and prospects of two-dimensional transistors. *Nature* **591**, 43–53 (2021).
150. Miao, J. *et al.* Gate-Tunable Semiconductor Heterojunctions from 2D/3D van der Waals Interfaces. *Nano Lett.* **20**, 2907–2915 (2020).
151. Munkhbat, B., Wróbel, P., Antosiewicz, T. J. & Shegai, T. Optical constants of several multilayer transition metal dichalcogenides measured by spectroscopic ellipsometry in the 300-1700 nm range: high-index, anisotropy, and hyperbolicity. Preprint at <http://arxiv.org/abs/2203.13793> (2022).
152. Yu, Y. *et al.* Giant Gating Tunability of Optical Refractive Index in Transition Metal Dichalcogenide Monolayers. *Nano Lett.* **17**, 3613–3618 (2017).
153. Li, M., Biswas, S., Hail, C. U. & Atwater, H. A. Refractive Index Modulation in Monolayer Molybdenum Diselenide. *Nano Lett.* **21**, 7602–7608 (2021).
154. van de Groep, J. *et al.* Exciton resonance tuning of an atomically thin lens. *Nat. Photonics* **14**, 426–430 (2020).
155. Li, M., Hail, C. U., Biswas, S. & Atwater, H. A. Excitonic Beam Steering in an Active van der Waals Metasurface. *Nano Lett.* **23**, 2771–2777 (2023).
156. Byrnes, S. J. Multilayer optical calculations. *ArXiv160302720 Phys.* (2019).
157. Wooten, F. Optical Properties of Solids. 270.
158. Evans, B. L. & Hazelwood, R. A. Optical and structural properties of MoSe₂. *Phys. Status Solidi A* **4**, 181–192 (1971).

159. Ruppert, C., Aslan, O. B. & Heinz, T. F. Optical Properties and Band Gap of Single- and Few-Layer MoTe₂ Crystals. *Nano Lett.* **14**, 6231–6236 (2014).
160. Beal, A. R. & Hughes, H. P. Kramers-Kronig analysis of the reflectivity spectra of 2H-MoS₂, 2H-MoSe₂ and 2H-MoTe₂. *J. Phys. C Solid State Phys.* **12**, 881–890 (1979).
161. Kuzmenko, A. B. Kramers–Kronig constrained variational analysis of optical spectra. *Rev. Sci. Instrum.* **76**, 083108 (2005).
162. Yang, S. *et al.* Gate Dielectrics Integration for 2D Electronics: Challenges, Advances, and Outlook. *Adv. Mater.* **35**, 2207901 (2023).
163. Kim, H. G. & Lee, H.-B.-R. Atomic Layer Deposition on 2D Materials. *Chem. Mater.* **29**, 3809–3826 (2017).
164. Cai, J., Han, X., Wang, X. & Meng, X. Atomic Layer Deposition of Two-Dimensional Layered Materials: Processes, Growth Mechanisms, and Characteristics. *Matter* **2**, 587–630 (2020).
165. Mattinen, M., Leskelä, M. & Ritala, M. Atomic Layer Deposition of 2D Metal Dichalcogenides for Electronics, Catalysis, Energy Storage, and Beyond. *Adv. Mater. Interfaces* **8**, 2001677 (2021).
166. Turunen, M., Fernandez, H., Akkanen, S.-T., Seppänen, H. & Sun, Z. Effects of atomic layer deposition on the optical properties of two-dimensional transition metal dichalcogenide monolayers. *2D Mater.* **10**, 045018 (2023).
167. Nam, T., Seo, S. & Kim, H. Atomic layer deposition of a uniform thin film on two-dimensional transition metal dichalcogenides. *J. Vac. Sci. Technol. Vac. Surf. Films* **38**, 030803 (2020).

- 168.Cheng, L. *et al.* Atomic Layer Deposition of a High- k Dielectric on MoS₂ Using Trimethylaluminum and Ozone. *ACS Appl. Mater. Interfaces* **6**, 11834–11838 (2014).
- 169.Datta, I. *et al.* 2D material platform for overcoming the amplitude–phase tradeoff in ring resonators. *Optica* **11**, 48 (2024).
- 170.Zhao, J. *et al.* Exciton polariton interactions in Van der Waals superlattices at room temperature. *Nat. Commun.* **14**, 1512 (2023).
- 171.Yun, T., Estrecho, E., Truscott, A. G., Ostrovskaya, E. A. & Wurdack, M. J. Fabrication of high-quality PMMA/SiO₂ spaced planar microcavities for strong coupling of light with monolayer WS₂ excitons. *Appl. Phys. Lett.* **121**, 081105 (2022).
- 172.Paik, E. Y. *et al.* High Quality Factor Microcavity for Van der Waals Semiconductor Polaritons Using a Transferrable Mirror. *Adv. Opt. Mater.* **11**, 2201440 (2023).
- 173.Rupprecht, C. *et al.* Micro-mechanical assembly and characterization of high-quality Fabry–Pérot microcavities for the integration of two-dimensional materials. *Appl. Phys. Lett.* **118**, 103103 (2021).
- 174.Knopf, H. *et al.* Integration of atomically thin layers of transition metal dichalcogenides into high-Q, monolithic Bragg-cavities: an experimental platform for the enhancement of the optical interaction in 2D-materials. *Opt. Mater. Express* **9**, 598 (2019).
- 175.Cheng, Z. *et al.* Are 2D Interfaces Really Flat? *ACS Nano* **16**, 5316–5324 (2022).